ROMA TRE
Università degli studi

Roma Tre University
Department of Civil Engineering

Ph.D. in Civil Engineering
XXIV Cycle

Ph.D. Thesis

Gravity currents: laboratory experiments and numerical simulations

Ph.D. Student: Valentina Lombardi

Tutor: Prof. Giampiero Sciortino

Co-tutors: Dr. Claudia Adduce

       Prof. Michele La Rocca

Ph.D. Coordinator: Prof. Leopoldo Franco

Rome, February 2012

ii

Abstract

Gravity currents are buoyancy-driven flows due to a density gradient between two fluids and frequently occur in both natural and industrial flows. In this work two-dimensional and three-dimensional gravity current's dynamics was investigated by laboratory experiments and numerical simulations. A widely used experimental technique, called *lock exchange release* was applied to carry out laboratory experiments. In this configuration the tank is divided by a vertical gate into two parts, filled with salty and fresh water, respectively. As soon as the gate is removed, a non-equilibrium condition occurs and the heavier fluid flows under the lighter one, producing the gravity current, whose evolution is recorded by a CCD camera. An image analysis technique, based on the threshold method is then applied in order to measure the space-time evolution of the current's profile.

Experimental 2D gravity currents were realized in order to study the effect of the density difference between the two fluids and both the roughness and the slope's angle of the bed on the current's dynamics. In particular, one of the innovative aspects of this paper is to be focused on gravity currents on upsloping bed, while to the author's knowledge most of the previous studies deals with currents flowing on downsloping beds. Moreover, regarding 2D configuration, instantaneous velocity measurements were performed by PIV technique (Particle Image Velocimetry). Numerical simulations of 2D gravity currents were performed by a 1D, two-layer, shallow-water model developed by Adduce et al. (2012). The model takes into account the space-time evolution of free-surface and the mixing between the two layers. Entrainment at the interface between the gravity current and the ambient fluid is modeled by a modified Ellison & Turner's formula (1959). Several tests were run to calibrate an entrainment parameter in order to reproduce gravity currents moving on both smooth flat and upsloping beds.

Experimental 3D gravity currents were carried out in order to test different values of initial density and height of the current and the length of the gate. A single layer, 2D, shallow-water model was used to perform numerical simulations for 3D currents. As for the 1D model, the entrainment is taken into account in the flow's dynamics.

Experimental results and the comparison between experimental data and numerical prediction for both 2D and 3D configuration are presented, showing that the used models are valid tools to reproduce gravity currents' dynamics.

Sommario

Le correnti di gravità sono generate da un gradiente di densità tra due fluidi e rappresentano un fenomeno diffuso in ambito naturale e artificiale. Obiettivo di questo lavoro è l'analisi di correnti di gravità bidimensionali e tridimensionali attraverso esperimenti di laboratorio e simulazioni numeriche. Le correnti di gravità sono state realizzate in laboratorio con una tecnica sperimentale ampiamente diffusa detta "*lock exchange release*". Un canale in plexiglass è suddiviso da un setto verticale rimovibile in due volumi distinti, uno riempito con una soluzione acquosa salina e l'altro con acque dolce. Non appena avviene la rimozione del setto, si verifica una condizione di disequilibrio e il fluido più denso scorre al di sotto del fluido ambiente più leggero. L'evoluzione della corrente di gravità così generata è acquisita con una telecamera digitale e una tecnica di analisi d'immagine è stata poi applicata per misurare l'evoluzione spazio-temporale del profilo della corrente.

Le correnti di gravità 2D sono state realizzate allo scopo di studiare l'effetto del gradiente di densità tra i due fluidi, della scabrezza e della pendenza del fondo sulla dinamica della corrente. In particolar modo, il presente lavoro è stato focalizzato sullo studio della dinamica di correnti su fondo acclive, mentre la maggior parte degli studi in letteratura riguarda correnti su fondo declive. Riguardo alla configurazione 2D, sono state realizzate misure istantanee del campo di velocità con la tecnica PIV (Particle Image Velocimetry). Per simulare le correnti 2D è stato utilizzato un modello 1D shallow-water a due strati sviluppato da Adduce et al. (2012). Il modello tiene conto dell'evoluzione spazio-temporale della superficie libera. Il mescolamento all'interfaccia tra i due fluidi è modellato attraverso una forma modificata della formula di Ellison & Turner (1959). Sono state realizzate diverse prove numeriche per calibrare un parametro di mescolamento allo scopo di riprodurre correttamente le correnti di gravità su fondo piano e acclive. Le correnti 3D sono state realizzate allo scopo di esaminare diversi valori di densità iniziale del fluido denso, di altezza iniziale dei due fluidi e di lunghezza del setto. Per le simulazioni numeriche delle correnti 3D è stato utilizzato un modello 2D shallow-water a uno strato sviluppato da La Rocca et al. (2009). Così come il modello 1D, anche il modello 2D tiene conto del mescolamento all'interfaccia tra i due fluidi. Il confronto con le simulazioni numeriche per le correnti di gravità 2D e 3D mostra che i modelli utilizzati sono validi strumenti per la riproduzione della dinamica delle correnti di gravità.

Valentina Lombardi

Contents

List of figures

Valentina Lombardi

List of tables

List of symbols

b	Width of the tank – 2D experiments
B	Width of the tank – 3D experiments
C	Depth averaged concentration – 2D model
d	Length of removable gate – 3D experiments
g	Gravity acceleration
g'	Reduced gravity acceleration
h^*	Non-constant height of current's shape
h_0	Initial height of the lock fluid
$h_1; h_2$	Height of dense and ambient fluid – 1D model
H	Total height of the two fluids
k	Dimensionless entrainment parameter – 1D model
l^*	Transition point between self-similar and viscous phase
$l_s; l_{ss}; l_{vis}$	Length of slumping, self-similar and viscous phase
L	Half length of the tank – 3D experiments
u	x-velocity component
U	Depth averaged x-component velocity – 2D model
U_f	Front's velocity
U_m	Velocity modulus – 2D model
V	Depth averaged y-component velocity – 2D model

Valentina Lombardi

V_1; V_2	Velocity of dense and ambient fluid – 1D model
V_e	Entrainment velocity – 1D model
$T_{xz}|_{z=0}$; $T_{yz}|_{z=0}$	Bottom stresses – 3D model
x_0	Gate position – 2D experiments
x_f	Front's position
α	Entrainment coefficient – 2D model
ε	Bed's roughness
ϑ	Slope's angle of the tank
λ_1; λ_2	Friction factor for lower and upper layer – 1D model
λ_{int}	Friction factor at the interface – 1D model
λ_∞	Friction factor for turbulent rough flows
μ	Dynamic viscosity
v	Kinematic viscosity
ρ_{01}	Initial density of the heavier lock fluid
ρ_1; ρ_2	Density of dense and ambient fluid
ρ_p	Density of reflective particles
ρ_s	Density of sediments
τ_{1b} ; τ_{2b}	Bottom stresses – 1D model
τ_{12}	Stress term at the interface – 1D model
ω	Vorticity

1. Introduction

1.1. The nature of gravity currents

Gravity currents, also called density or buoyancy currents, are flows generated by a density gradient between two fluids and occur in both natural and industrial flows. A large variety of examples of gravity currents can be found in Simpson, 1997. The basic sketch of a typical gravity current configuration is shown in Figure 1.1. The gravity current with density ρ_1 propagates into the ambient fluid with a different density ρ_2. If $\rho_1 > \rho_2$ the more dense (heavy) fluid flows below the upper layer, generating a bottom gravity current, while if $\rho_2 > \rho_1$ a top current of less dense (light) fluid occurs. Gravity currents can also occur as intrusions of mixed fluid in a sharply or linearly stratified ambient (Ungarish, 2009). The former case of a bottom current is the object of this work. In this configuration (i.e. $\rho_1 > \rho_2$), the current with higher density ρ_1 and non-constant depth h^* moves forward with front's velocity U_f into the surrounding fluid with lower density ρ_2. The total depth of the two fluids is H. Behind the head of the current mixing and instabilities are concentrated. Underneath this area sedimentation and resuspension of particles can occur, if sediments are carried by the current.
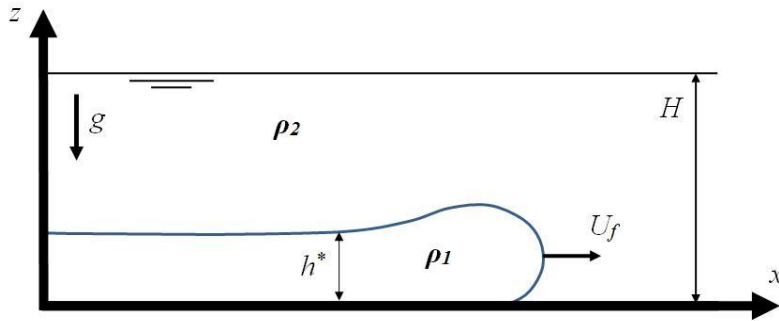
Figure 1.1: Basic sketch of a gravity current.

Gravity currents frequently develop along the longitudinal direction, so that the ratio of the vertical scale of the current to the horizontal length scale is small enough to allow the application of the shallow-water theory.
In the gravity current's shape a head and a tail can be distinguished. The head is located at the leading edge, and it is almost twice as high as the following flow (Simpson, 1982), frequently called tail of the current.   In the frontal zone of the current (i.e. the head) a nose rising above the following flow can usually be observed (Simpson, 1997).

In a typical gravity current configuration, hydrostatic balance can be assumed in the *z*-direction. Regarding the horizontal direction the density difference causes a pressure difference in the *x*-direction, which is then balanced by the velocity field with a main horizontal component U_f (Ungarish, 2009). Therefore the gravity current is driven by the gravity force and the gravity effect related to the density gradient is called reduced gravity g' and is defined in this work as:

$$g' = g\frac{\Delta\rho}{\rho_2} = g\frac{\rho_1 - \rho_2}{\rho_2} \tag{1}$$

where g is the gravity acceleration. The advantage of using g' is that in its own definition a large range of the ratio ρ_1/ρ_2 are included.

It's possible to distinguish *Boussinesq* and *non-Boussinesq* gravity currents. The former are characterized by a relatively small difference between the densities of the two fluids involved in the flow. Hence in this case $\rho_1 \cong \rho_2$, or $\rho_1/\rho_2 \cong 1$. Non-Boussinesq gravity currents are the ones for which the above condition is not verified.

Moreover gravity currents can be classified also as *compositional* or *particle-driven* gravity currents. In the case of compositional gravity currents the driving force is represented by dissolved solute like salt in the sea or difference of temperature, while for particle-driven gravity currents the driving force is represented by the suspension of sediments. A combination of the two types can also occur. Examples of compositional gravity currents are the sea breeze winds and submarine currents; the former are driven by a temperature gradient, while the latter are driven by a difference in salinity. Particle driven gravity currents are also common phenomena in natural environment, for example sandstorms and avalanches. The currents studied in the present work are all of Boussinesq type and the density difference between ρ_1 and ρ_2 is due to a difference in concentration of salt dissolved in the fluids (i.e. compositional gravity currents).

Front speed U_f can be roughly estimated by applying Bernoulli' law to a simplified scheme shown in Figure 1.2. Assuming a frame of reference moving with the front, the fluid in the current is at rest and the surrounding fluid moves toward the current's front with propagation velocity $-U_f$. Assuming a hydrostatic pressure distribution, equating the values of potential and kinetic energy between points *O* and *N*, the following relation can be obtained:

$$\frac{1}{2}\rho_2 U_f^2 + \rho_2 g\left(H - \frac{h}{2}\right) = \rho_1 g(H - h) + \rho_1 g\frac{h}{2} \tag{2}$$

From Equation (2) propagation velocity of the current can be obtained:

Valentina Lombardi

$$U_f = \sqrt{\frac{\rho_1 - \rho_2}{\rho_1} gh} = \sqrt{g'h} \qquad (3)$$

Although Equation (3) is estimated on the basis of a very simple energy balance assuming some simplifications, it represents a starting value for the speed of propagation of the typical gravity current.

An important dimensionless parameter for a Boussinesq gravity current is the Froude number Fr, defined as the ratio of the current speed U and the long wave speed $\sqrt{g'h}$:

$$Fr = \frac{U}{\sqrt{g'h}} \qquad (4)$$

Equation (4) shows that Froude number is a dimensionless representation of the speed of the current.

Another important dimensionless parameter is the Reynolds number Re, defined as:

$$Re = \frac{Uh}{v} \qquad (5)$$

where v is the kinematic viscosity. Equation (5) shows that Reynolds number measures the importance of viscous dissipation on the current. Simpson (1997) suggested that for values of Reynolds numbers greater than 1000 viscous effects are unimportant.

The two main types of instabilities involved in gravity current's dynamics are Kelvin-Helmotz billows and the lobes-and-clefts structure. Kelvin-Helmotz billows roll up in the region of velocity shear above the front of the current, contributing to the mixing processes behind the current's head. The complex lobes-and-clefts shifting is due to the gravitational instabilities of the less dense ambient fluid which is overrun by the nose of the gravity current (Simpson, 1997).

Figure 1.3 and Figure 1.4 show two images referred to laboratory experiments performed in the Hydraulics Laboratory of University of Rome "Roma Tre". The currents were realized by a lock exchange release, a widely used experimental technique that will be fully explained in section 1.2. In Figure 1.3 a visualization of the area behind the head of a gravity current is shown. Vortexes

are visible at the interface between the two fluids due to the velocity shear between the two layers with different densities.

The frontal region of a typical gravity current can be observed in Figure 1.4. The currents in Figure 1.3 and in Figure 1.4 were made visible by adding some white colorant to the dense fluid.
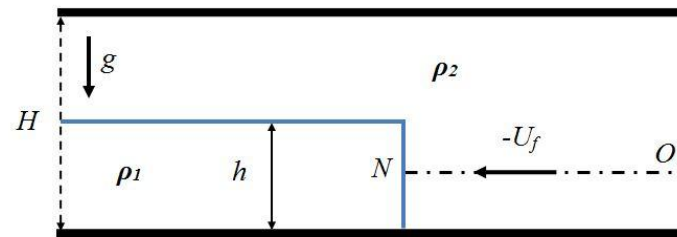
Figure 1.2: Schematic diagram of a gravity current.
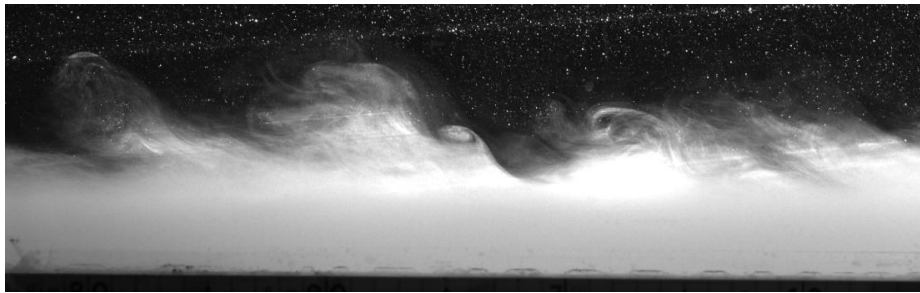
Figure 1.3: Visualization of the area behind the head of a gravity current realized in the Hydraulics Laboratory of University of Rome "Roma Tre". Instabilities can be observed at the interface between the fluids.

Figure 1.4: Front of a gravity current of salty water flowing in fresh surrounding water realized in the Hydraulics Laboratory of University of Rome "Roma Tre".

1.2.   Lock exchange release

An experimental technique widely used to produce laboratory gravity currents is the lock-exchange release. In this configuration a tank is divided in two portions separated by a vertical sliding gate, one filled with lighter fluid (e.g. fresh water), and the other filled with the heavier one (e.g. salty water). It's possible to distinguish two different initial configurations: a full depth (Figure 1.5a) if the initial heights of the two fluids are the same and partial-depth (Figure 1.5b) if the initial height of the dense fluid is only a fraction of the whole height. The present work deals with full-depth experiments. The experiment begins when the gate is suddenly removed and a non-equilibrium condition occurs between the two fluids. Hence the heavier fluid flows under the lighter one, producing the gravity current. The experiment stops when the current's front reaches the right end wall of the tank. Figure 1.6a-f show the images acquired by a CCD camera of a gravity current produced by a full-depth lock exchange experiment in a Perspex tank in the Hydraulics Laboratory of University of Rome "Roma Tre". The time step between the images is about 1.68 s. In Figure 1.6a the initial configuration is shown, while in Figure 1.6b-f the resulting flow from the release of the dense fluid can be observed: the dense gravity current moves to the right part of the tank along the bottom boundary, while the buoyant current (i.e. ambient fluid) flows to left along the upper boundary.
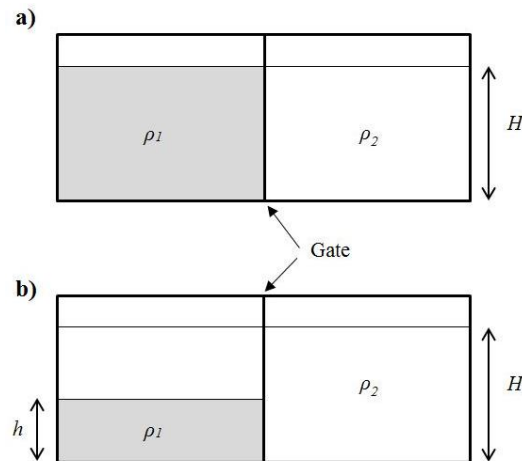
Figure 1.5a-b: Sketch of initial conditions for full-depth (a) and partial-depth (b) configuration of lock exchange release experiment.

Huppert & Simpson (1980) and Rottman & Simpson (1983) investigated gravity currents performing lock exchange experiments in a channel of rectangular

cross-section and showed that three phases can be distinguished in the dynamics of a gravity current produced by an instantaneous release. The first phase, called *slumping phase*, is characterized by a constant speed and a linear variation of the front position with time. During the second phase, called *self-similar phase*, the front's speed depends on time by a power law as $t^{-1/3}$ and the front position varies with $t^{2/3}$ (Rottman & Simpson, 1983). The transition between the first and the second phase occurs when a bore, caused by the reflection of the lighter fluid to the left wall of the tank, reaches the current's front, which is slower than the bore. Rottman & Simpson (1983) found that the first phase stops at a distance from the left wall, l_s, given by:

$$x_f = l_s \cong 10 \cdot x_0 \tag{6}$$

where x_f is the front position and x_0 is a length scale defined as the distance between the gate and the left vertical wall of the tank.
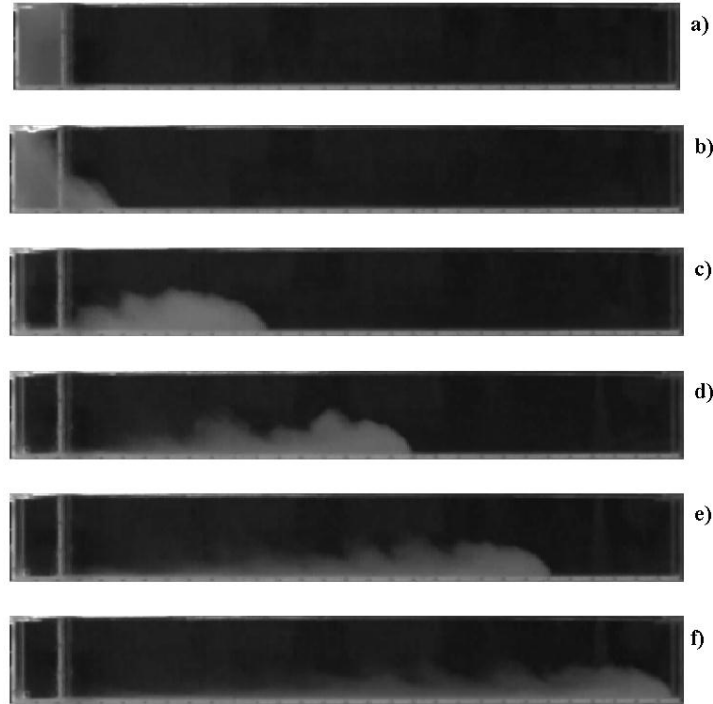
Figure 1.6a-f: Images acquired by the camera of a released gravity current: initial configuration (a), flow of the dense fluid (b-f). The time step between the frames is about 1.68 s.

If viscous and inertial forces become comparable, a third *viscous phase* occurs and the current's speed decreases with a law as $t^{-4/5}$, while the front position increases with $t^{1/5}$ (Huppert, 1982). Huppert (1982) also found that the transition between the self-similar phase and the viscous phase is reached when $x_f \cong l^*$ with l^* defined as:

$$l^* = \left(\frac{g'_0 \, h_0^5 \, x_0^5}{v^2} \right)^{\frac{1}{7}}$$ (7)

where h_0 is the initial height of the heavier fluid, v is the kinematic viscosity of the dense fluid and g_0' is the initial reduced gravity, defined as:

$$g'_0 = g \, \frac{\rho_{01} - \rho_2}{\rho_2}$$ (8)

in which ρ_{01} is the initial density of the gravity current and ρ_2 is the density of the ambient fluid.

1.3. Previous studies

Many studies investigated gravity currents by both laboratory experiments and numerical simulations.

The first quantitative study of gravity currents was an essay, published by von Kármán in 1940, proposing a perfect-fluid model for steadily propagating gravity currents. The motivation of such a study was an enquiry by the American military before the War World II concerning the evaluation of what wind conditions would allow to poisonous gas to move forward and reach the enemy avoiding the backwards flow towards the troops who released the substance (Huppert, 2006). He considered a frame of reference moving with the dense fluid (of density ρ_1), which is therefore assumed to be at rest, while the ambient fluid (of density ρ_2) of infinite depth appears to be in stationary motion above the interface between the two layers, with propagation velocity c_1. On the basis of Bernoulli's theorem von Kármán found that the angle formed between the interface and the bottom at the stagnation point is 60°. Moreover, by applying the Bernoulli's theorem between the stagnation point and several points at the interface where this is supposed to become horizontal, he obtained a relation for

the velocity of the flow along the interface. The dimensionless speed found by von Kármán is given by:

$$Fr_H = \frac{c_1}{\sqrt{g'H}} \qquad (9)$$

where H is the asymptotic height of the interface. The Froude number was evaluated by von Kármán to be $\sqrt{2}$. For gravity flows propagating into a very deep ambient at high Reynolds number, the condition proposed by von Kármán has been generally applied at the nose of the current.

Benjamin (1968) argued that von Kármán (1940) used incorrectly the Bernoulli's theorem by applying it along the interface, where dissipation takes place. By using a momentum integral, Benjamin obtained the same result as von Kármán.

A simple theory by Prandt (1952) concerns the transient phase following the release of dense fluid in a deep surrounding fluid with lower density. Neglecting hydrostatic forces and applying the hypothesis that the roll formed at the rear of the head of the current does not fall backward, Prandt (1952) obtained the ratio of the propagation velocity to the flow velocity by the evaluation of the dynamic pressures against the front. Prandt's theory can only be applied to the transient phase, during which the gate between the two fluids is partially opened. In fact, as soon as the gate is removed, the roll formed at the rear of the head of the currents falls behind and entrained with the lower layer, developing a turbulent motion at the front. After this stage of development, a state of stationary propagation takes place, in which turbulent motion is confined to the head of the current and the ratio of the propagation velocity to the flow velocity must be 1 (Benjamin, 1968).

As previously touched on, Benjamin provides an alternative argument leading to the same results of von Kármán, by the use of a momentum integral, or flow force, as himself called it in Benjamin (1968). Benjamin develops its theory for a cavity empty or filled with air, whose weight can be neglected. Shin et al. (2004) proposed Benjamin's theory on the basis of an idealized two-dimensional gravity current of density ρ_2 which flows with constant velocity U into a surrounding fluid with density ρ_1. The frame of reference moves with the front. The total depth of the two layers is H, while the depth of the current, where the interface becomes flat, is h. The velocity of the ambient fluid is supposed to be constant and it is denoted as u_1. The control volume is delimited by two horizontal boundaries and two vertical planes, one downstream and one upstream. As no external forces are involved in the system, the net flux of horizontal momentum into the considered control volume is zero. By the use of continuity equation and conservation of the horizontal component of the

momentum flux between the vertical sections, taking into account the hydrostatic pressure distribution, the following relation can be obtained:

$$\frac{U^2}{gH} = \frac{1-\gamma}{\gamma} f(h) \tag{10}$$

where γ is the density ratio ρ_1/ρ_2 and $f(h)$ is given by:

$$f(h) = \frac{h(2H-h)(H-h)}{H^2(H+h)} \tag{11}$$

The Froude number F_H is then defined as:

$$F_H = \frac{U}{\sqrt{g(1-\gamma)H}} \tag{12}$$

Benjamin (1968) showed that if dissipation can be neglected, Bernoulli's theorem can be applied along another streamline, which can be the top boundary or the interface between the two fluids and the following definition can be obtained:

$$\frac{U^2}{gH} = 2\frac{(1-\gamma)}{\gamma} \frac{h(H-h)^2}{H^3} \tag{13}$$

Equating relations (10) and (13), two solutions for h/H are provided:

$$\begin{aligned} \frac{h}{H} &= 0 \\ \frac{h}{H} &= \frac{1}{2} \end{aligned} \tag{14}$$

The second solution says that the current must occupy half the distance between the horizontal plates if the flow as to be steady and without energy dissipation. Considering a Bossinesq current, the density ratio $\gamma=1$, hence the Froude number F_H is defined as:

$$F_H = \frac{U}{\sqrt{g(1-\gamma)H}} = \frac{U}{\sqrt{g'H}} = \frac{1}{2} \tag{15}$$

Benjamin (1968) reached the same results of von Kármán, for the case of a gravity current moving into an infinitively deep ambient fluid. Hence for the case of $H \to \infty$, $h/H = 0$ and the Froude number in terms of depth of the current h is found to be $\sqrt{2}$, as von Kármán suggested.

Rottman & Simpson (1983) proposed a shallow-water model considering the current as a two-dimensional two-layer flow bounded at the top and at the bottom by horizontal planes. They considered the partial-depth lock release (Figure 1.5b), involving two inviscid, incompressible fluids with slightly different densities and assumed mixing negligible. They imposed the following front condition:

$$\frac{U_f^2}{g'H_f} = \beta^2 \frac{(H - h_f)(2H - h_f)}{2H(H + h_f)} \tag{16}$$

where U_f is the front's speed, h_f is the depth at the front and β is a dimensionless constant.

More recently, Shin et al. (2004) considered the case of a partial-depth lock exchange experiments. They developed an hydraulic model for unsteady and irrotational flow, in which, for high Reynolds number, the energy dissipation is a weak component. In contrast with Benjamin's theory they included in the control volume both the current's front and the wave depression. The fluid is assumed to be inviscid and immiscible, and the pressure distribution is assumed to hydrostatic. Moreover they supposed an horizontal surface between the depression wave and the current's front.

By the use of continuity equation and horizontal momentum conservation, and applying time-dependent Bernoulli's theorem and choosing a suitable velocity potential, Shin et al. (2004) found the following definition for the speed of the current:

$$\frac{U^2}{gH} = \frac{(\rho_2 - \rho_1)D(D - h)(H - h)}{2hH(\rho_2(H + h) + \rho_1 h)} \tag{17}$$

where D is the lock depth, h is the current's depth and H is the total depth of the two fluids. As for the Benjamin's theory, in order to specify h, a further

Valentina Lombardi

condition is needed. Therefore Shin et al. (2004) assumed an energy-conserving flow, in order to equate energy gain and energy loss in the control volume and obtain a further relation for the current speed:

$$\frac{U^2}{gH} = \frac{(\rho_2 - \rho_1)(D - h)(H - h)}{H(\rho_2(H - h) + \rho_1 h)} \qquad (18)$$

Comparing Equation (17) and Equation (18) the only non-trivial solution is given by:

$$h = \frac{D}{2} \qquad (19)$$

This results shows that an energy-conserving current produced by a partial-depth release has an height which is half of the initial height of the lock. Such result is consistent with Benjamin's result (Equation 14) for a full-depth release. Using Equation (19) the speed of the current for a Boussinesq gravity current (i.e. $\gamma \cong 1$) is:

$$F_H = \frac{U}{\sqrt{g(1 - \gamma)H}} = \frac{1}{2}\sqrt{\frac{D}{H}\left(2 - \frac{D}{H}\right)} \qquad (20)$$

For a full-depth release Equation (20) leads to the Benjamin's results $F_H = 1/2$, while for the case of a partial-depth release the presented theory differs from Benjamin's one.

Marino et al. (2005), on the basis of their experimental results showed that during the slumping phase (i.e. constant-speed phase) the Froude number can be defined in terms of lock depth, while during the second similar phase, which is no more influenced by the initial conditions, the Froude number is better defined on the basis of the maximum height of the current's head, which corresponds to the height at the rear of the head. They also found that Froude number defined in such way is dependent on the Reynolds number over the range 400-4500.

More recently, La Rocca et al. (2008) studied the dynamics of three-dimensional gravity currents moving on smooth and rough beds by full-depth lock exchange experiments and numerical simulations, using a 2D shallow water model together with the single layer approximation. They investigated gravity current's dynamics keeping constant the width of the sliding gate, the initial density of the lighter fluid and testing different values of initial density of the dense fluid,

initial height of the two fluids and the bed's roughness. They observed two different phases in three-dimensional gravity current's evolution: the front's velocity increases during the first phase and decreases during the second phase. La Rocca et al. (2008) suggested that these phases cannot be interpreted as slumping and self-similar phases, typical of two-dimensional and axisymmetric gravity currents. In fact as explained in section 1.2, the slumping phase is related to the backward flow of the upper layer of lighter fluid and to its reflection on the end-wall of the tank. As soon as the reflected wave overtakes the current's front, the gravity current starts to decelerate and the second self-similar phase starts. The geometrical configuration used in La Rocca et al. (2008) consists in a rectangular tank divided into two square section reservoirs of equal dimension by a vertical sliding gate, whose length is only a fraction of the total width of the tank. Therefore the backward-forward flow of the depression wave is influenced by the length of the gate, which chokes the flow and causes a configuration of permanent motion through the gate's opening; such a behavior does not allow the overtaking of the front by the depression wave and consequently the self-similar phase never starts. They also found that as the bed's roughness increases, the front's velocity during the second phase decreases. They observed a fairly good agreement in the velocity and front position between experimental and numerical results, although they observed a systematic discrepancy between them during the first instants of motion, which is attributed by the authors to the neglecting of the entrainment term in the mathematical model. Adduce et al. (2012) performed two-dimensional full-depth lock exchange experiments on a flat bed and compared experimental results with numerical simulations obtained by a two-layer, 1D shallow water model for miscible fluids. They carried out several laboratory experiments varying the lock position, the initial height of the two fluids and the initial density of the dense gravity current. Unlike several previous studies, Adduce et al. (2012) removed the rigid lid approximation, accounting for the free surface effects, and took into account also the entrainment between the two fluids. The latter is model by a modified Ellison & Turner's formula. The modeling of the mixing between the two fluids is a novelty, as shallow water models rarely presents this features. They proposed a comparison between numerical prediction with and without taking into account the entrainment, showing a better agreement with experimental results for the simulation performed for miscible fluids. Moreover, they showed the free surface effect, by comparing the numerical results obtained with the proposed model, accounting for both the free-surface oscillation and the mixing between the two layers, and single layer models with a rigid lid assumption. They compared experimental front's velocity, measured during the first slumping phase, with the one predicted by their model and previous expressions found in literature and they observed that the best agreement with experimental results is provided by using their own model. A recent paper by La Rocca et al. (2012) investigated the dynamics of a two-layer liquid, made of two immiscible

shallow-layers of different density within the framework of the Lattice Boltzmann Method (LBM). Results obtained from the LBM are compared with numerical results obtained with a two-layer shallow-water model, with experimental results and other numerical results published in literature. They observed that the prediction obtained by using the LBM and the one obtained with the shallow-water model can be considered almost equivalent and agree well with experimental results during the initial phase of the flow, when viscous forces are not involved in the evolution of the current. They also showed that the LBM is a valid tool to simulate gravity currents moving on beds with different slopes.

Several authors studied gravity current by the use of high resolution numerical models as LES (Ooi et al., 2007) or DNS (Härtel et al., 2000a-b; Cantero et al. 2006; Cantero et al. 2007). Such models provide a very detailed description of gravity current's dynamics, producing reliable results. However they are very complex and require high computational resources.

Some works were focused on measuring the velocity field during the slumping phase. Thomas & al. (2003) defined the two-dimensional structure of the head of inertial gravity currents during the slumping phase by digital Particle Tracking Velocimetry (PTV). They considered two-dimensional, high-Reynolds number turbulent flows moving on a flat bottom and they extracted the flow field by averaging each experiment in a given temporal interval. They observed the presence of two counter-rotating cells supplying dense fluid from the center of the current's head to the nose and suggested that both the intensity and the positions of these cells depends on the Reynolds number. Zhu & al. (2006) provided a detailed instantaneous velocity structure of two-dimensional lock release gravity currents in the slumping phase using a Particle Image Velocimetry (PIV) technique. They observed an upper positive vorticity strip located at the interface between the dense and the ambient fluid and a lower negative vorticity strip along the rigid bottom boundary. In a recent work, Martin & García (2009) obtained instantaneous and time averaged fields of both velocity and density of a steady density current by combining PIV and Planar Laser Induced Fluorescence (PLIF). In order to make the fluids optically uniform, while maintaining a density difference, they matched the index of refraction using, as solutes in water, sodium chloride and ethyl alcohol for the dense and the ambient fluid, respectively. They observed the generation of persistent billows associated with Kelvin-Helmholtz instabilities.

Alahyari & Longmire (1994) focused the attention on the problem associated with variation in the index of refraction within two fluids. Such problem often affects application of PIV. In fact, the direction of the light scattered from seed particles within the fluid, depends on the local refractive index and on the angle formed at the interface between the two fluids with different densities. Such effect can cause a blurred image in which particles cannot be distinguished. Therefore they suggested an index matching strategy based on glycerol and

potassium dihydrogen phosphate (monobasic) as solutes in water rather than sodium chloride and ethyl alcohol as the latter is difficult to use in facilities with large free surface, due to its high volatility. They recommend the use of glycerol, because it is clear, odorless and miscible in water and it does not evaporate or react with air. Alahyari & Longmire (1996) applied the described index matching strategy to study axisymmetric laboratory gravity currents by PIV technique. Some other details about index matching strategy will be provided in section 2.3.

2. 2D gravity currents

2.1. Laboratory experiments

2.1.1. Experimental set-up

The experiments were performed at the Hydraulics Laboratory of University of Rome "Roma Tre". Gravity currents were generated using a common technique widely used in literature, called *lock-exchange release*: a tank is divided by a vertical sliding gate into two reservoirs, filled with the lock fluid (i.e. heavier fluid) and with the ambient fluid (i.e. lighter fluid), respectively, as shown in the sketch of the experimental apparatus (Figure 2.1) and in the picture of the used tank (Figure 2.2). When the gate is removed, as suddenly as possible, the two fluids with different densities come in contact and a non-equilibrium condition occurs. Therefore the heavier fluid collapses flowing under the lighter one and forming the gravity current. The main features of lock exchange release technique are provided in section 1.2.

In this work compositional gravity currents were performed, using a solution of tap water and sodium chloride (*NaCl*) as lock fluid, and tap water as surrounding fluid. Two-dimensional lock release gravity currents were generated in a transparent Plexiglas tank of rectangular cross-section, of depth 0.3 m, length 3.00 m and width 0.20 m. The sliding vertical gate was placed at a distance x_0 from the left end wall of the tank. The right volume of the tank, called *lock*, was filled with fresh water of density ρ_2, while the rest of the tank was filled with salty water with initial density $\rho_{01} > \rho_2$. As we performed the so-called full-depth lock exchange release experiments, both in the right and in the left part of the tank the depth of the fluid was h_0 and the ratio of the initial gravity current height h_0 to the total height of the two fluids H, called fractional depth ϕ, is such that $\phi = 1$. A pycnometer was used to perform density measurements. The uncertainty in the density measurements was estimated as 0.2 %. Some dye was dissolved into the salty water in order to provide the flow visualization during the experiment. The experiment starts when the sliding gate is suddenly removed and the heavier fluid moves from the left part of the tank to the right part forming the gravity current. The experiment stops when the front of the gravity current reaches the right end wall of the tank.

A CCD (Charged Coupled Device) camera, with a frequency of 25 Hz, was used to record the experiments and an image analysis technique, based on the threshold method, was applied to measure the space-time evolution of the gravity currents' profiles. Each frame of the movie acquired by the camera is a

rectangular matrix (576 × 768 pixels) of integers representing the gray level of the corresponding pixel and ranging from 0 (black) to 255 (white). The grey level of the interface between the two fluids was chosen as the threshold value. Therefore the threshold value is a calibration parameter of the code, which has to be chosen in order to obtain as output a current's profile in agreement with acquired images. A program written in MatLab language travelled along the columns of the matrix (i.e. the image) until it met the threshold value (i.e. the interface between the two fluids) and recorded the coordinates of this pixel as a point of the current's profile. A rule was positioned along both the horizontal and vertical walls of the tank in order to obtain the conversion factor pixel/cm. The front position x_f is determined within an error of 0.2 cm. The experimental profiles measured by the threshold method, together with the images captured by the camera, at four different time steps for one of the performed runs (Run 2D_9) are shown in Figure 2.3.

The tank was placed on an inclinable structure, in order to obtain the desired sloping angle ϑ for the experiments performed on upsloping beds. For the upsloping configuration the height of the two fluids h_0 was measured at the gate position x_0 as shown in Figure 2.1.

Regarding the runs performed on rough bed, the desired roughness was obtained by gluing sand of a defined mean diameter (D_{50}) on the bottom of the tank.

2.1.2. Experimental parameters

Twenty-six 2D lock release gravity currents were carried out. The experimental parameters used for the experiments are shown in Table 1. Among these, seventeen experiments (Runs 2D_1-2D_17) were performed on a flat bed: the runs 2D_1-2D_5 were realized on a flat smooth bed keeping constant ρ_2=1000 Kg/m^3, h_0=0.15 m, x_0=0.10 m and testing five values of initial density of the lock fluid $\rho_{01}\cong$1009, 1024, 1039, 1060 and 1090 Kg/m^3 corresponding to different values of the dimensionless ratio $r=\rho_2/\rho_{01}$; the runs 2D_6-2D_17 were performed on a flat rough bed keeping constant ρ_2=1000 Kg/m^3, h_0=0.15 m, x_0=0.10 m and testing four values of $\rho_{01}\cong$1009, 1024, 1039 and 1060 Kg/m^3 and three values of the bed's roughness ε=0.7, 2.2 and 4.5 mm. A dimensionless bed's roughness was defined as the ratio $\varepsilon^*=\varepsilon/h_0$. For the runs performed on rough beds ε^* was equal to 0.0047, 0.0147 and 0.03.

Nine experiments (runs 2D_18-2D_26) were performed on a smooth and upsloping bed, keeping constant ρ_2=1000 kg/m^3, h_0=0.15 m, x_0=0.1 m and testing three different values of $\rho_{01}\cong$1039, 1060 and 1090 Kg/m^3 and varying the angle ϑ between the bed and the horizontal. For each density value the critical bed's angle was found. In this work the critical angle is defined as the angle for which the gravity current reaches the end of the tank with a front's speed close

to zero. Then subcritical and supercritical bed's angles for each density were found. The subcritical bed's angle is the angle for which the gravity current reaches the end wall with a front's speed higher than zero, while the subcritical bed's angle is the one for which the current doesn't reach at all the end of the tank
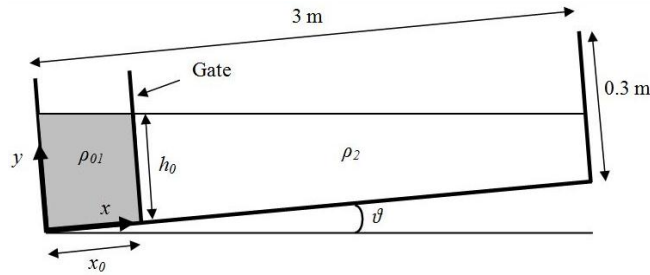
Figure 2.1: Sketch of the tank used to perform 2D lock release gravity currents.
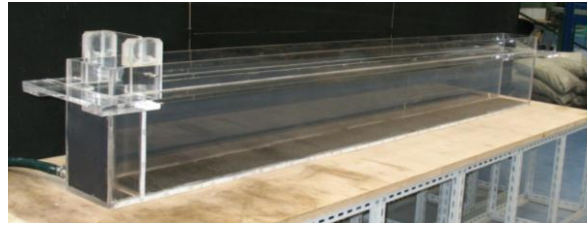
Figure 2.2: Picture of the tank used to perform 2D lock release gravity currents.
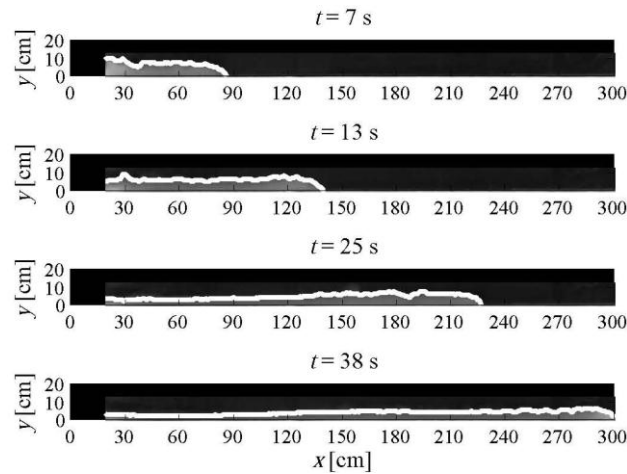
Figure 2.3: Measured profiles (white line) overlapping the images captured by the camera for the run 2D_9 at 7, 13, 25 and 38 s after the removal of the gate.

Run	x_0 [m]	h_0 [m]	ρ_{01} [Kg/m^3]	ε [mm]	$r = \rho_2/\rho_{01}$	$\varepsilon^* = \varepsilon/h_0$	ϑ [°]	Angle
2D_1	0.1	0.15	1009.25	0.0	0.991	0.0000	0.00	-
2D_2	0.1	0.15	1023.70	0.0	0.977	0.0000	0.00	-
2D_3	0.1	0.15	1039.54	0.0	0.962	0.0000	0.00	-
2D_4	0.1	0.15	1059.56	0.0	0.944	0.0000	0.00	-
2D_5	0.1	0.15	1089.99	0.0	0.917	0.0000	0.00	-
2D_6	0.1	0.15	1009.15	0.7	0.991	0.0047	0.00	-
2D_7	0.1	0.15	1009.24	2.2	0.991	0.0147	0.00	-
2D_8	0.1	0.15	1008.75	4.5	0.991	0.0300	0.00	-
2D_9	0.1	0.15	1024.06	0.7	0.976	0.0047	0.00	-
2D_10	0.1	0.15	1024.36	2.2	0.976	0.0147	0.00	-
2D_11	0.1	0.15	1023.73	4.5	0.977	0.0300	0.00	-
2D_12	0.1	0.15	1038.90	0.7	0.963	0.0047	0.00	-
2D_13	0.1	0.15	1038.68	2.2	0.962	0.0147	0.00	-
2D_14	0.1	0.15	1039.47	4.5	0.962	0.0300	0.00	-
2D_15	0.1	0.15	1060.56	0.7	0.943	0.0047	0.00	-
2D_16	0.1	0.15	1060.00	2.2	0.943	0.0147	0.00	-
2D_17	0.1	0.15	1059.47	4.5	0.944	0.0300	0.00	-
2D_18	0.1	0.15	1038.59	0.0	0.963	0.0000	0.90	Subcritical
2D_19	0.1	0.15	1038.59	0.0	0.963	0.0000	1.11	Critical
2D_20	0.1	0.15	1039.10	0.0	0.962	0.0000	1.39	Supercritical
2D_21	0.1	0.15	1059.72	0.0	0.944	0.0000	1.14	Subcritical
2D_22	0.1	0.15	1059.75	0.0	0.944	0.0000	1.39	Critical
2D_23	0.1	0.15	1059.72	0.0	0.944	0.0000	1.52	Supercritical
2D_24	0.1	0.15	1089.99	0.0	0.917	0.0000	1.39	Subcritical
2D_25	0.1	0.15	1090.10	0.0	0.917	0.0000	1.45	Critical
2D_26	0.1	0.15	1089.88	0.0	0.917	0.0000	1.8	Supercritical

Table 1: Experimental parameters used to perform 2D gravity currents.

2.1.3. Experimental results

2.1.3.1. Flat smooth bed

In Figure 2.4a-b experimental front's positions versus time are shown for all the experiments performed on flat smooth bed (i.e. Runs 2D_1-2D_5), in dimensional and dimensionless form, respectively. All the runs shown in this

section are performed keeping constant h_0 and x_0 and testing five different values of ρ_{01}. The values of the experimental parameters are shown in Table 1. All the laboratory measurements starts about two seconds after the removal of the sliding gate, because it was difficult to measure the profile of the current during its initial stage of development.

Dimensionless front position x_f^* is defined as:

$$x_f^* = \frac{x_f - x_0}{x_0} \tag{21}$$

Dimensionless time T^* is defined on the basis of the time scale t_0 as:

$$T^* = \frac{t}{t_0}; \quad t_0 = \frac{x_0}{\sqrt{g_0' h_0}} \tag{22}$$

where g'_0 is the initial reduced gravity, given by:

$$g'_0 = g \frac{\rho_{01} - \rho_2}{\rho_2} \tag{23}$$

in which g is the gravity acceleration. Figure 2.4a shows that the speed of the current increases as the initial density of released current increases. For a constant time, the gravity current with higher initial density covers a longer distance than those realized with lower values of initial density. Figure 2.4b shows that all the time histories of the front position in dimensionless form of relative to the runs performed with different values of the initial density of the gravity current and keeping constant the other experimental parameters lye all on the same curve. Such a result is in agreement with most of the studies about gravity currents, as Marino et al. 2005. Figure 2.5a-c shows the comparisons of current profiles for all the runs performed on flat smooth bed, at three different time steps after release of the dense fluid, $t=12$ s (Figure 2.5a), $t=20$ s (Figure 2.5b) and $t=24$ s (Figure 2.5c), respectively. As observed in Figure 2.4a, as the initial density of the dense fluid increases, the current's speed increases.

As explained in section 1.2, Huppert & Simpson (1980) and Rottman & Simpson (1983) showed that three phases can be distinguished in the dynamics of a gravity current produced by an instantaneous release. As they investigated gravity currents moving on flat and smooth beds, in the present work the length of the three phases can be computed only for runs 2D_1-2D_5. The length of the

slumping phase l_s can be calculated following Rottman & Simpson (1983) by Equation (5). The distance at which the viscous phase starts l^* is calculated following Huppert (1982) by Equation (6). The length of the viscous phase l_{vis} is given by the difference between the total length of the tank and the distance at which the third phase starts. The length of the self-similar phase l_{ss} can be obtained by the difference between l^* and l_s. In Table 2 l_s, l_{ss}, l_{vis} for runs 2D_1-2D_5 are shown.

Run	ρ_{01} [Kg/m^3]	l_s [m]	l_{ss} [m]	l_{vis} [m]
2D_1	1009.25	1.00	0.82	1.18
2D_2	1023.70	1.00	1.10	0.90
2D_3	1039.54	1.00	1.25	0.75
2D_4	1059.56	1.00	1.39	0.61
2D_5	1089.99	1.00	1.53	0.47

Table 2 Lengths of slumping phase l_s, self-similar phase l_{ss} and viscous phase l_{vis} for all the runs performed on flat and smooth beds.
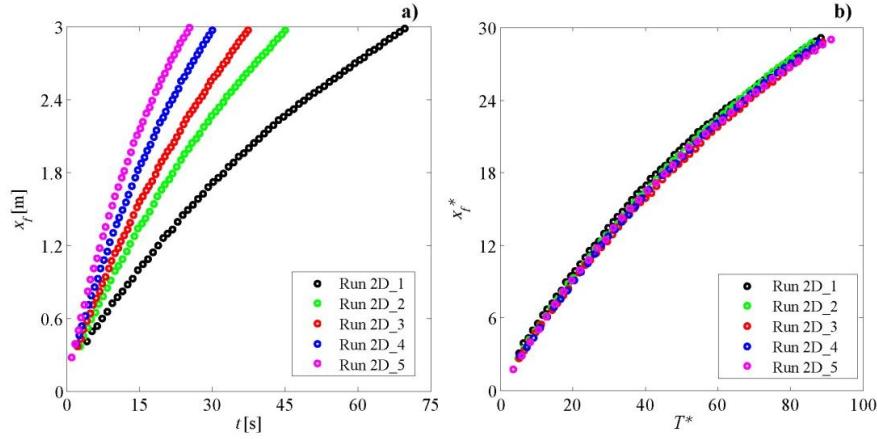
Figure 2.4a-b: Dimensional and dimensionless plots of front position versus time for the runs 2D_1-2D_5, performed on flat smooth bed with different initial densities.

Figure 2.6 show a comparison between experimental front position versus time of runs that runs 2D_1-2D-5 and theoretical front evolution for the three phases given by previous studies. It can be observed that during the first phase, experimental data are placed on a line with slope 1 (solid line), while during the second self-similar phase are on the line with slope 2/3 (dashed line). The third line (dotted line) has a slope of 1/5 and should be followed by data points

corresponding to the third viscous phase. However, although by using laws from Rottman & Simpson (1983) and Huppert (1982) it can be predicted that runs 2D_1-2D_5 develop the three phases during their evolution, the log-log plot shows in Figure 2.6 shows that these experimental data are in agreement with previous formulae only for the first and the second phase, while the third phase seems not to occur in the current's evolution. It can be supposed that the length of the viscous phase should be longer than the ones occurring in the dynamics of runs 2D_1-2D_5 in order to be observable in experimental results. Moreover Equation (7) was derived by Huppert (1982), on the basis of some hypothesis, among which the hypothesis of immiscibility of the two fluids, while entrainment phenomena are involved in the gravity currents' dynamics analyzed in this work, as will be fully shown in section 2.3.3.
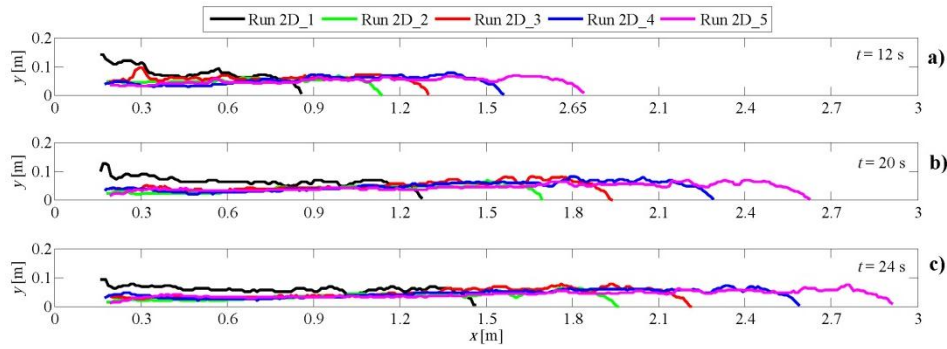
Figure 2.5a-c: Measured gravity current's profiles at three different time steps for the runs 2D_1-2D_5, performed on a flat smooth bed with different initial densities.
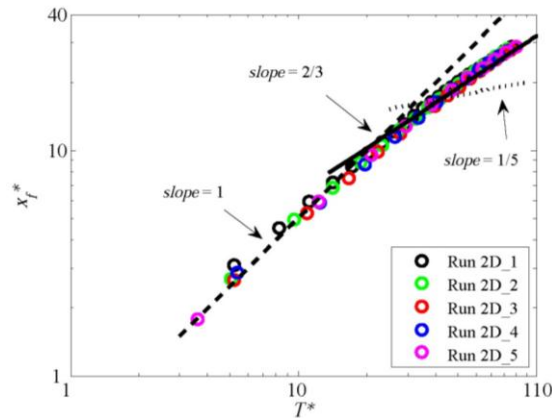
Figure 2.6: Dimensionless log-log plot of front's position versus time for the runs performed on flat and smooth beds. Dashed line, solid line and dotted line are the theoretical front evolution for the slumping, self-similar and viscous phase, respectively.

2.1.3.2. Rough flat bed

In Figure 2.7a-h experimental front's positions versus time are shown for all the performed runs on a rough flat bed in both dimensional and dimensionless form. Space scale and time scale are the same used for the dimensionless plots shown in Figure 2.4a-b.

Each plot in Figure 2.7a-h shows a comparison between the runs performed with the same value of initial density of released current and different values of bed's roughness, including the run realized on smooth bed. Experimental parameters are shown in Table 1.

Figure 2.8a-d shows the measured gravity current's profiles obtained with the threshold's method for the same runs at three different time steps $t=12$ s, $t=20$ s and $t=30$ s.

The observed general trend is that the speed of the gravity currents decreases as the bed roughness increases. In particular as the initial density of the heavier fluid increases, a decrease of the decelerating effect due to the bed's roughness can be observed. However a superimposition of some runs in Figure 2.7a-h can be observed. Hence the following couples of runs are overlapped: 2D_1-2D_6 (Figure 2.7a-e), 2D_9-2D_10 (Figure 2.7b-f), 2D_3-2D_12 (Figure 2.7c-g), 2D_13-2D_14 (Figure 2.7c-g) and 2D_16-2D_17 (Figure 2.7d-h). This behavior can be due to the fact that the rough bottom was separately prepared for each experiment. In fact, as previously touched on, the bed's roughness was obtained by gluing sediments of defined mean diameter on the bottom of the tank. In order to avoid the damage of the rough bottom due to the removal of the colored salty water at the end of each experiment, a new rough bed was set up for each run. The glue used to obtain a fixed rough bottom could have someway covered part of the sediments, leading to values of bed's roughness smaller than the desired one. Hence, as a new rough bed was prepared for each experiment, such an effect could be different for each run. In order to verify if the overlapping of the curves in Figure 2.7a-h is due to such a procedure of setting up the rough bottom, additional laboratory experiments with a fixed rough bed for each set of runs should be performed.
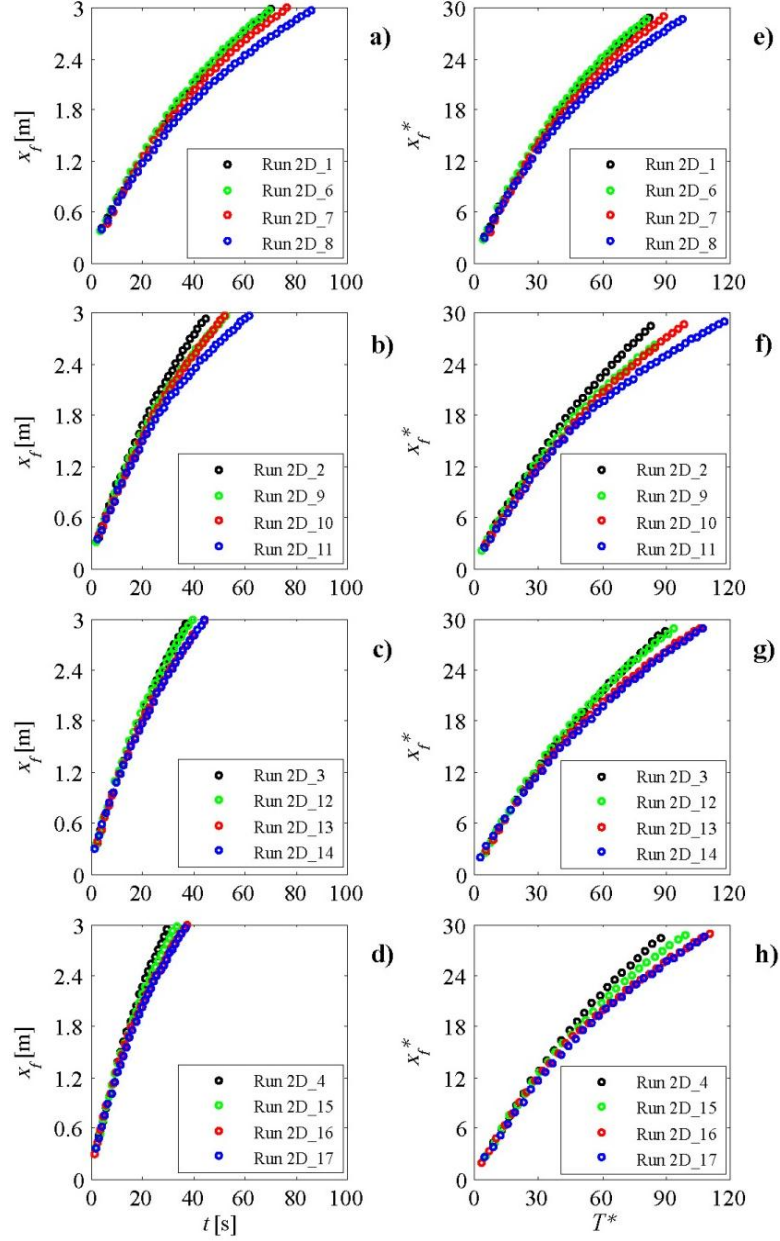
Figure 2.7a-h: Dimensional and dimensionless plot of front position versus time for all the runs performed on rough and smooth flat beds; (a-d) Runs 2D_1-2D_6-2D_7-2D_8: $\rho_{01} \cong 1009$ Kg/m^3, ε=0.0, 0.7, 2.2 and 4.5 mm; (b-e) Runs 2D_2-2D_9-2D_10-2D_11: $\rho_{01} \cong 1024$ Kg/m^3, ε=0.0, 0.7, 2.2 and 4.5 mm; (c-f) Runs 2D_3-2D_12-2D_13-2D_14: $\rho_{01} \cong 1039$ Kg/m^3, ε=0.0, 0.7, 2.2 and 4.5 mm; (d-g) Runs 2D_4-2D_15-2D_16-2D_17: $\rho_{01} \cong 1060$ Kg/m^3, ε=0.0, 0.7, 2.2 and 4.5 mm.
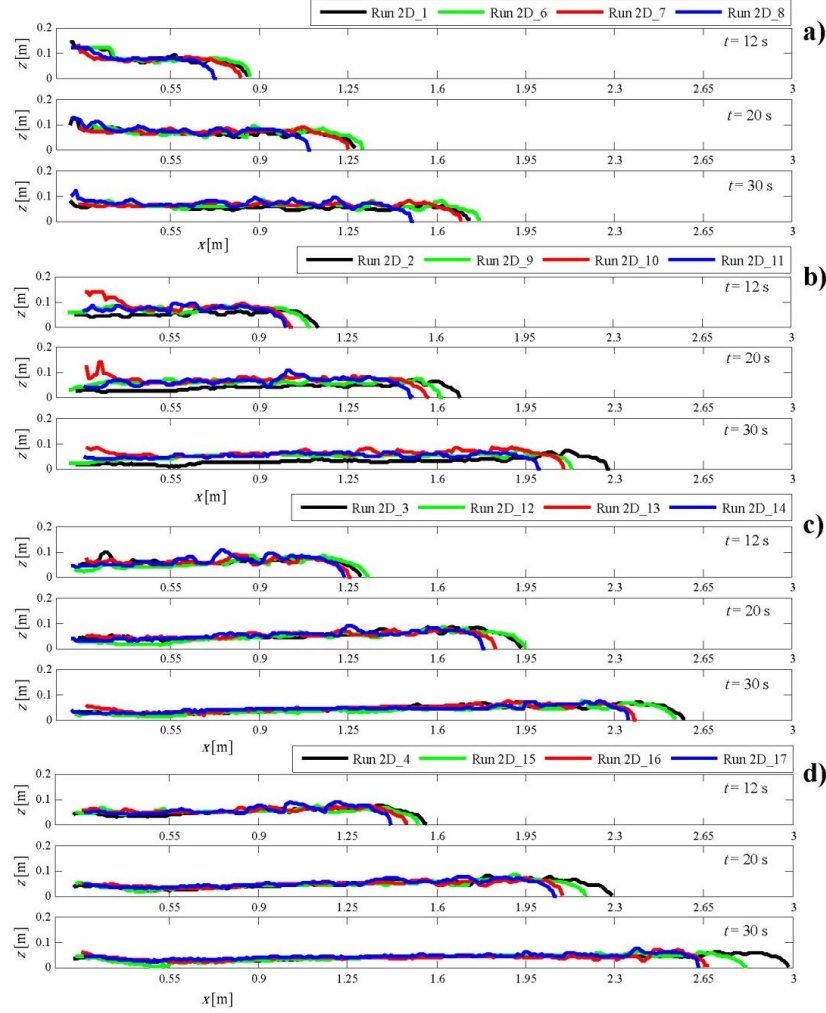
Figure 2.8a-d: Measured gravity current's profiles at three different time steps for all the runs performed on rough and smooth flat beds; (a) Runs 2D_1-2D_6-2D_7-2D_8: $\rho_{01} \cong 1009$ Kg/m^3, ε=0.0, 0.7, 2.2 and 4.5 mm; (b) Runs 2D_2-2D_9-2D_10-2D_11: $\rho_{01} \cong 1024$ Kg/m^3, ε=0.0, 0.7, 2.2 and 4.5 mm; (c) Runs 2D_3-2D_12-2D_13-2D_14: $\rho_{01} \cong 1039$ Kg/m^3, ε=0.0, 0.7, 2.2 and 4.5 mm; (d) Runs 2D_4-2D_15-2D_16-2D_17: $\rho_{01} \cong 1060$ Kg/m^3, ε=0.0, 0.7, 2.2 and 4.5 mm.

2.1.3.3. Upsloping smooth bed

Figure 2.10a-f show experimental front's positions versus time for all the runs performed on upsloping smooth bed in dimensional and dimensionless form.

Valentina Lombardi

Space scale and time scale are the same used for dimensionless plots shown in Figure 2.4a-b. Each plot in Figure 2.10a-f shows a comparison between the runs performed with the same value of initial density of the released current and different values of the angle ϑ, including the run realized on flat bed. Experimental parameters are shown in Table 1. Figure 2.10a-f shows that the current's speed decrease as the angle ϑ increases. Gravity currents realized with critical and subcritical angle ϑ reach the end of the tank, while runs performed with supercritical angles stops before the end wall of the tank.

In Figure 2.9a-c the measured current's profiles for the same experiments are shown and a decrease of the current's speed can be observed, increasing the angle ϑ.
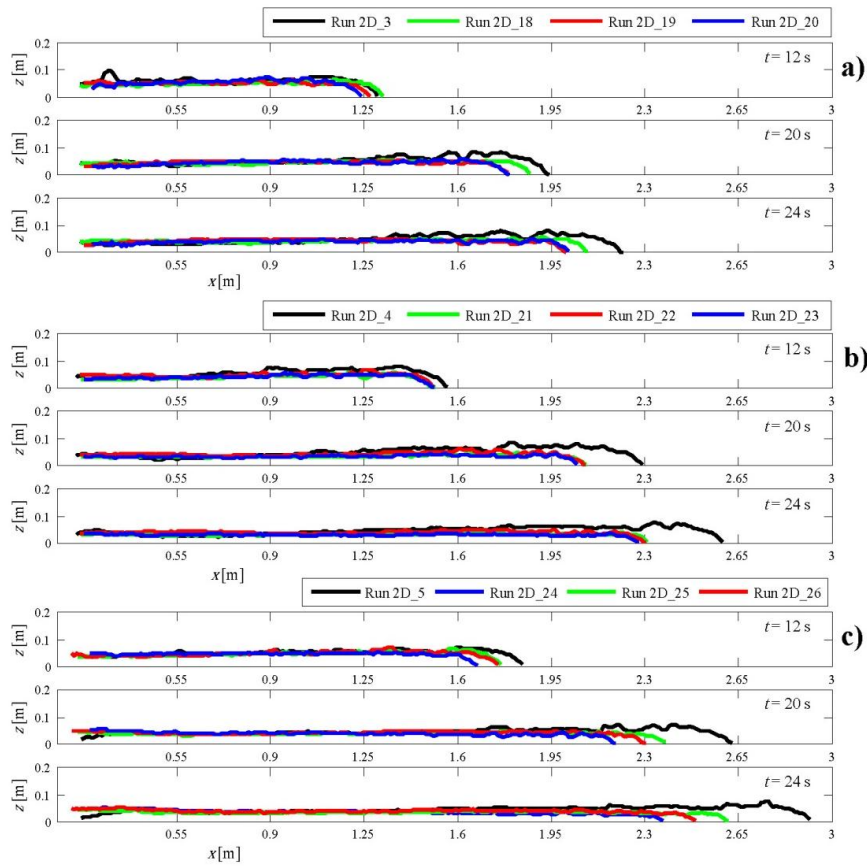
Figure 2.9a-c: Measured gravity current's profiles at three different time steps for all the runs performed on flat and upsloping smooth beds; (a) Runs 2D_3-2D_18-2D_19-2D_20: $\rho_{01}\cong1039$ Kg/m^3, ϑ=0.0°, 0.90°, 1.11° and 1.39°; (b) Runs 2D_4-2D_21-2D_22-2D_23: $\rho_{01}\cong1060$ Kg/m^3, ϑ=0.0°, 1.14°, 1.39° and 1.52°; (c) Runs 2D_5-2D_24-2D_25-2D_26: $\rho_{01}\cong1090$ Kg/m^3, ϑ=0.0°, 1.39°, 1.45° and 1.8°.
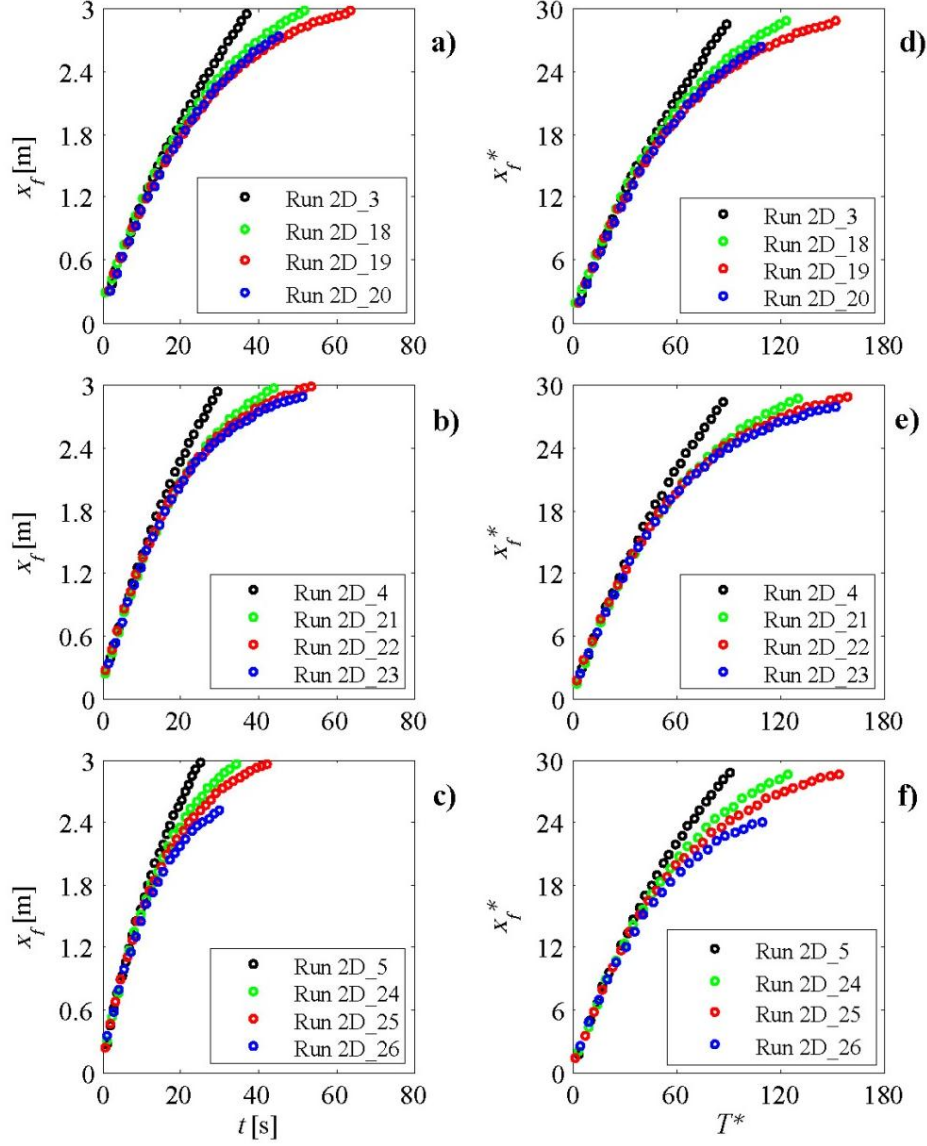
Figure 2.10a-f: Dimensional and dimensionless plots of front position versus time for all the runs performed on flat and upsloping smooth beds; (a-d) Runs 2D_3-2D_18-2D_19-2D_20: $\rho_{01} \cong 1039$ Kg/m^3, ϑ=0.0°, 0.90°, 1.11° and 1.39°; (b-e) Runs 2D_4-2D_21-2D_22-2D_23: $\rho_{01} \cong 1060$ Kg/m^3, ϑ=0.0°, 1.14°, 1.39° and 1.52°; (c-f) Runs 2D_5-2D_24-2D_25-2D_26: $\rho_{01} \cong 1090$ Kg/m^3, ϑ=0.0°, 1.39°, 1.45° and 1.8°.

2.2. 1D numerical simulations

2.3.1. Mathematical model

A two-layer, one-dimensional, shallow-water model developed by Adduce et al. (2012) was used to simulate gravity currents. Gravity currents frequently develop along the longitudinal direction, therefore the ratio between the depth and the length of the current is small enough to allow the application of the shallow water theory. Several authors investigated gravity currents by shallow water equations (Rottman and Simpson, 1983; Sparks et al., 1993; Klemp et al., 1994; Shin et al., 2004). Such authors used a rigid lid assumption, while in the present work the free surface is modeled as a moving impermeable boundary, with a constant pressure distribution as a dynamical constraint, following Adduce et al. 2012. Previous models are governed by a smaller number of equations, but although they are simpler than the present model, they are also less similar to the real physical phenomenon. Modeling the space-time evolution of the free surface ensures a more realistic simulation of the studied phenomenon. Moreover the mathematical model takes into account the entrainment between the two fluids. Therefore the interface is modeled as a moving permeable boundary, through which a given fluid volume, estimated by the entrainment velocity V_e, flows from the upper layer of lighter fluid to the lower layer of heavier fluid. Such flow of clear water which crosses the boundary between causes a decrease of the density of the gravity current.

A sketch of the frame of reference used for the mathematical model is shown in Figure 2.11. A one-dimensional gravity current moving on a bed forming with the horizontal an angle ϑ is considered. For the mathematical model, negative values of ϑ are referred to upsloping beds. The heavier current of height $h_1(x,t)$ and density ρ_1 flows below the lighter one of height $h_2(x,t)$ and density ρ_2 bounded at the top by a free surface.
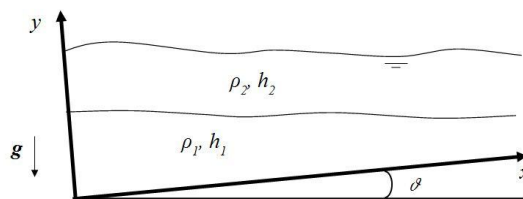
Figure 2.11: Frame of reference used in the mathematical model.

Applying the principle of mass conservation and projecting along the *x*-axis the momentum equations, the following hyperbolic system of partial differential equations is obtained:

$$\begin{cases} \dfrac{\partial(\rho_1 h_1)}{\partial t} + \dfrac{\partial(\rho_1 V_1 h_1)}{\partial x} = \rho_2 V_e \\[2ex] \dfrac{\partial(\rho_2 h_2)}{\partial t} + \dfrac{\partial(\rho_2 V_2 h_2)}{\partial x} = -\rho_2 V_e \\[2ex] \dfrac{\partial V_1}{\partial t} = g\sin\theta - \dfrac{\partial}{\partial x}\left(\dfrac{\rho_1 h_1 + \rho_2 h_2}{\rho_1} g\cos\theta + \dfrac{V_1^2}{2} \right) - \dfrac{\tau_{1b} + \tau_{12}}{\rho_1 h_1} \\[2ex] \dfrac{\partial V_2}{\partial t} = g\sin\theta - \dfrac{\partial}{\partial x}\left((h_1 + h_2)g\cos\theta + \dfrac{V_2^2}{2} \right) + \dfrac{\tau_{12} + \tau_{2b}}{\rho_2 h_2} \end{cases} \qquad (24)$$

where the unknown quantities h_1, h_2, V_1 and V_2 are the depth and the velocity of the lower and the upper layer, respectively, V_e is the entrainment velocity, τ_{1b} and τ_{2b} are the shear stress between the two fluids and the bottom. These terms include both the shear stress due to the bottom and side walls for the lower layer and the shear stress due to side walls for the upper layer. τ_{12} is the shear stress at the interface between the two fluids defined following the relation suggested by Supino (1981) as:

$$\tau_{12} = \tau_{21} = \lambda_{\text{int}} \frac{\rho_1 + \rho_2}{2} \frac{(V_2 - V_1)|V_2 - V_1|}{8} \qquad (25)$$

Several runs were performed to calibrate the friction factor at the interface λ_{int}. The value $\lambda_{\text{int}}=0.24$ was found as calibration value and it was used for all the simulations. Both τ_{1b} and τ_{2b} are modeled by the Darcy-Weisbach's formula (Darcy, 1857; Weisbach, 1845), as in La Rocca et al. (2008):

$$\begin{aligned} \tau_{1b} &= \lambda_1 \rho_1 \frac{V_1|V_1|}{8} \frac{(2h_1 + b)}{b} \\[2ex] \tau_{2b} &= \lambda_2 \rho_2 \frac{V_2|V_2|}{8} \frac{(2h_2)}{b} \end{aligned} \qquad (26)$$

where λ_1 and λ_2 are the friction factors for the lower and the upper layer respectively and b is the width of the tank. The definition of the general λ_i for the i_{th} layer is given by the Colebrook' relation (Colebrook, 1939) as:

Valentina Lombardi

$$\lambda_i = \lambda_{i\infty}\left(1 + \frac{8h_i}{\text{Re}_i\,\varepsilon}\right) \tag{27}$$

where $\lambda_{i\infty}$, Re_i and ε/h_i are the friction factors for turbulent rough flows, the local Reynolds number and the relative roughness of the i_{th} layer, respectively. $\lambda_{i\infty}$ and Re are defined as:

$$\lambda_{i\infty} = \frac{1}{4}\left[\log\left(\frac{3.71h_i}{\varepsilon}\right)\right]^{-2} \tag{28}$$

$$\text{Re}_i = \frac{V_i h_i}{v_i} \tag{29}$$

Equation (27) shows that the term $8h_i/\text{Re}_i\,\varepsilon$ adapts the friction factor for turbulent rough flows to turbulent transition flows. In the performed experiments turbulent transition flows develop.

On the basis of Ellison & Turner's (1959) laboratory experiments, Turner (1986) defined the entrainment as a function of the Froude number suggesting the following relation:

$$\frac{V_e}{|V_1|} = \begin{cases} \dfrac{0.08Fr^2 - 0.1}{Fr^2 + 5} & Fr^2 \geq 1.25 \\[3mm] 0 & Fr^2 < 1.25 \end{cases} \tag{30}$$

in which $V_e/|V_1|$ is the entrainment coefficient and Fr is the local densimetric Froude number of the dense fluid and is given by:

$$Fr = \frac{V_1}{\sqrt{h_1 \dfrac{\rho_1 - \rho_2}{\rho_1} g \cos\theta}} \tag{31}$$

Because Ellison & Turner's formula was obtained by an experimental apparatus different from the lock exchange release experiment used for the present work,

some modifications to Ellison & Turner's relation were adopted as in Adduce et al. (2012). First of all, the threshold on squared Froude number was removed, as in the gravity currents investigated in this work, squared Froude numbers rarely reach values higher than 1.25, and the use of Equation (30) would often provide a null result for the term $V_e/|V_1|$. Moreover the coefficient 0.08 was substituted by a dimensionless parameter k and the term 0.1 was fixed to zero, in order to avoid negative values of the entrainment term in the case in which $Fr^2 \leq 0.1/k$. The relation suggested by Adduce et al. (2012) is used in this work to model the entrainment coefficient:

$$\frac{V_e}{|V_1|} = \frac{k \cdot Fr^2}{Fr^2 + 5} \tag{32}$$

where k is the dimensionless coefficient to be calibrated. The entrainment velocity increases as k increases. The calibration value of k has to balance a correct evaluation of the gravity current's depth and a good simulation of the front's speed of the gravity current. Several tests were performed with different values of the dimensionless parameter k, in order to obtain the calibration value. The calibration of k is necessary because Equation (32) doesn't take into account that the entrainment coefficient $V_e/|V_1|$ depends not only on the densimetric local Froude number but also on the Reynolds number of the gravity current (Cenedese & Adduce, 2008). Moreover the empirical formula used in this work is a first attempt to model the entrainment in the shallow water framework.

2.3.2. Numerical method

The conservation form of the system (24) is obtained by assuming the following hypothesis: the density of the ambient fluid ρ_2 is considered to be constant; the density of the dense fluid depends on time, but not on space. Therefore system (24) can be expressed by the following conservation form:

$$\frac{\partial U}{\partial t} + \frac{\partial F(U)}{\partial x} = E(U) \tag{33}$$

where U is the vector of the conserved variables and is given by:

$$U \equiv \left\{ \rho_1 h_1, \rho_2 h_2, V_1, V_2 \right\} \tag{34}$$

$F(U)$ and $E(U)$ are vectors, whose components are expressed in terms of U and are given by the following expressions:

$$F(U) \equiv \left\{ \rho_1 V_1 h_1, \rho_2 V_2 h_2, \frac{V_1^2}{2} + \left(\frac{\rho_1 h_1 + \rho_2 h_2}{\rho_1} \right) g \cos\theta, \right.$$
$$\left. \frac{V_2^2}{2} + \left(\frac{\rho_1 h_1}{\rho_1} + \frac{\rho_2 h_2}{\rho_2} \right) g \cos\theta \right\} \tag{35}$$

$$E(U) \equiv \left\{ \rho_2 V_e, -\rho_2 V_e, g \sin\theta - \frac{\tau_{1b} + \tau_{12}}{\rho_1 h_1}, g \sin\theta + \frac{\tau_{2b} + \tau_{12}}{\rho_2 h_2} \right\} \tag{36}$$

The conservation form given by system (24) imposes energy conservation across the front wave, which is a quite realistic assumption for several kinds of gravity currents (Benjamin, 1968; Shin et al. 2004).

The conservation form allows the application of numerical methods, characterized by shock fitting and shock capturing features, which are suitable for simulating wave propagation with internal discontinuities. By the expression of Equation (33) in matrix form, the following relation can be obtained:

$$\frac{\partial U}{\partial t} + A \frac{\partial U}{\partial x} = E(U) \tag{37}$$

In which $A = dF/dU$ is the coefficients' matrix, which shows complex eigenvalues only when the variables in U reach extreme values, never observed in the regime of interest. Therefore the system can be classified as hyperbolic and an explicit Mac-Cormack' finite difference scheme by predictor-corrector method was applied.

The explicit formulation of the used scheme is the following:

$$U_j^p = U_j^n - \left(\frac{dt}{dx}\right)\left[F\left(U_j^n\right) - F\left(U_{j-1}^n\right)\right] + dt E\left(U_j^n\right) \qquad (38)$$

$$U_j^c = U_j^p - \left(\frac{dt}{dx}\right)\left[F\left(U_{j+1}^p\right) - F\left(U_j^p\right)\right] + dt E\left(U_j^p\right) \qquad (39)$$

$$U_j^{n+1} = \frac{U_j^n + U_j^c}{2} \qquad (40)$$

In which p and c denote the predictor and corrector steps and j refers to the index of spatial grid points. Figure 2.12 shows a sketch of grid points involved in a predictor-corrector step. The used method starts with the predictor step, corresponding to time $t=n+1$, in which forward difference and backward difference for temporal and spatial derivatives respectively are applied, as shown in Figure 2.12 where the red triangle's vertexes are the points involved in the Equation (38). Then the corrector step, corresponding to time $t=n+2$, applies forward difference and backward difference for spatial and temporal derivatives, respectively, involving in the computation the grid points indicated in Figure 2.12 by the orange triangle's vertexes. Therefore at each time step the sequence of backward and forward difference for spatial derivatives is reversed. The final result at $t=n+1$ for $x=j$ is given by the average between the values at $t=n$ and $t=n+2$, indicated in Figure 2.12 by the green circle, and expressed by Equation (40).
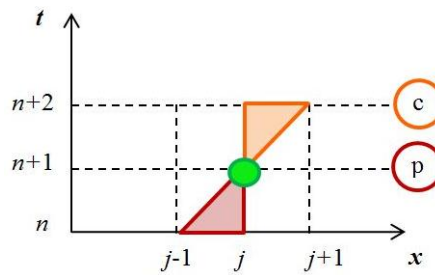
Figure 2.12: Sketch of grid points involved in a predictor-corrector step.

The spatial grid size is $dx=0.015$ m and the time step dt is given by the stability condition $dt \leq dx/\Lambda$, in which Λ is the maximum absolute value of the eigenvalues of the matrix A.

2.3.3. Comparison between experimental and numerical results

The entrainment coefficient given by Equation (32) depends on the dimensionless parameter k, which needs to be calibrated. As k increases, the entrainment term also increases, causing two different effects in the miscible current's dynamics. On one hand the increase of k causes a decrease of the current's density, decelerating the flow; on the other hand however, as the effect of the entrainment phenomenon is to produce a mass transport form the lighter fluid to the heavier one, the height of the current increases causing an acceleration of the flow.

Several preliminary simulations were performed in order to obtain for each run the calibration value of k, which should ensure a good evaluation of both the current's height and the front's speed.

As previously explained, the calibration of k is necessary because the equation used to model the entrainment in this work accounts for the dependence between the entrainment coefficient and the densimetric local Froude number, without involving in the relation the Reynolds number. Cenedese & Adduce (2008) found that the entrainment coefficient is dependent not only on Froude number, as assumed in previous studies, but also on Reynolds number. Moreover Equation (32) is an empirical formula, which is a first attempt used to model the entrainment in the shallow water framework. As a consequence different calibration values of k were found. Table 3 shows calibration values obtained for all the runs performed on smooth flat and upsloping beds.

Run	ρ_{01} [Kg/m^3]	ε [m]	$r = \rho_2/\rho_{01}$	ϑ [°]	k	Angle
2D_3	1039.54	0.0	0.962	0.00	0.6	-
2D_18	1038.59	0.0	0.962	0.90	0.8	Subcritical
2D_19	1038.59	0.0	0.962	1.11	0.9	Critical
2D_20	1039.10	0.0	0.962	1.39	1.1	Supercritical
2D_4	1059.56	0.0	0.943	0.00	0.6	-
2D_21	1059.72	0.0	0.943	1.14	0.9	Subcritical
2D_22	1059.75	0.0	0.943	1.39	1.1	Critical
2D_23	1059.72	0.0	0.943	1.52	1.1	Supercritical
2D_5	1089.99	0.0	0.917	0.00	0.6	-
2D_24	1089.99	0.0	0.917	1.39	1.1	Subcritical
2D_25	1090.10	0.0	0.917	1.45	1.1	Critical
2D_26	1089.88	0.0	0.917	1.8	1.1	Supercritical

Table 3: Experimental parameters and calibration values of k for all the runs performed on smooth flat and upsloping beds.

Figure 2.13a-d shows the comparisons of numerical gravity current's profiles and the images acquired by the camera for the run 2D_4, performed on flat smooth bed with initial density of the gravity current $\rho_{01} \cong 1060$ Kg/m^3, at four different time steps after release, $t=8$ s (Figure 2.13a), $t=12$ s (Figure 2.13b), $t=18$ s (Figure 2.13c) and $t=30$ s (Figure 2.13d), respectively: yellow solid line represents the current's profile obtained taking into account the entrainment phenomenon, therefore considering two miscible fluids and using the calibration value of $k=0.6$; red dashed line show current's profile obtained neglecting the entrainment term in the numerical model, hence considering two immiscible fluids (i.e. $k=0$). As previously explained, the effect of mixing is to produce a mass flow from the lighter fluid to the heavier one, causing an increase of the height of the current's profile.

As a consequence, in Figure 2.13a-d a reduction of the height of the gravity current can be observed in the profiles obtained without taking into account the entrainment phenomenon.

Figure 2.14 shows the space-time evolution in dimensionless form of the same run (i.e. Run 2D_4) obtained by laboratory measurement, numerical simulation for miscible fluids (i.e. $k=0.6$) and immiscible fluids (i.e. $k=0$). This comparison shows that if mixing is not taken into account the numerical prediction is in agreement with experimental measurement only for the initial stage of gravity current's development. Such an initial stage could be identified with the first constant speed phase (i.e. slumping phase) during which the entrainment phenomenon is not involved enough in the flow dynamics. The numerical simulation obtained for miscible fluids with $k=0.6$ shows a good agreement with the measured front position.

The same kind of comparison are shown in Figure 2.15a-d and Figure 2.16 for the run 2D_21 performed on smooth upsloping bed with initial density of the gravity current $\rho_{01} \cong 1060$ Kg/m^3 and $\vartheta=1.14°$.

Figure 2.15a-d shows the comparisons of numerical gravity current's profiles and the images acquired by the camera, at four different time steps after release, $t=5$ s (Figure 2.15a), $t=10$ s (Figure 2.15b), $t=15$ s (Figure 2.15c) and $t=20$ s (Figure 2.15d), respectively. In this case the calibration value is $k=0.9$. As for the case of the gravity current performed on flat bed (i.e. Run 2D_4), the numerical simulation obtained neglecting the entrainment term provides a less high profile for the current which not agrees with the interface between the two fluids detectable from the images acquired by the camera. Figure 2.15a-d shows that the numerical run performed for miscible fluids shows a good agreement with laboratory measurements as can be observed also in Figure 2.16, that shows front position versus time for the run 2D_21 obtained by laboratory measurement, numerical simulation for miscible fluids (i.e. $k=0.9$) and immiscible fluids (i.e. $k=0$).

Figures 2.17a-d, 2.18a-d and 2.19a-d show the comparisons between numerical and experimental front position versus time in dimensionless form for the runs

performed on flat and upsloping smooth bed with initial density of the dense fluid $\rho_{01} \cong 1039$, 1060 and 1090 Kg/m^3, respectively . The numerical results are obtained for miscible fluids, using the calibration value for k chosen for each run. The comparison shows a good agreement between experimental front positions and numerical predictions.

In order to define the ability of the model in simulating gravity currents, an error E_{xf} was computed in the following way:

$$E_{xf} = Mean\left(\left|1 - \frac{x_{nf}^*}{x_{ef}^*}\right| \times 100\right)$$ (41)

Where x_{nf}^* and x_{ef}^* are the numerical and experimental dimensionless front position, respectively. Table 4 shows the value of E_{xf} for each run. The mean error E_{xf} reaches a maximum value of 4.7 % for the runs 2D_19 and 2D_25 and a minimum value of 1.0 % for the run 2D_4. Therefore the agreement between the results for the numerical and experimental front position is fairly good, being the error values reasonable for all the investigated experimental conditions.

Run	ρ_{01} [Kg/m^3]	ϑ [°]	E_{xf} [%]	Angle
2D_3	1039.54	0.00	2.5	-
2D_18	1038.59	0.90	2.0	Subcritical
2D_19	1038.59	1.11	4.7	Critical
2D_20	1039.10	1.39	2.9	Supercritical
2D_4	1059.56	0.00	1.0	-
2D_21	1059.72	1.14	2.3	Subcritical
2D_22	1059.75	1.39	3.3	Critical
2D_23	1059.72	1.52	1.9	Supercritical
2D_5	1089.99	0.00	2.1	-
2D_24	1089.99	1.39	3.8	Subcritical
2D_25	1090.10	1.45	4.7	Critical
2D_26	1089.88	1.80	3.6	Supercritical

Table 4: Experimental parameters and mean error E_{xf} computed for each run on the basis of Equation (41) for all the 2D released currents performed on smooth flat and upsloping beds.
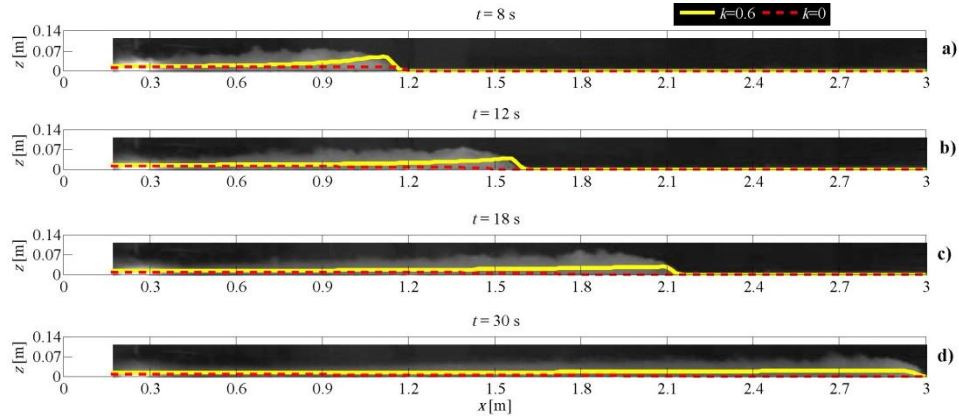
Figure 2.13a-d: Comparison of numerical gravity current's profiles for the run 2D_4 moving on flat and smooth bed and the images acquired by the camera at four different time steps: miscible fluid, k=0.6 (solid yellow line) and immiscible fluid, k=0 (red dashed line).
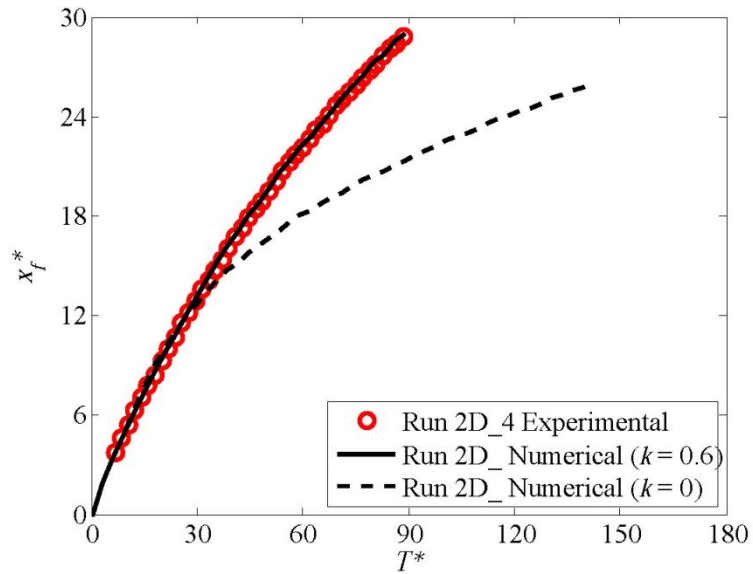
Figure 2.14: Front position versus time for the run 2D_4 moving on flat and smooth bed: measurements (red circles), numerical simulation with k=0.6 (black solid line) and numerical simulation with k=0.0 (black dashed line).
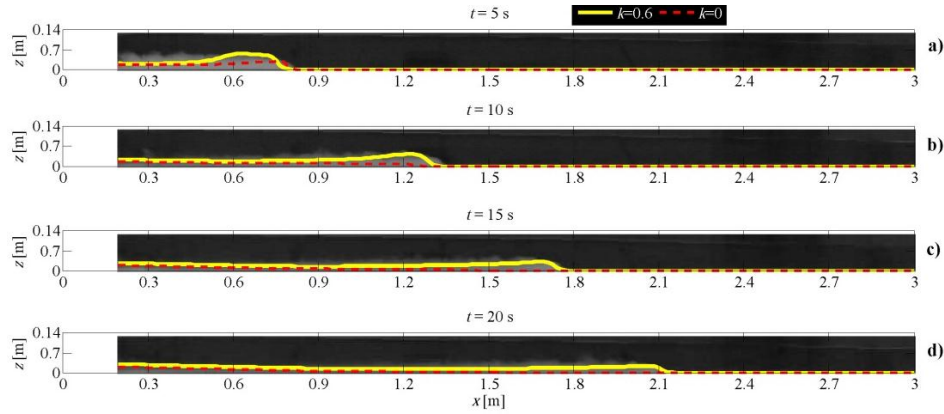
Figure 2.15a-d: Comparison of numerical gravity current's profiles for the run 2D_21 moving on smooth and upsloping bed and the images acquired by the camera at four different time steps: miscible fluid, k=0.9 (solid yellow line) and immiscible fluid, k=0 (red dotted line).
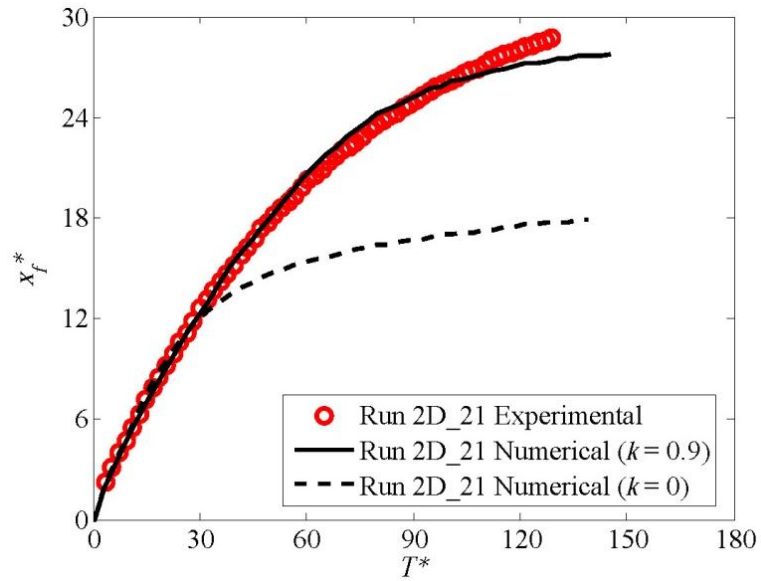
Figure 2.16: Front position versus time for the run 2D_21 moving on smooth and upsloping bed: measurements (red circles), numerical simulation with k=0.9 (black solid line) and numerical simulation with k=0.0 (black dotted line).
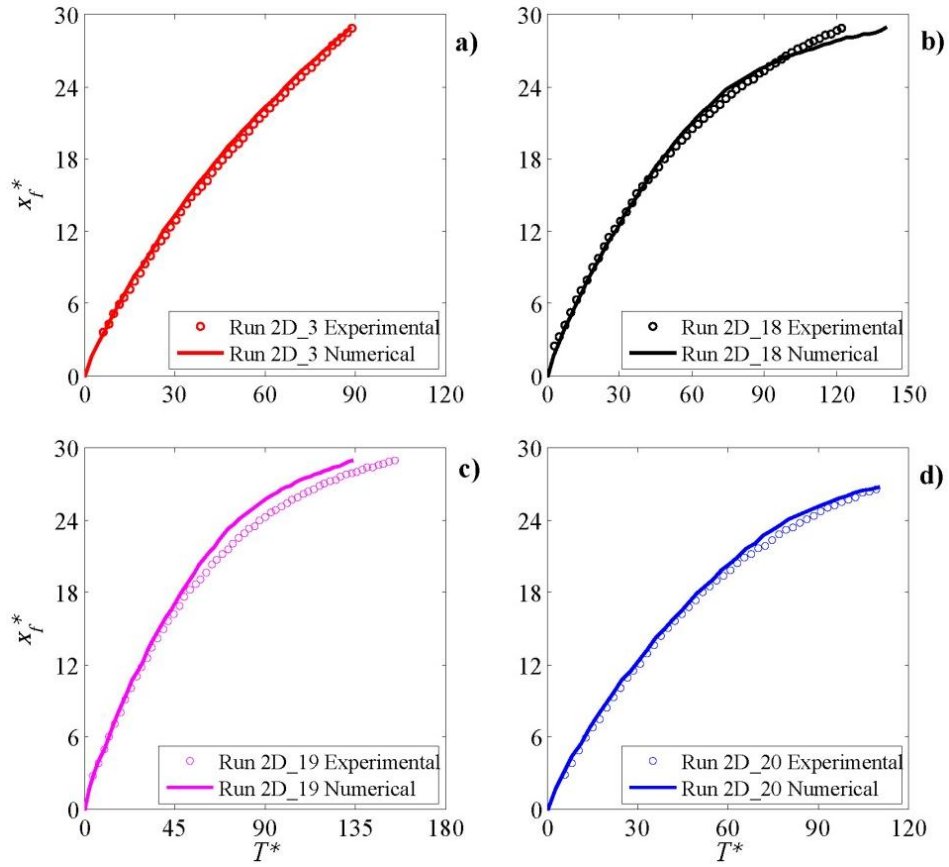
Figure 2.17a-d: Experimental and numerical front position versus time for all the runs performed with $\rho_{01} \cong 1039$ Kg/m^3 on flat and upsloping smooth beds; (a) Run 2D_3: ϑ=0.00°; (b) Run 2D_18: ϑ=0.90°; (c) Run 2D_19: ϑ=1.11°; (d) Run 2D_20: ϑ=1.39°.
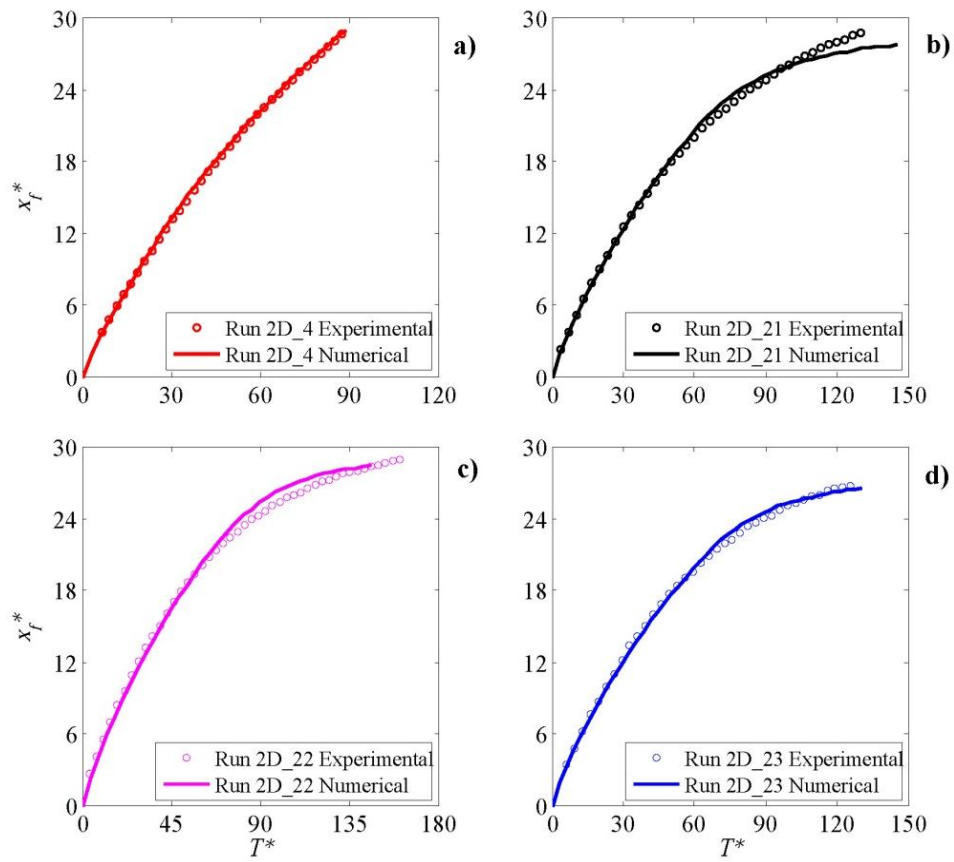
Figure 2.18a-d: Experimental and numerical front position versus time for all the runs performed with $\rho_{01} \cong 1060$ Kg/m^3 on flat and upsloping smooth beds; (a) Run 2D_4: ϑ=0.00°; (b) Run 2D_21: ϑ=1.14°; (c) Run 2D_22: ϑ=1.39°; (d) Run 2D_23: ϑ=1.52°.
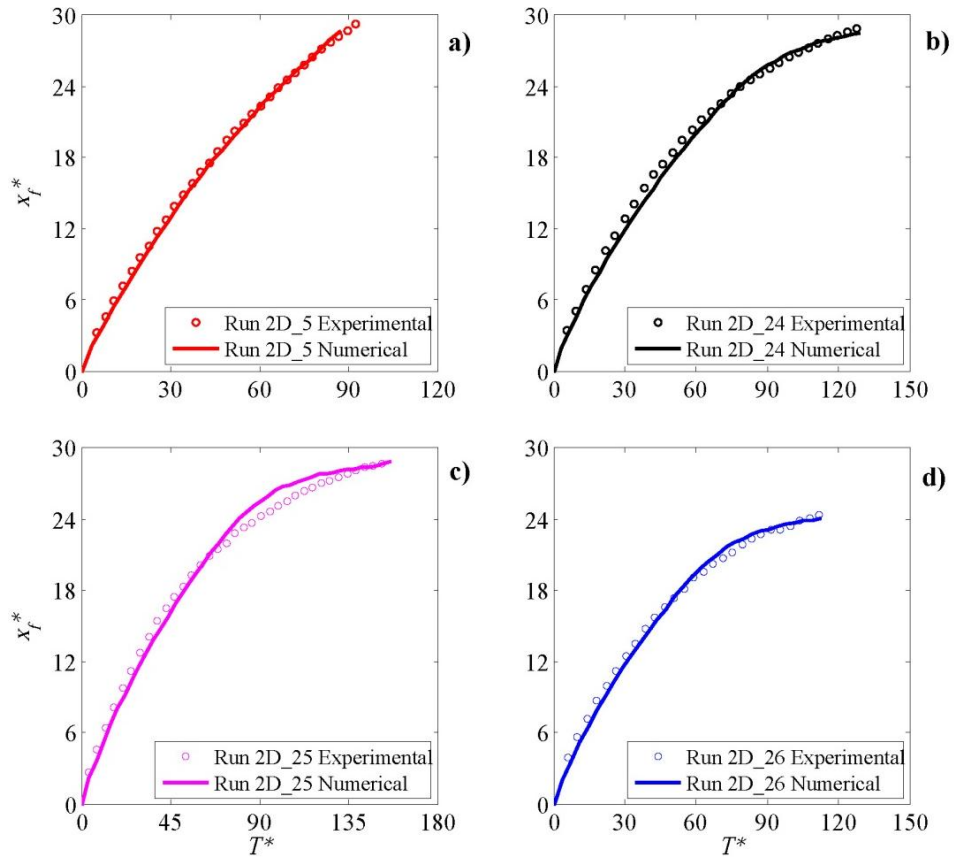
Figure 2.19a-d: Experimental and numerical front position versus time for all the runs performed with $\rho_{01} \cong 1090$ Kg/m^3 on flat and upsloping smooth beds; (a) Run 2D_5: ϑ=0.00°; (b) Run 2D_24: ϑ=1.39°; (c) Run 2D_25: ϑ=1.45°; (d) Run 2D_26: ϑ=1.80°.

2.3. Velocity measurements by PIV

Particle Image Velocimetry (PIV) is an optical technique for performing measurements of velocity fields in a wide range of flow conditions. As PIV technique does not use any probe that can disturb the flow, it can be considered as a non-intrusive technique. Moreover an important feature of PIV technique is that it can be used to obtain the spatial velocity distribution for a whole field simultaneously. The working principle of a PIV system is based on the determination of velocity vectors from the displacement of seeding particles and the time for the displacement.

A general PIV system requires four main components: an optical transparent tank filled with fluid seeded with tracer particles, a laser source producing a laser sheet, a camera acquiring images in the area of interest and a computer with suitable software to process the recorded images and calculate velocity information on the basis of the particles displacements.

The velocity of suspended particles is measured by capturing images of the whole field of analysis in which seeding particles are illuminated with a sheet of laser light. Figure 2.20 shows a sketch of fundamental components of a common PIV system.

Tracer particles should satisfy two main requirements: they should follow the streamlines of the flow, without influencing the fluid properties and they should be characterized by an high scattering efficiency. Assuming that the settling velocity under gravity is governed by Stokes drag, a way to evaluate the first requirements is to calculate the particles settling velocity by:

$$u_\infty = \frac{g d_p^2 (\rho_p - \rho_f)}{18\mu} \qquad (42)$$

In which d_p and ρ_p are the diameter and density of the reflective particle, μ and ρ_f are the dynamic viscosity and the density of the fluid. Particles are suitable if the settling velocity u_∞ is negligible compared to the flow velocity, therefore they are neutrally buoyant in the fluid.

Once the fluid is seeded with suitable particles a double pulsed laser is used to illuminate one plane of the flow. In order to find the displacement of groups of particles over a short time interval, two successive images, corresponding to two pulses of the laser that illuminate the field of view, are compared. The acquired images are divided into several sub-areas, commonly called interrogation areas. Each interrogation area is compared with the sub-area corresponding to the same location in the second image using a cross-correlation technique, in order to find the average motion of a small group of particles contained within the sub-area

(Adrian, 1991). This process is repeated for all the interrogation areas of the investigated domain, providing one displacement vector per spot. Since the time interval between the two laser pulses (i.e. two images) is known, from the averaged displacement of the particles it is possible to deduce their velocity. Applying this technique to all the couples of images, corresponding to the whole duration of the experiment, the complete velocity vector field is obtained.

In this work PIV technique was applied in order to measure the velocity field of gravity currents produced by lock exchange release. One of the main objectives of this stage of work was to verify the reliability of the back flow predicted for gravity currents moving on upsloping beds by the one-dimensional numerical model near the lock of the tank.

Two experiments were realized: a first preliminary run (PIV1) was carried out in order to test the PIV system for gravity current moving on flat and smooth bed and a second run (PIV2) was realized on smooth upsloping bed in order to compare experimental results with numerical predictions.

Regarding velocity measurements within the area near the lock of the tank (i.e. PIV2) it must be taken into account that during the first stage of development of the gravity current, there is a high density gradient between the two fluids, because the entrainment is not occurring yet in the flow dynamics. As the index of refraction changes with the local value of the density, a high density gradient can cause a blurred image in which individual particles cannot be distinguished (Alahyari & Longmire, 1994). In order to avoid this problem RIM (Refractive Index Matching) method was applied. This method consists in choosing defined concentrations of particular solutions which ensure throughout the flow a uniform refractive index.
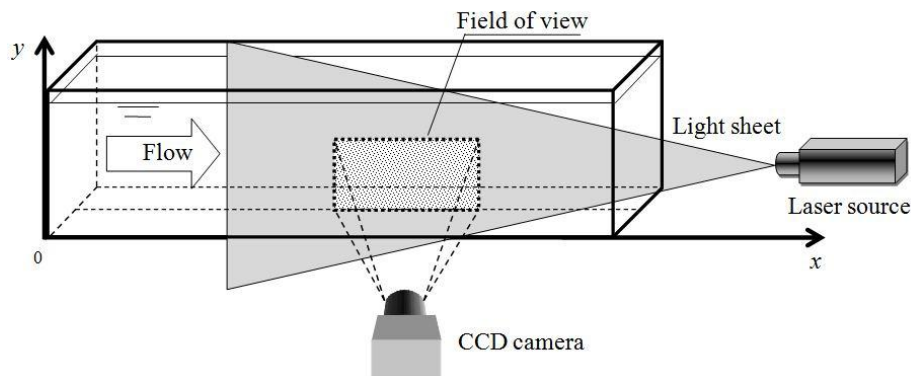
Figure 2.20: Sketch of a general PIV system showing the main components: tank with transparent wall filled with fluid seeded with tracer particles, laser source producing laser sheet, camera acquiring images in the area of interest.

2.2.1. Flat smooth bed

The initial condition of a typical lock exchange release experiment is set up using a Perspex tank in two-dimensional configuration (Figure 2.21). As widely described in previous sections one of the two portion of the tank (i.e. the lock) was filled with dense fluid and the other with lighter ambient fluid. In this case no dye was added to the dense solution, but both the dense and the ambient fluid were seeded with reflective particles.

In order to test the PIV System, a first lock exchange experiment (PIV1) was performed using a solution of sodium chloride (*NaCl*) and tap water as lock fluid and fresh water as surrounding fluid. For the run PIV1 the following experimental parameters were used: ρ_2=1000 Kg/m^3, ρ_{01}=1014.84 Kg/m^3, x_0=0.10 m and h_0=0.20 m.

A PIV system (Intelligent Laser Applications) with a double pulsed Nd:YAG Laser was used. The frequency between the couples of images was 3 Hz and the time between pulses was 30 ms. Both the dense fluid and the ambient fluid were seeded with polyamide particles with a mean diameter of 100 μm and a density of 1016 Kg/m^3. The laser source was positioned normal to the right end wall of the tank, so that the laser sheet was parallel to the sidewalls of the channel and directed along the tank's centerline. A CCD camera was located normal to the sidewall and acquired in a field of view 0.33 m long and 0.17 m high, positioned at *x*=2.13 m, as it is shown in Figure 2.21.
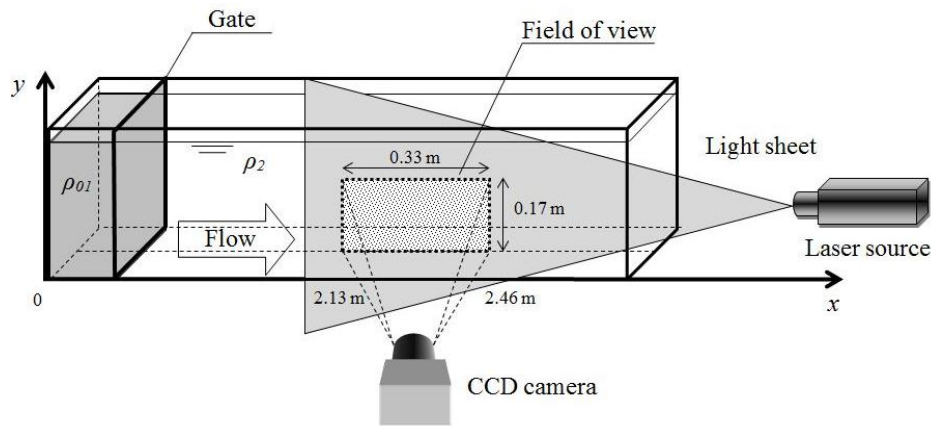
Figure 2.21: Sketch of the PIV system used for velocity measurements showing the field of view analyzed for the run PIV1.

In Figure 2.22a-c vector maps at three different time steps, with Δt=2.66 s, are shown. In order to identify the height of the gravity current for each position on the *x*-axis, the experiment was repeated with the same experimental parameters

realizing a colored gravity current and the threshold method was applied to detect the interface between the two layers. Figure 2.23a-b shows contour plots of the x-velocity component, u, and the vorticity ω of the gravity current for six different time steps. Vector maps and contour plots of u show that the ambient fluid flows upward and backward as the lower layer moves forward with higher velocity. In the region of velocity shear between the two fluids, interfacial instabilities take place, as can be seen from the eddies formed at the rear of the head of the current's front (Figure 2.22a-c). A head and a tail in the gravity current's shape can be distinguished in Figure 2.23a. A gradual decrease of u from the head to the tail of the gravity current can be observed. Figure 2.22a-c shows that the field of u within the tail is relatively uniform, although it results influenced by the eddies formed behind the head of the current. In agreement with the results of Zhu et al. (2006) the vorticity field (Figure 2.23b) shows an area of positive vorticity at the interface between the two fluids and a region of negative vorticity along the rigid bottom boundary. The strip of positive vorticity is due to the velocity shear between the two layers, while the region of negative vorticity results from the no-slip condition at the bottom boundary. The upper positive vorticity distributes in a wide region, mainly located at the rear of the gravity current, as can be observed in vorticity contour plots for t=33.62 s, t=36.28 s and t=38.94 s (Figure 2.23b). The negative vorticity is concentrated in a thinner strip near the bottom of the tank.

Figure 2.24a-c shows u versus x for three different heights y_1=3.4 cm, y_2=2.6 cm and y_3=1.4 cm at t=33.62 s. In Figure 2.24a-c the maximum value of u is observed at x=13.4 cm, x=14.5 cm and x=15.3 cm at the heights y_1, y_2 and y_3, respectively. By a comparison of Figure 2.24a-c with Figure 2.22a, which referred to the same time t, it can be seen that the maximum velocity doesn't occur in correspondence of the nose of the current, but at least 5 cm upstream, within the head of the gravity current. Vertical profiles of u measured at three different positions x_1=7.9 cm, x_2=13.4 cm and x_3=18.1 cm for t=33.62 s are shown in Figure 2.25a-c. While x_1 and x_2 are located in the core of the head of the gravity current, x_3 is positioned in a zone near the nose of the current. The maximum velocity at x_3 is 4.6 cm/s, which is smaller than the maximum values 7.1 cm/s and 7.1 cm/s measured in the gravity current head at x_1 and x_2, respectively.

Figure 2.26 show the comparison between x-velocity component measured by PIV and x-velocity component predicted by numerical simulation by 1D numerical model at t=36.28 s, where the head of the current is within the field of view. As the numerical model adopts shallow water approximation, in order to compare numerical and experimental results, velocity values measured by PIV were averaged along the y-direction. A good agreement is observed for velocity profiles. The numerical velocity values seem to be slightly lower and this behavior could be due to the fact that the numerical current is shallower at the nose of the current than the experimental one.

Valentina Lombardi
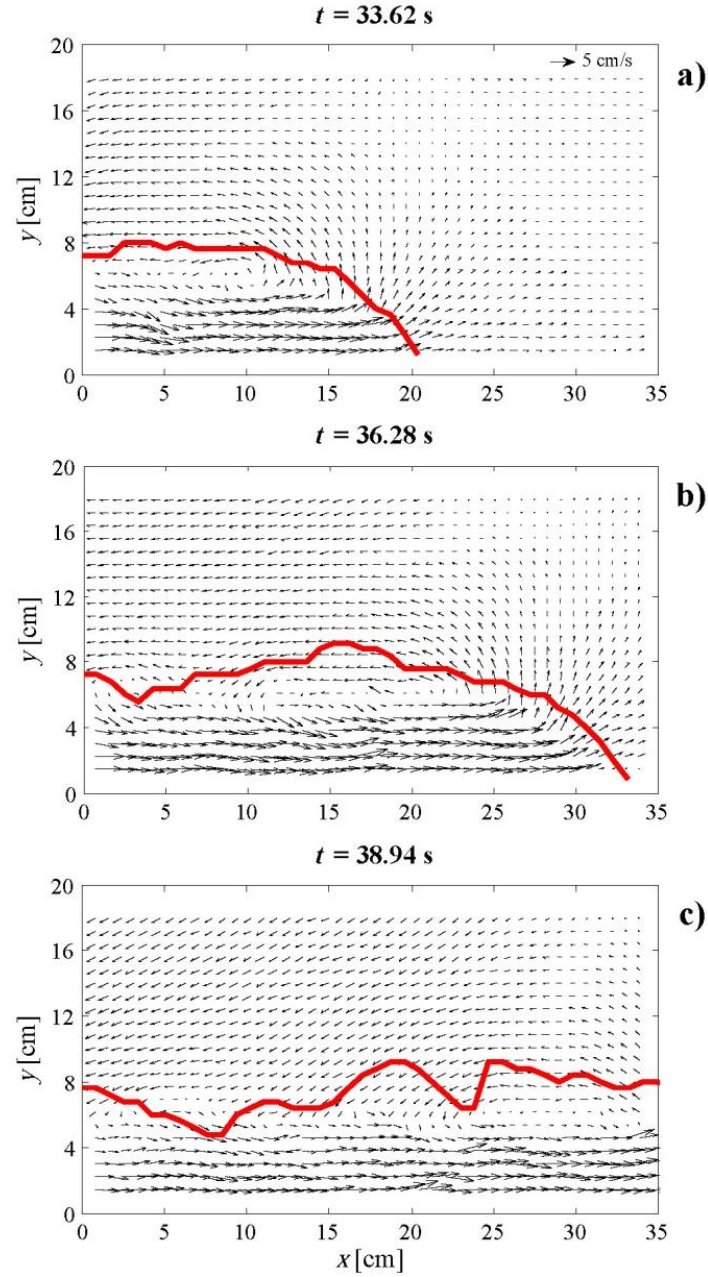
Figure 2.22a-c: Vector maps of the gravity currents at three different time steps. The red line is the interface between the two fluids, identified as the height of a colored release current performed with the same experimental parameters. Threshold method was applied to measure the profile of the current acquired by a CCD camera.
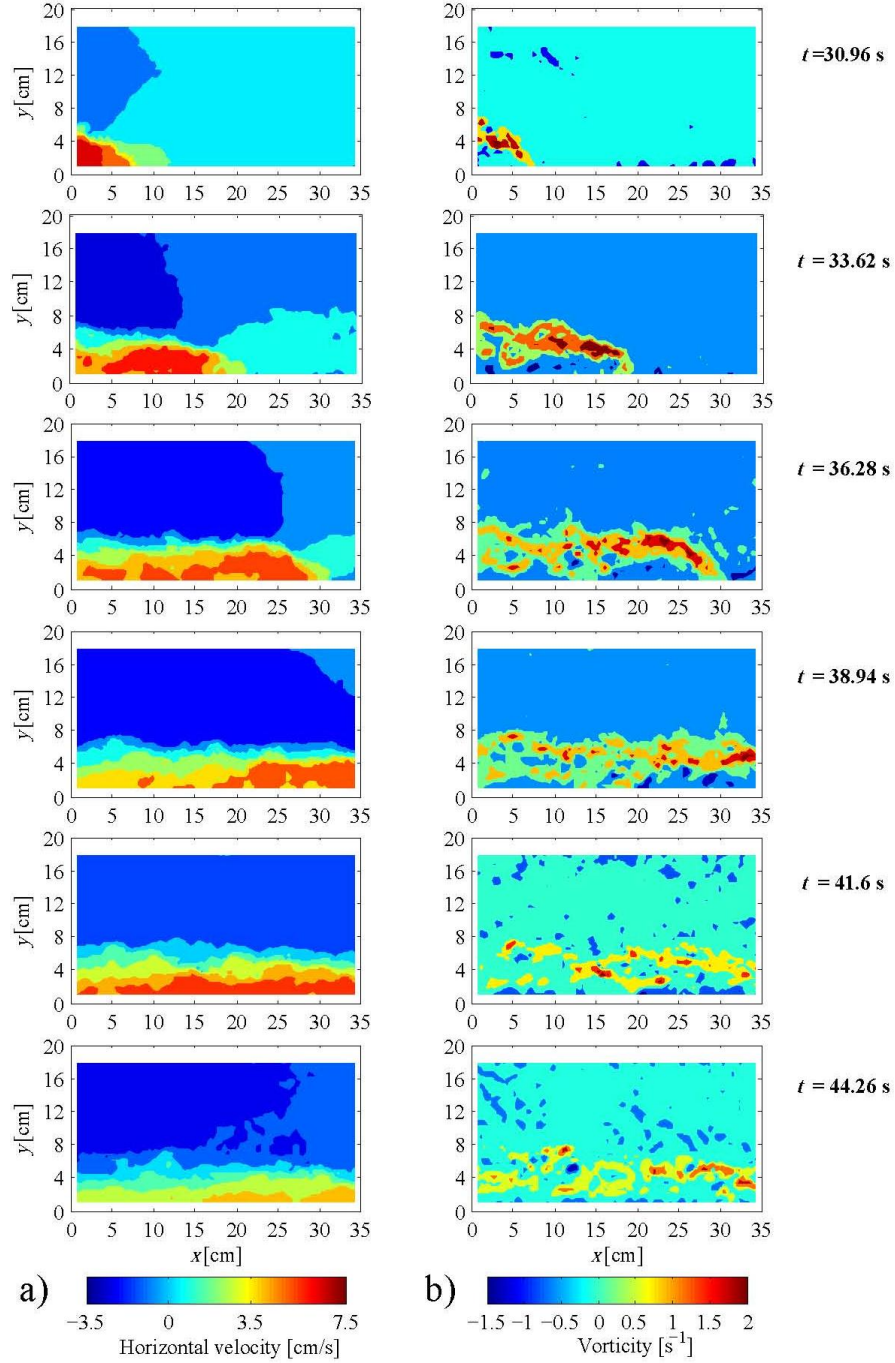
Figure 2.23a-b: Contour plots of the *x*-velocity component, *u*, (a) and vorticity *ω* (b) at six time steps for the run PIV1.
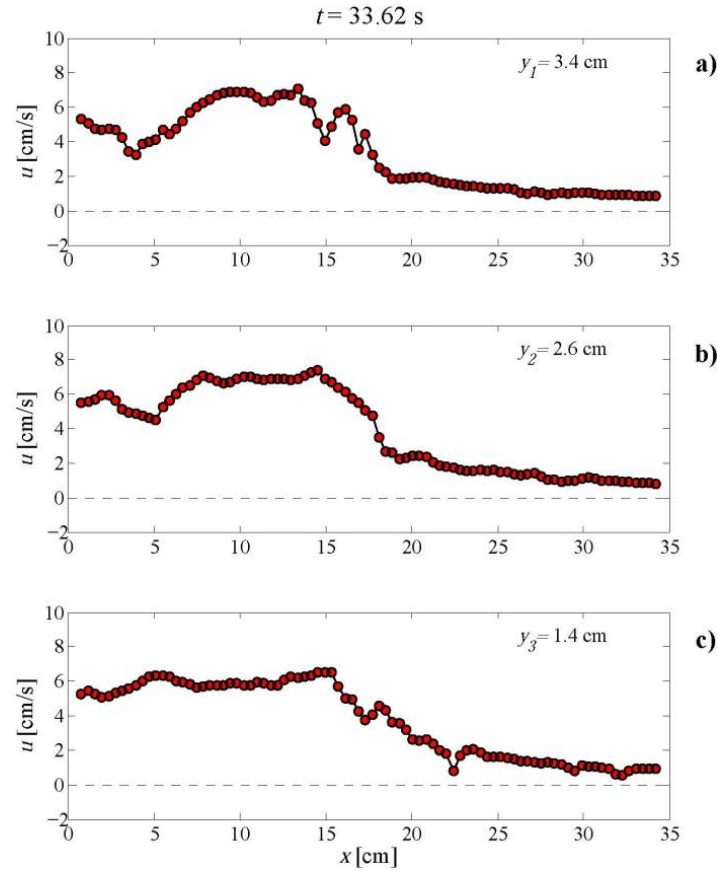
Figure 2.24a-c: *x*-velocity component measured along *x*-axis for three different heights y_1, y_2 and y_3 at t=33.62 s for the run PIV1. The dashed black line corresponds to the *x*-velocity component equals to zero.
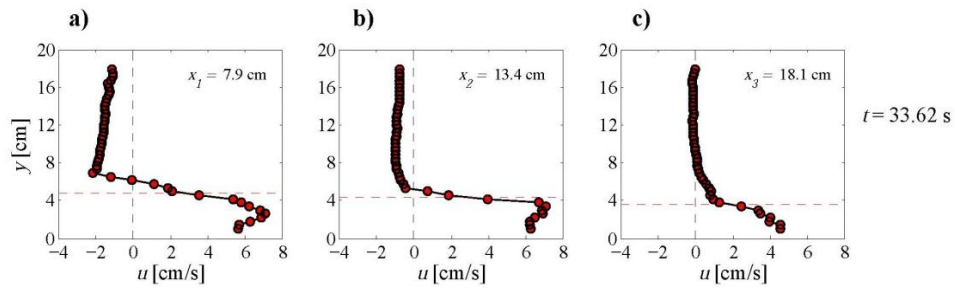
Figure 2.25a-c: Vertical profiles of the *x*-velocity component measured at three different positions x_1, x_2 and x_3 at for t=33.62 s for the run PIV1. The dashed black line corresponds to the *x*-velocity component equals to zero, while with the red dashed line is showed the height of the gravity current for each position on the *x*-axis.
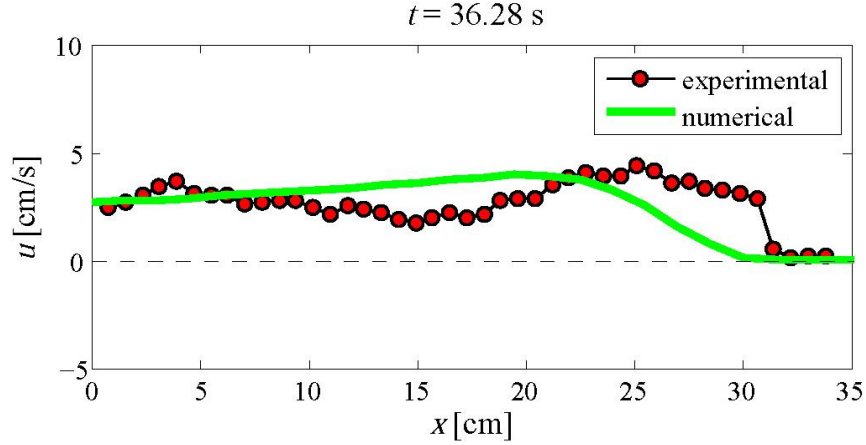
$$t = 36.28 \text{ s}$$

Figure 2.26: Comparison for the run PIV1 between x-velocity component measured by PIV (red circles) and x-velocity component predicted by numerical simulation by 1D numerical model (green line) at $t=36.28$ s. Velocity values measured by PIV are averaged along the y-axis. The dashed black line corresponds to u equal to zero.

2.2.2. Upsloping smooth bed

One of the aims of this stage of work was to verify the reliability of the back flow predicted for gravity currents moving on upsloping beds by the 1D numerical model near the lock of the tank. On this purpose a second run (PIV2) was performed on upsloping smooth bed in order to compare experimental data with numerical prediction. The run PIV2 was performed with the following parameters: $\rho_2=1011$ Kg/m^3; $\rho_1=1038$ Kg/m^3; $x_0=0.10$ m; $h_0=0.25$ m; $\vartheta=1.36°$.

In order to avoid problems associated with the variations in refractive index with the local value of density, for the run PIV2 the index matching strategy was applied. Following Alahyari & Longmire (1994) a solution of glycerol and water as the less dense fluid and an aqueous solution of potassium dihydrogen phosphate (KH$_2$PO$_4$) as the heavier one were used. Such concentrations of these fluids provide 3% of density difference and a uniform refractive index within the fluids.

For the run PIV2 the PIV system and PIV settings (i.e. frequency and time between pulses) described for the run PIV1 were used. Also in this case both the dense fluid and the ambient fluid were seeded with polyamide particles and the laser source was placed in the same position seen for the run PIV1. The CCD camera was located normal to the sidewall, in order to acquire in a field of view 0.52 m long and 0.21 m high, starting at $x=0.76$ m from the left end wall of the tank, as it is shown in Figure 2.27.

Figure 2.28a-c shows vector maps at three different time steps for the run PIV2. As for the run PIV1, in order to identify the interface between the two layers, the experiment was repeated with the same experimental parameters realizing a colored gravity current and applying the threshold method to height of the current.
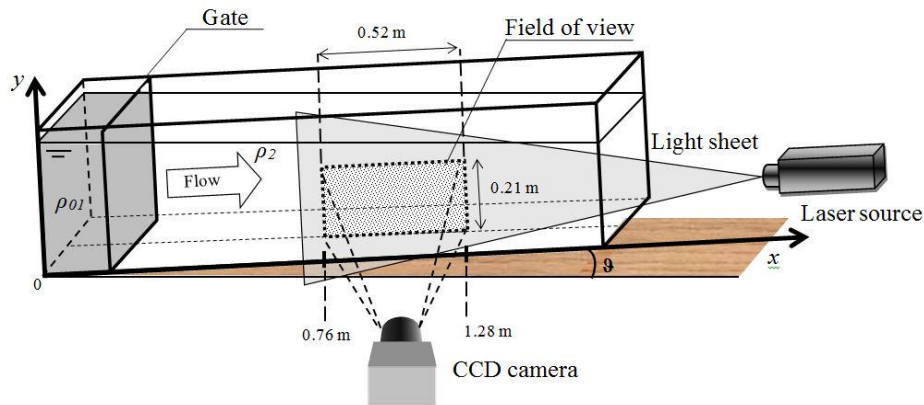
Figure 2.27: Sketch of the PIV system used for velocity measurements showing the field of view analyzed with the run PIV2.

Figure 2.28a and figure 2.28b refer to two time steps for which the current's front is still in the field of view, therefore they shows the velocity field of the head of the current. Figure 2.28c refers to the vector map of the tail of the current for an instant in which the current's front overtook the right boundary of the analysis domain, although it did not reach the right end wall of the tank. Figure 2.29a-b shows contour plots of horizontal velocity component and vorticity for six different time steps, with Δt=5.33 s. Figure 2.28a-c and Figure 2.29a-b show the same features observed for the run performed on flat and smooth bed (i.e. PIV1). Dense fluid flows in the positive direction of x-axis, while the surrounding fluid flows in the opposite direction with lower velocity. Contour plots of vorticity field in Figure 2.29b show a strip of negative vorticity near the bottom of the tank and an area of positive vorticity at the interface between the two fluids, although the vorticity gradient is less pronounced in respect to the vorticity field of the run PIV1. In Figure 2.28c near the bed of the tank a strip in which the flow direction is reversed to the gravity current's direction can be observed. Figure 2.30 and Figure 2.31a-b show the velocity vector map, the contour plot of x-velocity component and contour plot of vorticity respectively, referred to a detailed area of the field of view, 20 cm long and 14 cm high. A back flow can be observed in the lower part of the analysis domain near the bed of the tank.
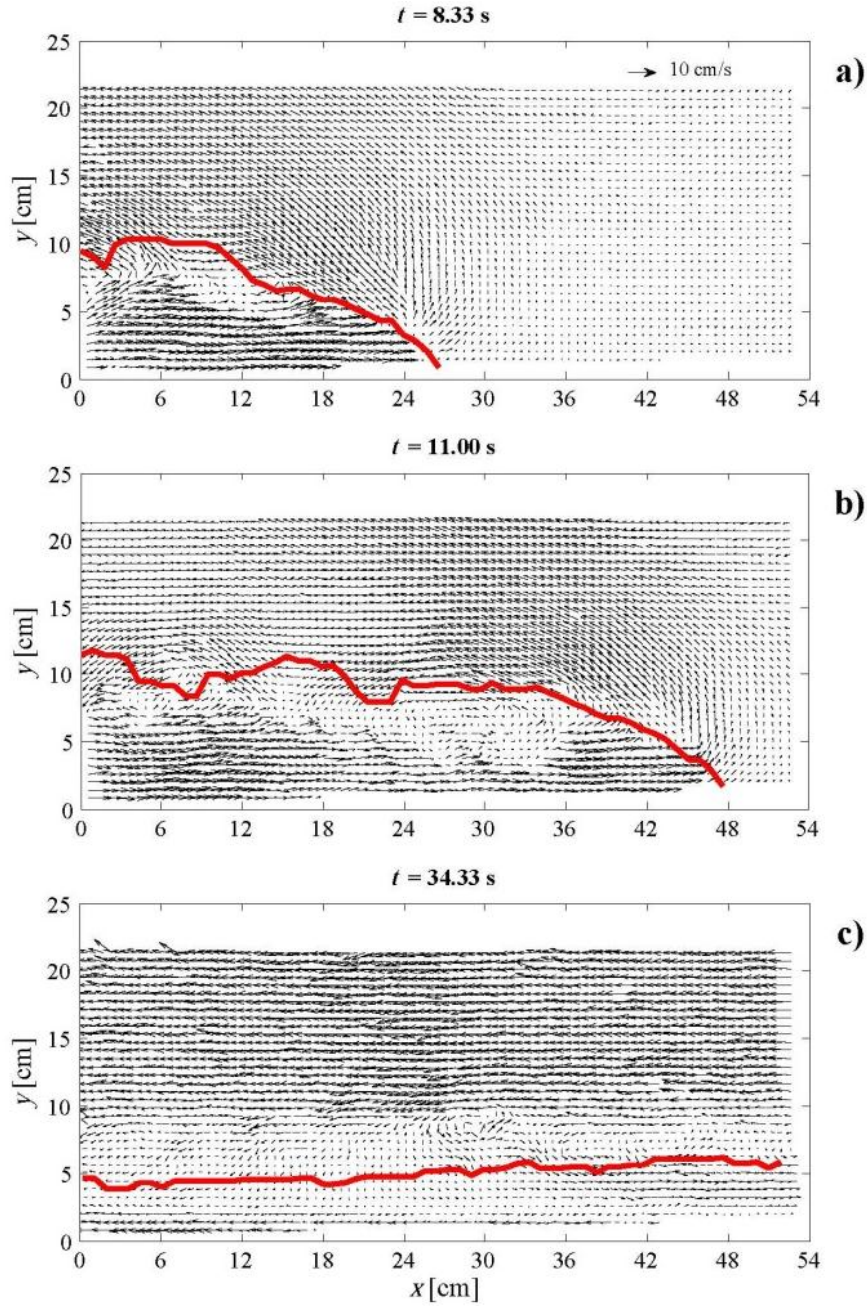
Figure 2.28a-c: Vector maps of the gravity currents at three different time steps. The red line is the interface between the two fluids, identified as the height of a colored release current performed with the same experimental parameters. Threshold method was applied to measure the profile of the current acquired by a CCD camera.

Valentina Lombardi
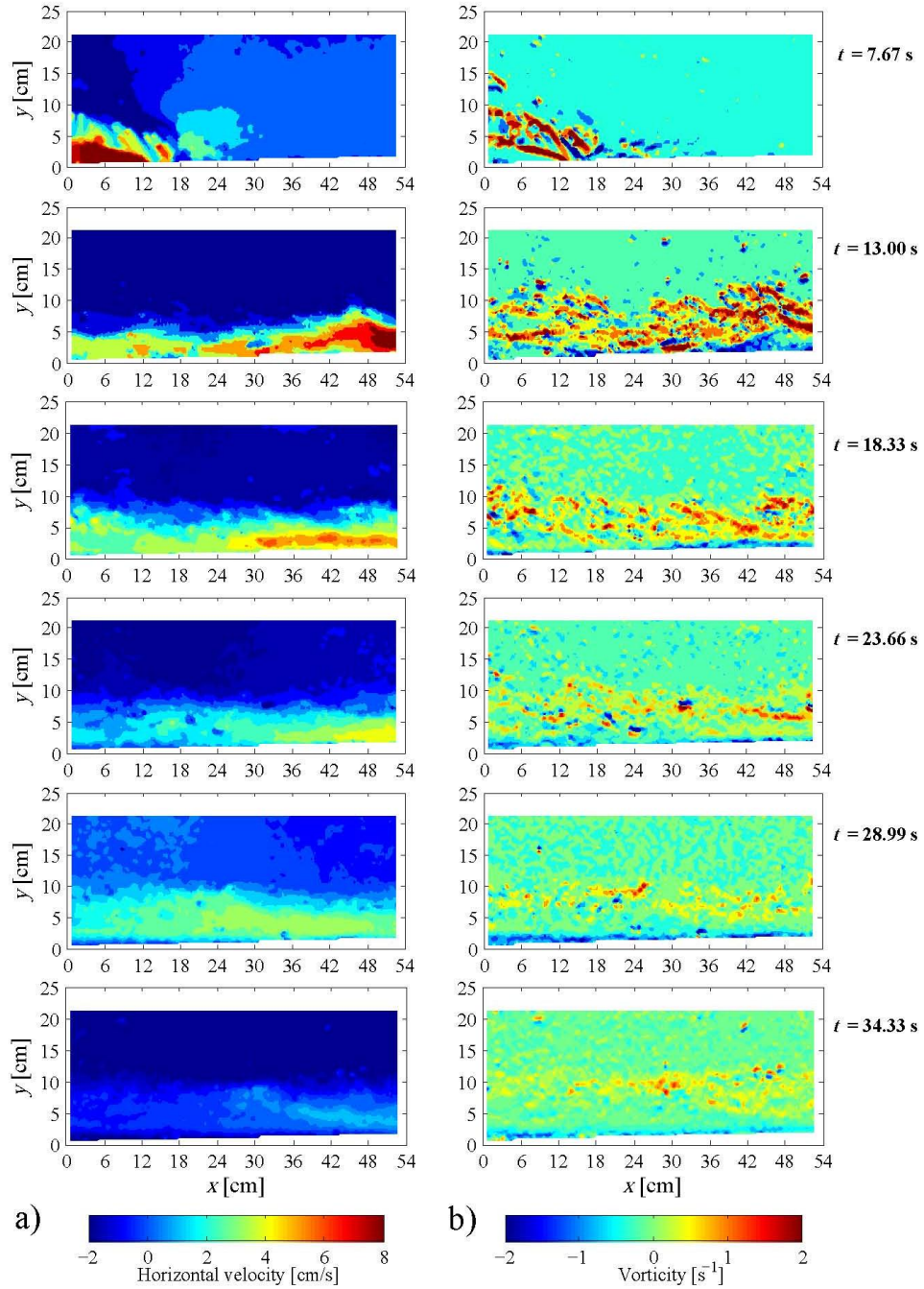
Figure 2.29a-b: Contour plots of the *x*-velocity component, *u*, (a) and vorticity *ω* (b) at six time steps for the run PIV2.
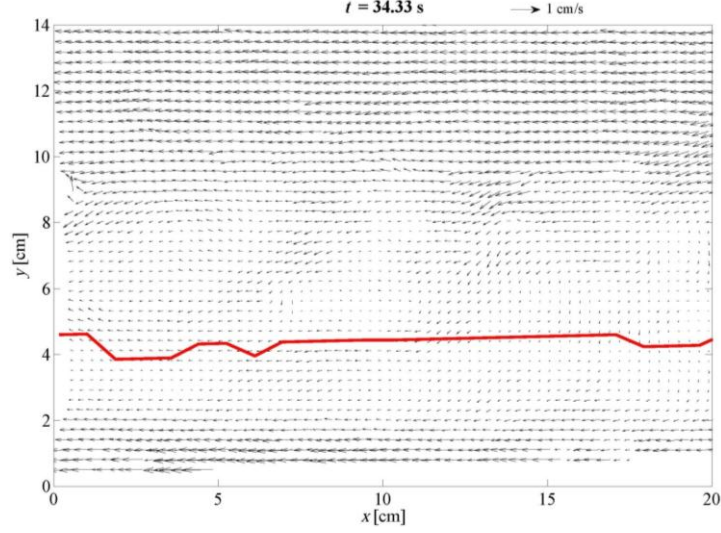
Figure 2.30: Vector maps of the gravity currents at *t*=34.33 s. Velocity field is shown for a detailed area of the field of view, 20 cm long and 14 cm high. The red line is the interface between the two fluids.

Figure 2.32a-c shows *u* versus *x* for three different heights y_1=3.8 cm, y_2=2.6 cm and y_3=1.7 cm for a defined time step. Figure 2.32a-c refers to the instant *t*=34.33 s at which the tail of the gravity current is observable in the field of view. Vertical profiles of *u* measured at three different positions x_1=6.9 cm, x_2=25.0 cm and x_3=42.2 cm for *t*=34.33 s are shown in Figure 2.33a-c. As can be seen from Figure 2.32a-c and Figure 2.33a-c negative values of *u* are mainly located in the region close the right left boundary of the analysis domain near the bed of the tank.

Figure 2.34 and Figure 2.35 show the comparison between *x*-velocity component measured by PIV and *x*-velocity component predicted by numerical simulation by 1D numerical model at *t*=8.33 s and *t*=34.33 s, respectively. As for run PIV1, in order to compare numerical and experimental results, velocity values measured by PIV were averaged along the *y*-direction. Figure 2.34 shows velocity profiles referred to the head of the current while Figure 2.35 is related to the tail of the current. A decrease of the mean horizontal velocity, both experimental and numerical, can be observed within the tail of the current (Figure 2.35), compared to the head of the current (Figure 2.34). Moreover a backflow (i.e. negative values of mean horizontal velocity) can be noticed observing both numerical and measured values. However, as the backflow is experimentally detected only in the area nearest to the lock of the tank (i.e. near the right boundary of the analysis domain), while the numerical model predicts negative mean horizontal values along the whole field of view, additional

laboratory experiments and PIV measurements should be performed in order to verify the real extent of the backflow predicted by numerical simulations. In Figure 2.34 an overestimation of the *x*-velocity component can be observed in the numerical profile. Such a discrepancy could be justified by taking into account that, while for the numerical model the simulation starts with the instantaneous contact between the two fluids, as the gate would suddenly disappear, for laboratory experiments the removal of the gate is a manual operation. This leads to a non-synchronous dynamics between numerical and experimental current whose delay can be taken into account in comparing results. However the physics consequences of the manual removal of the gate seems to influence in such a way the current's dynamics, mainly in the first stage of development of the current, which is analyzed by run PIV2.
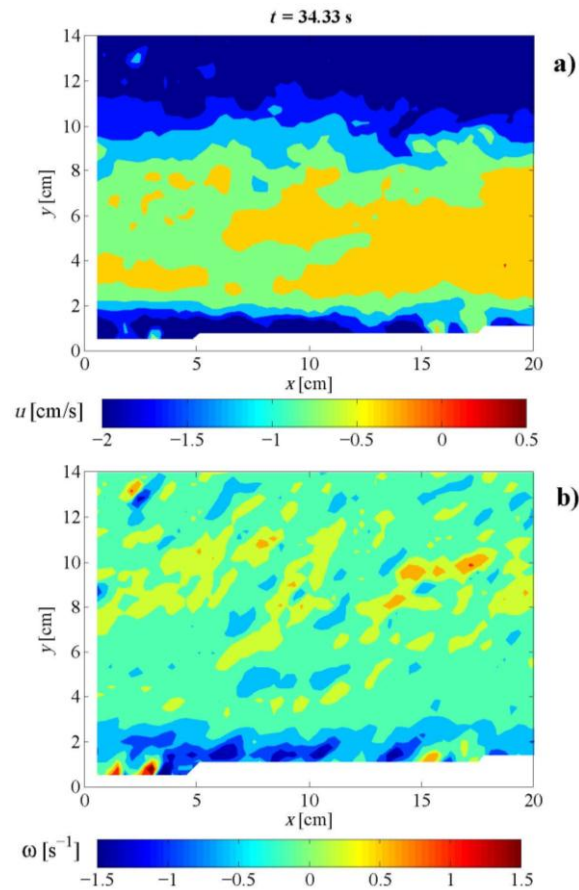
Figure 2.31a-b: Contour plots of the *x*-velocity component, *u*, (a) and vorticity *ω* (b) of the gravity currents at *t*=34.33 s for a detailed area of the field of view, 20 cm long and 14 cm high.
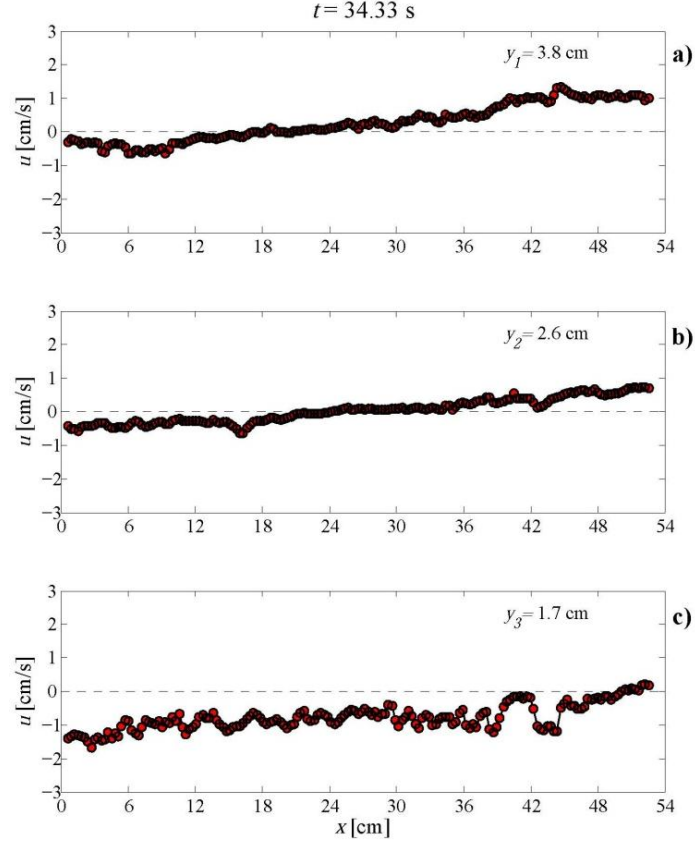
Figure 2.32a-c: *x*-velocity component measured along *x*-axis for three different heights y_1, y_2 and y_3 at t=34.33 s for the run PIV2. The dashed black line corresponds to the *x*-velocity component equals to zero.
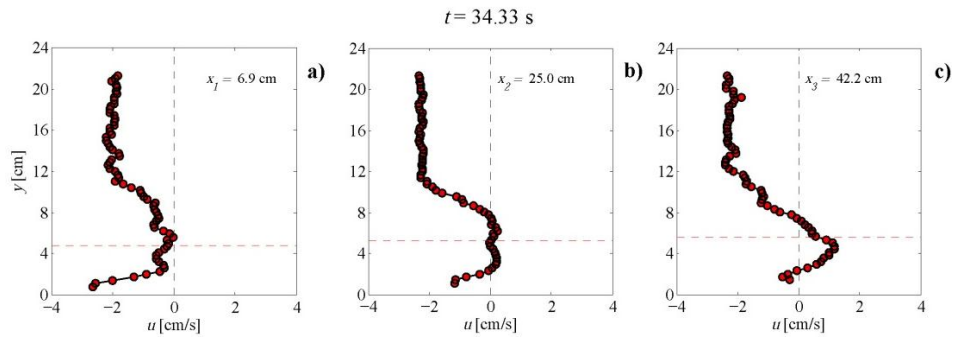
Figure 2.33a-c: Vertical profiles of the *x*-velocity component measured at three different positions x_1, x_2 and x_3 at for t=34.33 s for the run PIV2. The dashed black line corresponds to the *x*-velocity component equals to zero, while with the red dashed line is showed the height of the gravity current for each position on the *x*-axis.

Valentina Lombardi
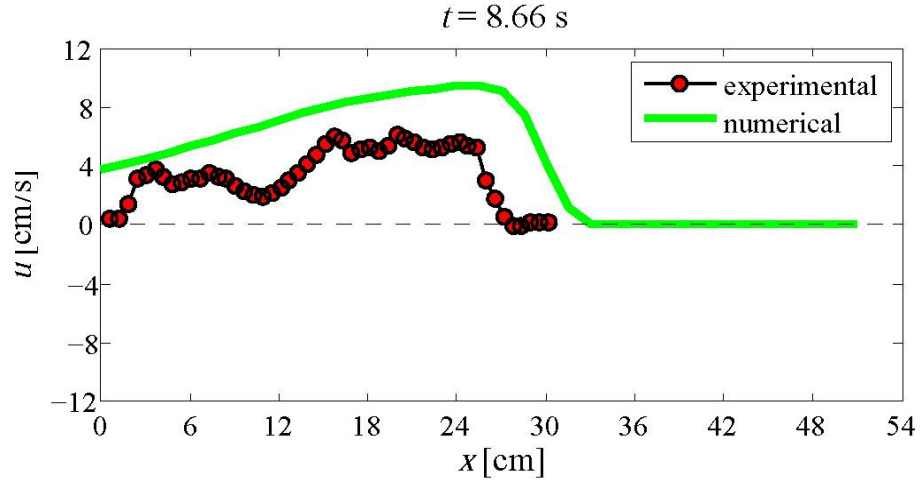
$t = 8.66$ s

Figure 2.34: Comparison for the run PIV2 between *x*-velocity component measured by PIV (red circles) and *x*-velocity component predicted by numerical simulation by 1D numerical model (green line) at *t*=8.66 s. Velocity values measured by PIV are averaged along the y-axis. The dashed line corresponds to *u* equal to zero.
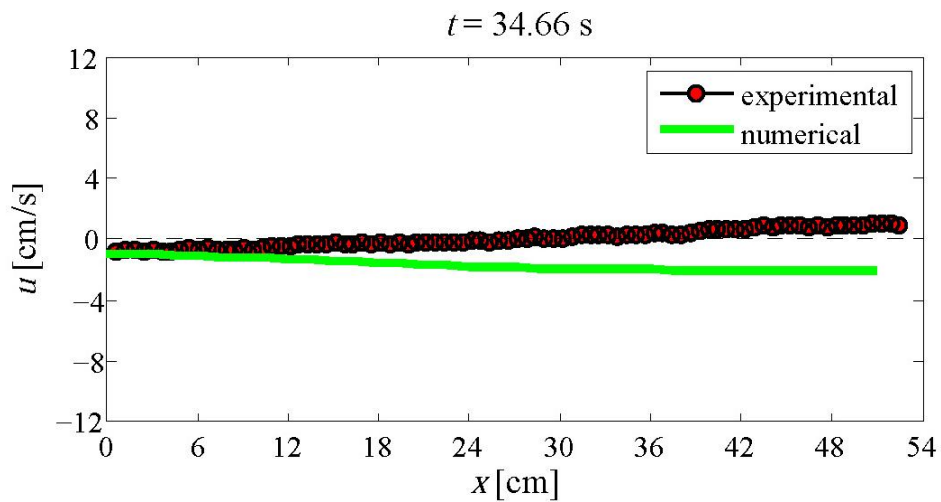
$t = 34.66$ s

Figure 2.35: Comparison between *x*-velocity component measured by PIV (red circles) and *x*-velocity component predicted by numerical simulation by 1D numerical model (green line) at *t*=34.66 s. Velocity values measured by PIV are averaged along the y-axis. The dashed line corresponds to *u* equal to zero.

3. 3D gravity currents

3.1. Laboratory experiments

3.1.1. Experimental set-up

Three-dimensional gravity currents were realized in the Hydraulics Laboratory of University of Rome "Roma Tre" using a rectangular Perspex tank, 2.35 m long, 1.35 m wide and 0.3 m deep. A sketch and a picture of the channel are shown in Figure 3.1a-c.

The channel was divided into two reservoirs of equal size by a rigid wall containing at the center a removable gate of length d. One part of the tank was filled with colored salty water with density ρ_{01} (i.e. lock fluid), while the other part was filled with clear tap water with lower density ρ_2 (i.e. ambient fluid). As the experimental configuration used in this work is the full-depth release experiment, both reservoirs have the same height h_0 and the ratio ϕ (i.e. fractional depth) of the initial gravity current height h_0 to the total height H, is such that $\phi=1$, as for 2D lock exchange experiments. Once the gate is manually opened, the two fluids with different densities come in contact and a non-equilibrium condition occurs. Indeed the heavier fluid collapses under the lighter one, originating the gravity current. For three-dimensional experiments the same CCD camera used for the two-dimensional currents was placed on the top of the tank and focused on the experimental domain, in order to acquire the current's development on the x-y plane.

The same image analysis technique, based on a threshold method, used for the two-dimensional tests was applied to detect the current shape for each time step. After choosing the grey level corresponding to the interface between the two fluids a program written in MatLab language travelled through the elements of the matrix (i.e. the image) until it met the threshold value (i.e. the interface between the two fluids) and recorded the coordinates of this pixel as a point of the interface between the two fluids. A rule was positioned along both the x and y axis (Figure 3.1a) in order to obtain the conversion factor pixel/cm. Figure 3.2a-d shows measured profiles of the experimental gravity current for the run 3D_1 overlapped to the images corresponding to four different time steps. In Figure 3.2a-d the typical mushroom shape of a three-dimensional gravity current detectable from a plan view can be observed. Such a form is recognized in each experimental condition investigated in this work. As pointed out for 2D experiments, the estimation of front position x_f is determined with an error equal to 0.2 cm, while the error for density measurements is 0.2%.

Valentina Lombardi
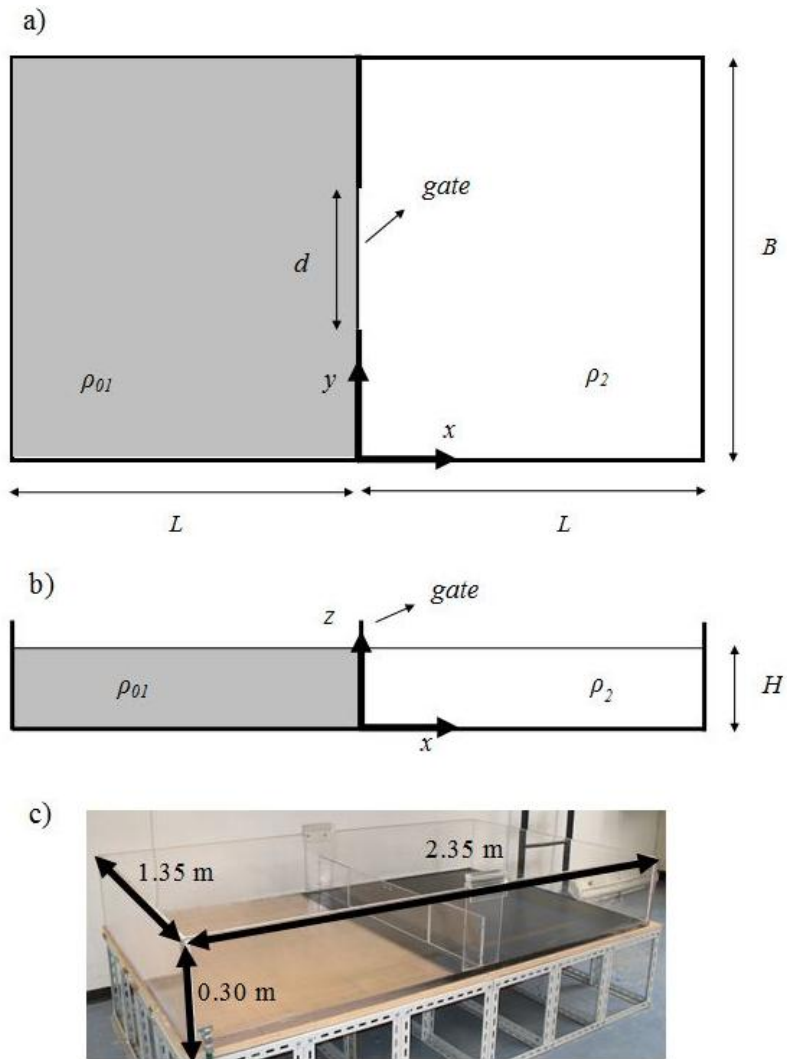
Figure 3.1a-c: Experimental apparatus used to perform the 3D lock-exchange experiments: (a) sketch of the top view; (b) sketch of the side view; (c) picture of the tank.
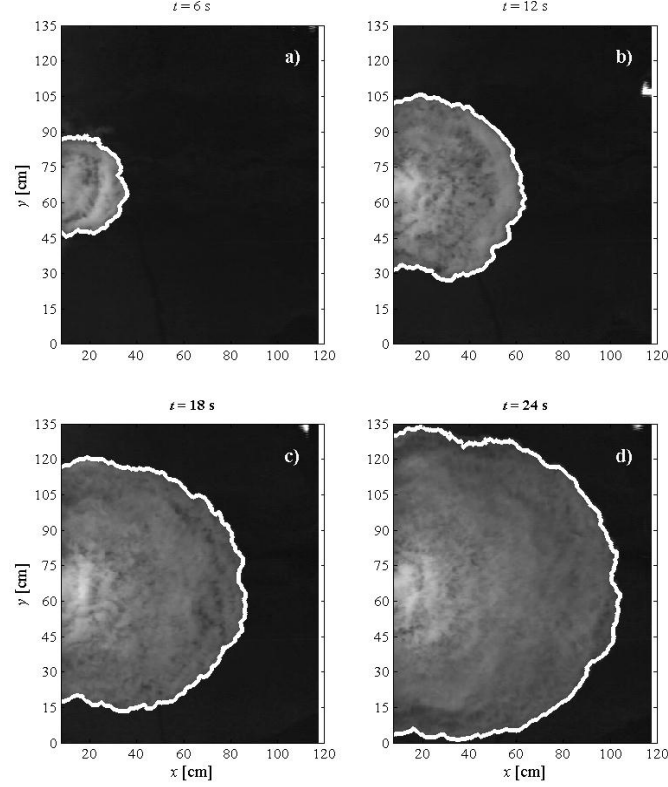
Figure 3.2a-d: Evolution on the *x-y* plane of the run 3D_1: measured profiles overlapped to the images corresponding to 6 s (a), 12 s (b), 18 s (c) and 24 s (d) after the release of the lock fluid.

3.1.2. Experimental parameters

Eighteen experiments were carried out keeping constant the initial density of the ambient fluid ρ_2=1000 Kg/m^3 and testing two different values of the initial density of the lock fluid $\rho_{01}\cong$1010 and 1030 Kg/m^3 corresponding to different values of the dimensionless ratio $r=\rho_2/\rho_{01}$, three initial height of the two fluids h_0=0.05, 0.10, 0.15 m corresponding to three values of the dimensionless parameter $H^*=h/L$ (i.e. H^*=0.128, 0.085, 0.042) and three values of the length of the sliding gate d=0.135, 0.35, 0.70 m, corresponding to three values of the dimensionless ratio $\delta=d/B$ (i.e. δ=0.100, 0.259, 0.518). Table 5 shows experimental parameters in dimensional and dimensionless form used for the performed 3D lock releases

Valentina Lombardi

Run	ρ_{01} [Kg/m^3]	h_0 [m]	d [m]	r =ρ_2/ρ_{01}	H* =h/L	δ =d/B
3D_1	1008	0.15	0.135	0.992	0.128	0.100
3D_2	1010	0.15	0.350	0.990	0.128	0.259
3D_3	1013	0.15	0.670	0.987	0.128	0.496
3D_4	1011	0.10	0.135	0.989	0.085	0.100
3D_5	1010	0.10	0.350	0.990	0.085	0.259
3D_6	1011	0.10	0.670	0.989	0.085	0.496
3D_7	1009	0.05	0.135	0.991	0.042	0.100
3D_8	1008	0.05	0.350	0.992	0.042	0.259
3D_9	1008	0.05	0.670	0.992	0.042	0.496
3D_10	1027	0.15	0.135	0.974	0.128	0.100
3D_11	1024	0.15	0.350	0.977	0.128	0.259
3D_12	1027	0.15	0.670	0.974	0.128	0.496
3D_13	1032	0.10	0.135	0.969	0.085	0.100
3D_14	1029	0.10	0.350	0.972	0.085	0.259
3D_15	1032	0.10	0.670	0.969	0.085	0.496
3D_16	1027	0.05	0.135	0.974	0.042	0.100
3D_17	1027	0.05	0.350	0.974	0.042	0.259
3D_18	1027	0.05	0.670	0.974	0.042	0.496

Table 5: Experimental parameters used to perform 3D gravity currents.

3.1.3. Experimental results

In this study three-dimensional gravity current's evolution was investigated by acquiring a movie of the experiment from the top of the tank, in order to measure the current's profile on the *x-y* plane (Figure 3.2 a-d). In this section time histories of front position for all the performed runs are shown. The instantaneous position of the experimental current's front along the *x*-axis direction is detected along the centerline of the tank from the instantaneous profile of the gravity current measured by image analysis as explained in details in section 3.1.1. All the laboratory measurements starts few seconds after the release of the dense fluid, as it was difficult to identify the current's shape as soon as the gate was removed.

Dimensionless front position x_f^* is defined as:

$$x_f^* = \frac{x_f}{L} \tag{43}$$

Dimensionless time T^* is scaled on the basis of t_0:

$$T^* = \frac{t}{t_0}; \quad t_0 = \frac{L}{\sqrt{g_0'H}} \tag{44}$$

Figure 3.3a-f and Figure 3.4a-f show experimental front position versus time for all the experiments performed with $\rho_{01} \cong 1010$ Kg/m^3 and 1030 Kg/m^3, respectively. Figure 3.3a-b-c and Figure 3.4a-b-c are in dimensional form, while Figure 3.3d-e-f and Figure 3.4d-e-f are in dimensionless form. Each plot shows a comparison between the runs performed with the same value of h_0 and different values of d. During the same time the run performed with the lower value of d (i.e. d=0.135 cm) covers a smaller distance than those realized with higher values of d (i.e. d=0.35 and 0.67 cm).

Figure 3.5a-f, 3.6a-f, 3.7a-f are referred to all the runs performed with initial height of the gravity current h_0=0.15, 0.10, 0.05 cm, respectively. Each plot is referred to the runs obtained with the same values of d, so that the only experimental parameter varying in each plot is ρ_{01}, whose effect can be highlight by this comparison. In particular the observed trend is that the speed of the current increases as the initial density of the heavier fluid increases. The same general trend has been observed in 2D gravity currents, fully described in section 2.1.3.1. For a constant time the gravity currents performed with $\rho_{01} \cong 1030$ Kg/m^3 covers a longer distance than those realized with $\rho_{01} \cong 1010$ Kg/m^3.

Figure 3.8a-f and Figure 3.9a-f show the time histories of front position for all the runs performed with $\rho_{01} \cong 1010$ Kg/m^3 and 1030 Kg/m^3, respectively. Each plot is a comparison between experiments realized with the same value of d and different values of h_0, in order to point out the effect of h_0 on the current's dynamics. The observed trend is that as the initial height of the current increases also the current's speed increases.
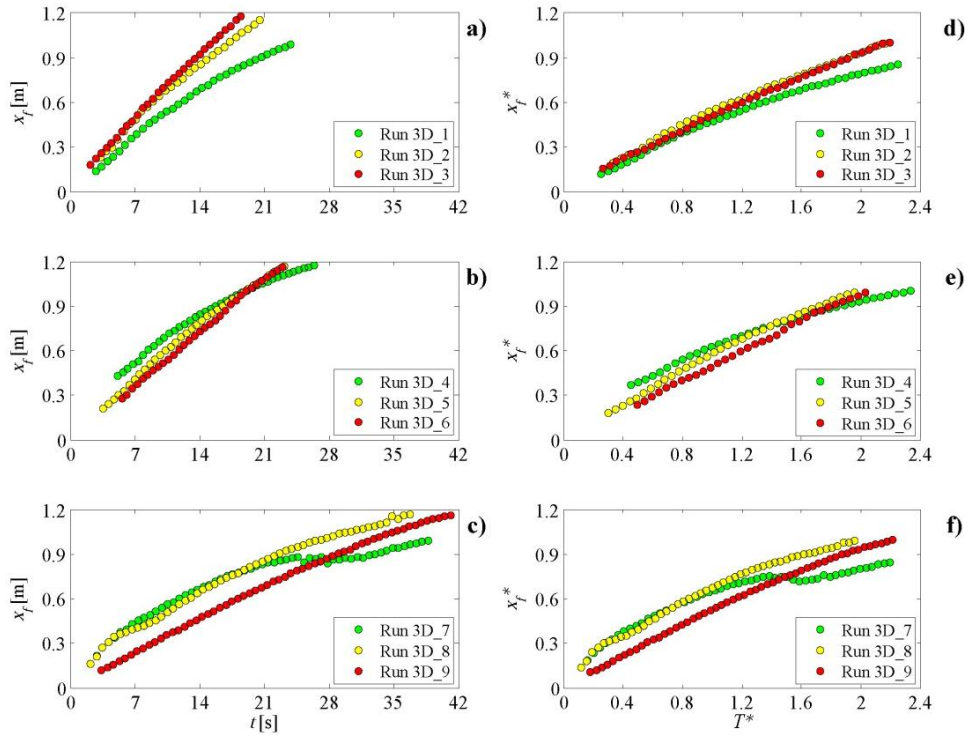
Figure 3.3a-f: Dimensional and dimensionless plot of front positions versus time for the runs with $\rho_{01} \cong 1010$ Kg/m³; (a-d) Runs 3D_1-3D_2-3D_3: h_0=0.15 m, d=0.135, 0.35, 0.67 m; (b-e) Runs 3D_4-3D_5-3D_6: h_0=0.10 m, d=0.135, 0.35, 0.67 m; (c-f) Runs 3D_7-3D_8-3D_9: h_0=0.05 m, d = 0.135, 0.35, 0.67 m.
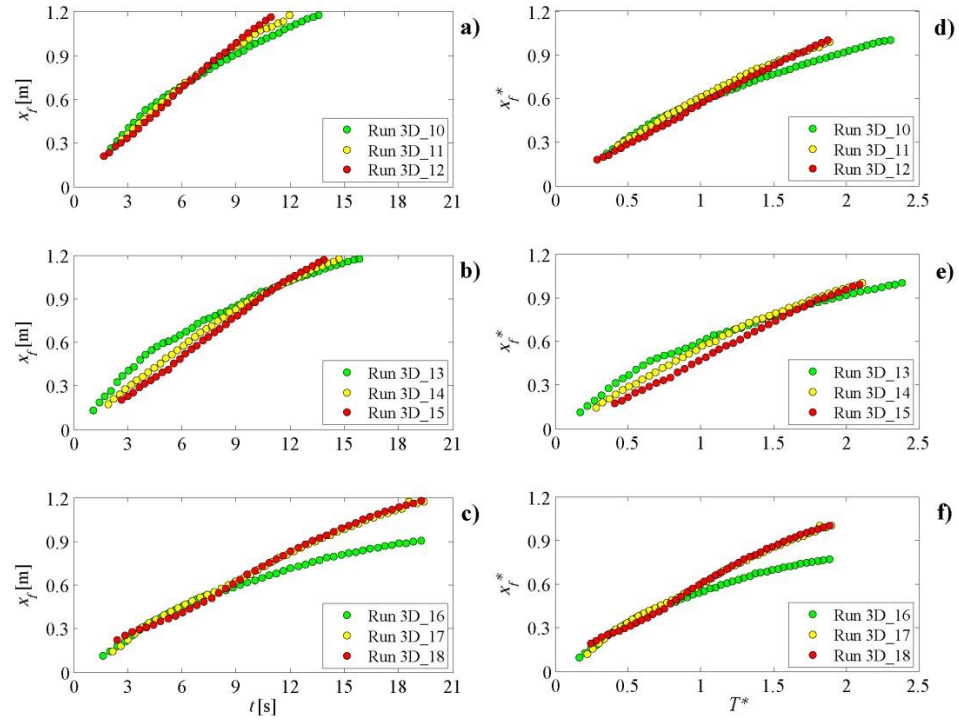
Figure 3.4a-f: Dimensional and dimensionless plot of front positions versus time for the runs with $\rho_{01} \cong 1030$ Kg/m^3; (a-d) Runs 3D_10-3D_11-3D_12: h_0=0.15 m, d=0.135, 0.35, 0.67 m; (b-e) Runs 3D_13-3D_14-3D_15: h_0=0.10 m, d=0.135, 0.35, 0.67 m; (c-f) Runs 3D_16-3D_17-3D_18: h_0=0.05 m, d=0.135, 0.35, 0.67 m.
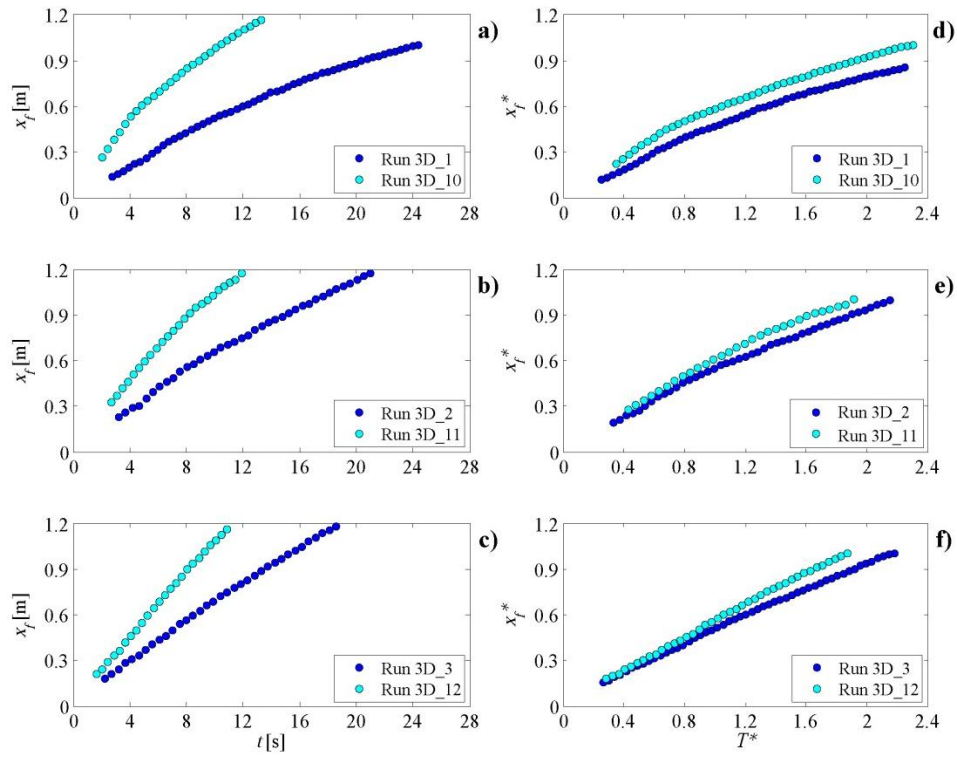
Figure 3.5a-f: Dimensional and dimensionless plot of front positions versus time for the runs with h_0=0.15 m; (a-d) Runs 3D_1-3D_10: d=0.135 m, $\rho_{01} \cong$1010, 1030 Kg/m³; (b-e) Runs 3D_2-3D_11: d=0.35 m, $\rho_{01} \cong$1010, 1030 Kg/m³; (c-f) Runs 3D_3-3D_12: d=0.67 m, $\rho_{01} \cong$1010, 1030 Kg/m³.
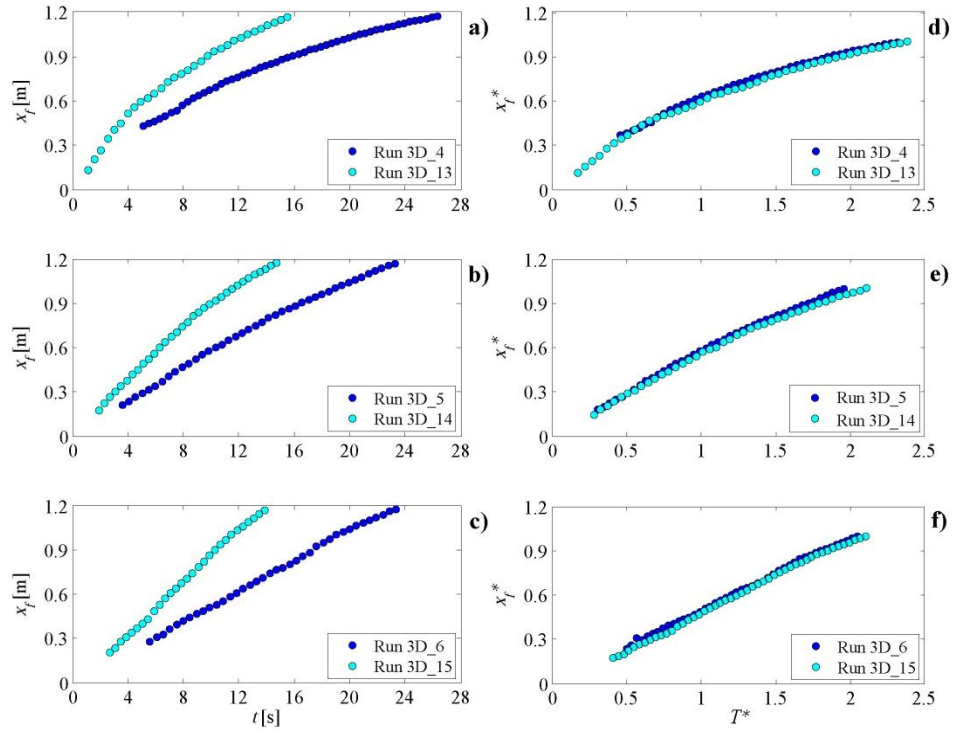
Figure 3.6a-f: Dimensional and dimensionless plot of front positions versus time for the runs h_0=0.10 m; (a-d) Runs 3D_4-3D_13: d=0.135 m, $\rho_{01}\cong$1010, 1030 Kg/m^3; (b-e) Runs 3D_5-3D_14: d=0.35 m, $\rho_{01}\cong$1010, 1030 Kg/m^3; (c-f) Runs 3D_6-3D_15: d=0.67 m, $\rho_{01}\cong$1010, 1030 Kg/m^3.
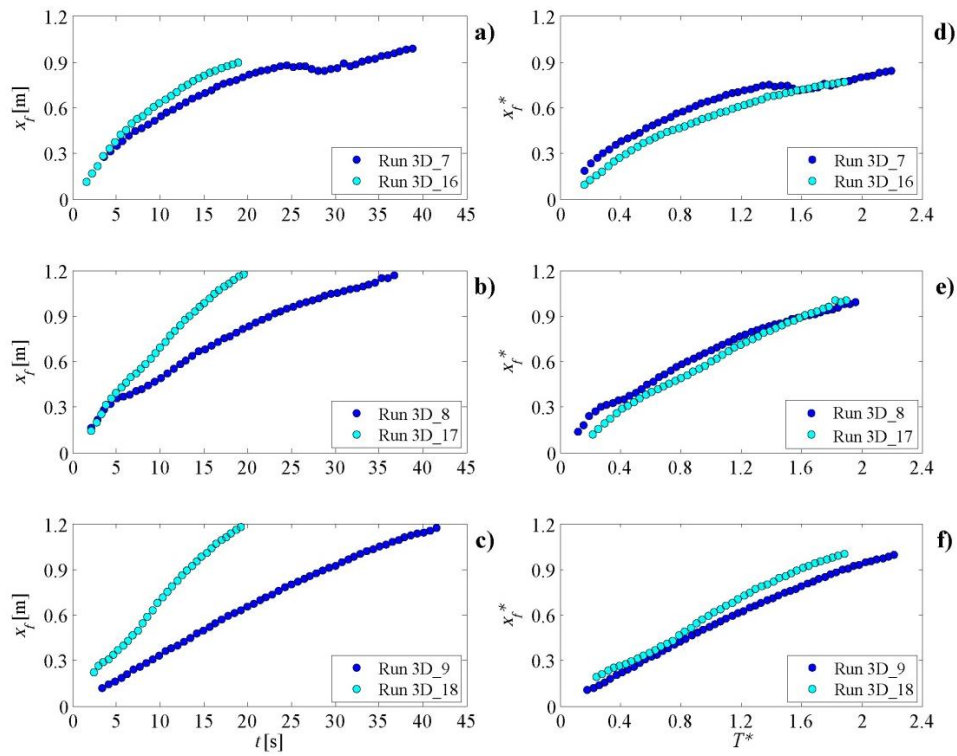
Figure 3.7a-f: Dimensional and dimensionless plot of front positions versus time for the runs with h_0=0.05 m; (a-d) Runs 3D_7-3D_16: d=0.135 m, $\rho_{01} \cong$ 1010, 1030 Kg/m³; (b-e) Runs 3D_8-3D_17: d=0.35 m, $\rho_{01} \cong$ 1010, 1030 Kg/m³; (c-f) Runs 3D_9-3D_18: d=0.67 m, $\rho_{01} \cong$ 1010, 1030 Kg/m³.
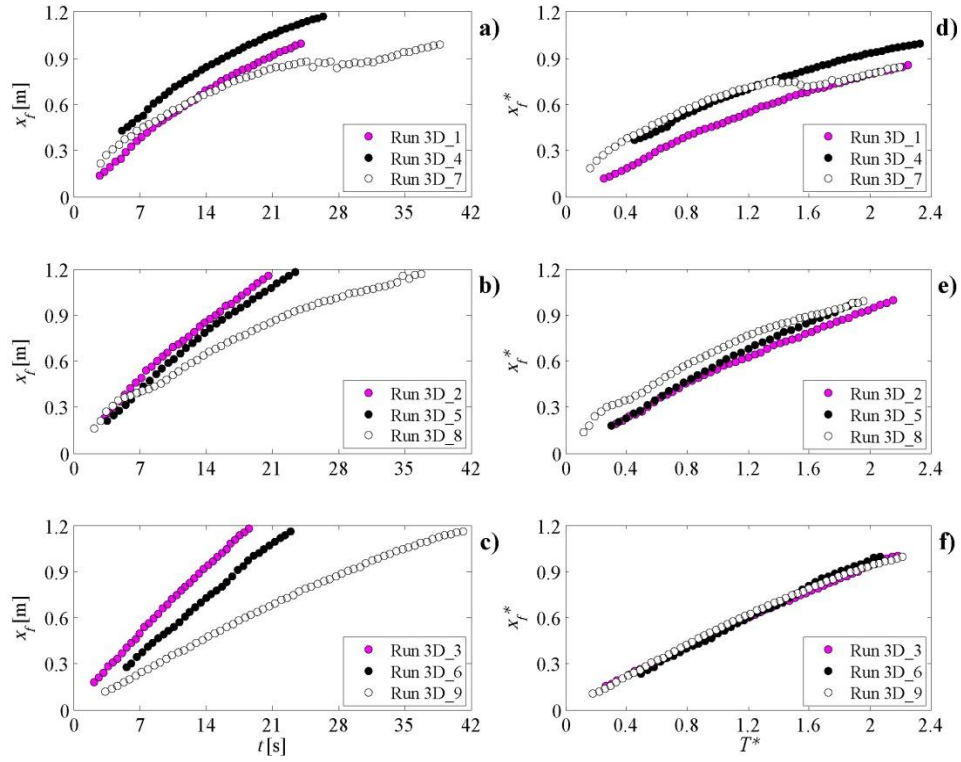
Figure 3.8a-f: Dimensional and dimensionless plot of front positions versus time for the runs with $\rho_{01} \cong 1010$ Kg/m^3; (a-d) Runs 3D_1-3D_4-3D_7: d=0.135 m, h_0=0.15, 0.10, 0.05 m; (b-e) Runs 3D_2-3D_5-3D_8: d=0.35 m, h_0=0.15,0.10, 0.05 m; (c-f) Runs 3D_3-3D_6-3D_9: d=0.67 m, h_0=0.15,0.10, 0.05 m.
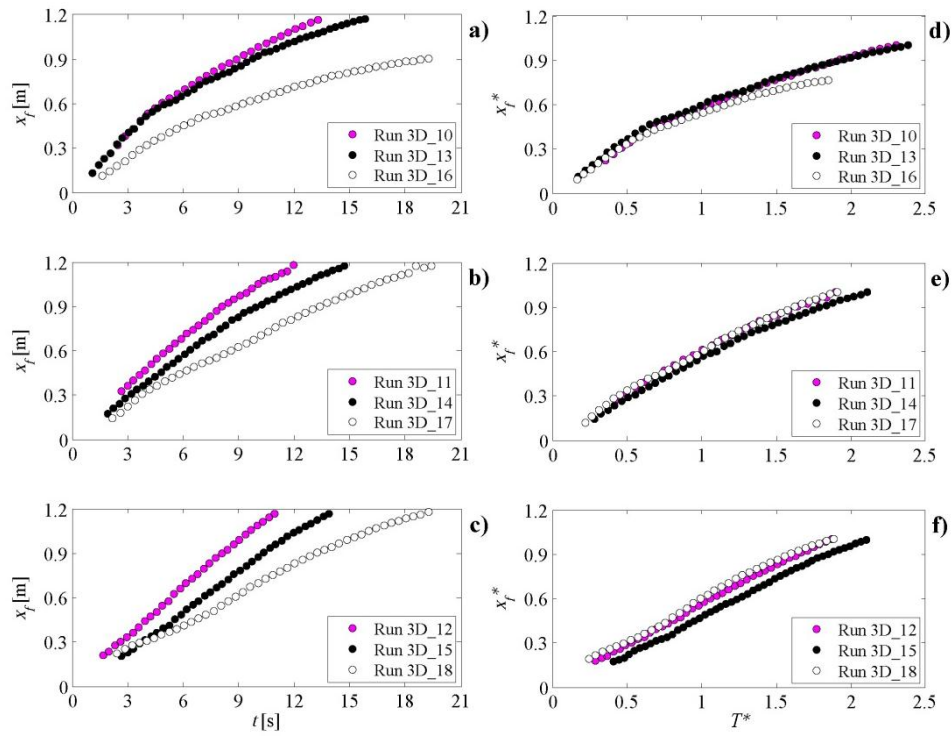
Figure 3.9a-f: Dimensional and dimensionless plot of front positions versus time for the runs with $\rho_{01} \cong 1030$ Kg/m^3; (a-d) Runs 3D_10-3D_13-3D_16: d=0.135 m, h_0=0.15,0.10, 0.05 m; (b-e) Runs 3D_11-3D_14-3D_17: d=0.35 m, h_0=0.15,0.10, 0.05 m; (c-f) Runs 3D_12-3D_15-3D_18: d=0.67 m, h_0=0.15,0.10, 0.05 m.

3.2. 2D numerical simulations

3.2.1. Mathematical model

Numerical simulations were performed using a single layer, two dimensional, shallow-water model. Figure 3.10 shows the frame of reference used in the mathematical model.

The lower layer (i.e. gravity current) with density ρ_1 and height h_1, flows below the upper layer of quiescent fluid with density ρ_2 ($\rho_1 > \rho_2$) and height h_2. The ratio h_1/h_2 is such that: $h_1/h_2 << 1$. The total height of the two layers is defined as H.

The density ρ_1 can be expressed as:

$$\rho_1 = \rho_2 + (\rho_s - \rho_2)c \qquad (45)$$

in which ρ_s and c are the density and the concentration of the fine uniform sediments, in case carried by the gravity current. The dimensionless number c is the ratio between the volume of sediments and the volume of water.

On the basis of the layer-averaged approach of Parker et al. (1986) and Bradford et al. (1997) the governing equations have the following form:

$$
\begin{cases}
\dfrac{\partial h_1}{\partial t} + \dfrac{\partial U h_1}{\partial x} + \dfrac{\partial V h_1}{\partial y} = \alpha U_m \\[2ex]
\dfrac{\partial U h_1}{\partial t} + \dfrac{\partial U^2 h_1}{\partial x} + \dfrac{\partial U V h_1}{\partial y} = \alpha U U_m - \dfrac{(\rho_s - \rho_2)g}{\rho_2}\dfrac{\partial}{\partial x}\left(C\dfrac{h_1^2}{2}\right) + \dfrac{1}{\rho_2}T_{xz}\big|_{z=0} \\[2ex]
\dfrac{\partial V h_1}{\partial t} + \dfrac{\partial U V h_1}{\partial x} + \dfrac{\partial V^2 h_1}{\partial y} = \alpha V U_m - \dfrac{(\rho_s - \rho_2)g}{\rho_2}\dfrac{\partial}{\partial y}\left(C\dfrac{h_1^2}{2}\right) + \dfrac{1}{\rho_2}T_{yz}\big|_{z=0} \\[2ex]
\dfrac{\partial C h_1}{\partial t} + \dfrac{\partial C U h_1}{\partial x} + \dfrac{\partial C V h_1}{\partial y} = \alpha C U_m + u_s(e_s - c_b)
\end{cases}
\qquad (46)
$$

being U, V and C the depth averaged velocity components along x and y axis and the depth averaged concentration, respectively. α is the entrainment coefficient and is given by the formula (Kostic & Parker, 2007):

$$\alpha = \frac{0.00153}{0.0204 + Ri} \qquad (47)$$

where the Richardson number Ri is defined as:
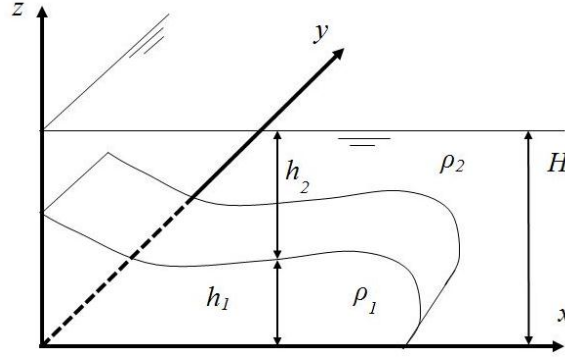
Figure 3.10: Sketch of the frame of reference used for the 2D mathematical model.

$$Ri = \frac{gCh_1}{U^2 + V^2}\left(\frac{\rho_s - \rho_2}{\rho_2}\right) \tag{48}$$

The velocity modulus U_m in the system (46) is given by:

$$U_m = \sqrt{U^2 + V^2} \tag{49}$$

Terms e_s and c_b in the system (46) are the resuspension coefficient and the value of the local concentration near the bed, respectively. e_s is assumed to be negligible with respect to c_b (Hallworth et al., 1998; Maxworthy, 1999; Gladstone & Woods, 2000; Kostic & Parker, 2003*a*, *b*; Kostic and Parker, 2007) which is proportional to the concentration C by means of the dimensionless parameter $r_0 \geq 1$. In agreement with Kostic and Parker (2007) r_0 is assumed to be a constant. The fall velocity of the suspended sediment u_s can be considered independent of the concentration of the sediment if $C \leq 10^{-2}$ (Bonnecaze et al., 1993) and can be given by the formula:

$$u_s = \frac{1}{\sqrt{C_R}}\sqrt{\frac{4}{3}\left(\frac{\rho_s - \rho_1}{\rho_1}\right)gd_s} \tag{50}$$

in which C_R is the drag coefficient of the sphere and d_s is the diameter of the sediment particles. In this case, compositional gravity currents rather than particle-driven gravity currents (i.e. turbidity currents) are performed; hence density gradient is exclusively due to a difference of salinity between the two fluids. Therefore, as no particles are present, the sedimentation term vanishes.

Finally, the last two terms on the right hand side of the momentum equations account for the bottom stress effects and can be expressed by:

$$
\begin{cases}
\dfrac{1}{\rho_2} T_{xz}\big|_{z=0} = \dfrac{\lambda}{8} U \sqrt{U^2 + V^2} \\[3mm]
\dfrac{1}{\rho_2} T_{yz}\big|_{z=0} = \dfrac{\lambda}{8} V \sqrt{U^2 + V^2}
\end{cases}
\tag{51}
$$

where the friction factor λ for turbulent rough flows is defined by the formula (Çengel and Cimbala, 2006):

$$
\lambda = \frac{0.25}{\left[Log\left(\dfrac{\varepsilon}{3.71 Hf} \right) \right]^2}
\tag{52}
$$

being f a shape factor.

3.2.2. Numerical method

According to the classification criterion of Bradford et al. (1997), the partial differential system (46) is hyperbolic because its eigenvalues are all real and admits a basis of real right eigenvectors.

Therefore the differential system can be put in a conservative form and it can be numerically solved by a finite-volume-based method, adopting the Godunov formulation with Roe's approximate Riemann solver. Hence systems (46) can be written as:

$$
\frac{\partial U}{\partial t} + \frac{\partial F(U)}{\partial x} + \frac{\partial G(U)}{\partial y} = S(U)
\tag{53}
$$

using the following definition for U, the vector of the conserved variables:

$$
U \equiv \{ h_1, Uh_1, Vh_1, Ch_1 \}
\tag{54}
$$

The vectors $F(U)$, $G(U)$ and $S(U)$ are expressed in terms of U in the following way:

$$\boldsymbol{F}(\boldsymbol{U}) \equiv \left\{ Uh_1, U^2h_1 + \frac{\rho_s - \rho_2}{\rho_2} gC\frac{h_1^2}{2}, UVh_1, CUh_1 \right\} \tag{55}$$

$$\boldsymbol{G}(\boldsymbol{U}) \equiv \left\{ Vh_1, UVh_1, V^2h_1 + \frac{\rho_s - \rho_2}{\rho_2} gC\frac{h_1^2}{2}, CVh_1 \right\} \tag{56}$$

$$\boldsymbol{S} \equiv \left\{ \alpha U_e, \alpha UU_e - \frac{\lambda}{8} U\sqrt{U^2 + V^2}, \right.$$
$$\left. \alpha VU_e - \frac{\lambda}{8} V\sqrt{U^2 + V^2}, \alpha CU_e + u_s(e_s - c_b) \right\} \tag{57}$$

Equation (53) can be put in a compact matrix form:

$$\frac{\partial \boldsymbol{U}}{\partial t} + \boldsymbol{A}\frac{\partial \boldsymbol{U}}{\partial x} + \boldsymbol{B}\frac{\partial \boldsymbol{U}}{\partial y} = \boldsymbol{S}(\boldsymbol{U}) \tag{58}$$

where $\boldsymbol{A} = d\boldsymbol{F}/d\boldsymbol{U}$ and $\boldsymbol{B} = d\boldsymbol{G}/d\boldsymbol{U}$.

The one layer partial differential system, being in conservative form, can be numerically solved with a finite volume numerical method. La Rocca et al. (2008) developed the numerical model used in this application, whose details are omitted, for the sake of simplicity. The reader can find them in the book of Toro (1999) and in the papers of La Rocca et al. (2008) and La Rocca et al. (2009).

The computational domain is divided into N elements, at the center of which the variables h, Uh, Vh and Ch are defined. The boundary condition of no flux normal to the sidewalls of the tank is imposed by the introduction of virtual elements outside the control volume having an opposite value to the corresponding element inside the domain, at the other side of the wall. Boundary conditions on h, Ch are imposed by setting the virtual values of h, Ch to the same values from the corresponding real element. Following Chippada et al. (1998), the CFL stability condition used is the same of La Rocca et al. (2008) and assumes the expression:

$$\Delta t \leq \min\left(\frac{d}{\lambda_{max}} \right) \tag{59}$$

where d is the minimum size of the element, and λ_{max} is the eigenvalue with the largest modulus among the eigenvalues of the matrices $\boldsymbol{A}$, $\boldsymbol{B}$.

3.2.3. Comparison between experimental and numerical results

Figure 3.11a-c and Figure 3.12a-c show the comparison between numerical and experimental dimensionless front's position versus dimensionless time for all the runs performed with $\rho_{01} \cong 1010$ and 1030 Kg/m^3, respectively. Dimensionless front position and dimensionless time are defined by Equation (43) and Equation (44), respectively. By a qualitative analysis of the plots a good agreement between experimental and numerical results for the runs performed with h_0=0.15, 0.10 m (Figure 3.11a-3.12a, Figure 3.11b-3.12b) can be observed, while a discrepancies between experimental data and numerical prediction can be noticed for the runs performed with the lower value of h_0=0.05 m (Figure 3.11c, Figure 3.12c). In order to quantify such a discrepancy, the mean percentage difference of front position between experimental results and numerical prediction E_{xf} was evaluated as for the 1D shallow-water model, in the following way:

$$E_{xf} = Mean\left(\left| 1 - \frac{x_{nf}^*}{x_{ef}^*} \right| \times 100 \right) \tag{60}$$

being x_{nf}^* and x_{ef}^* the numerical and experimental dimensionless front position, respectively. Table 6 shows the value of E_{xf} for each run. The mean error E_{xf} reaches a minimum value of 1.6% for the run 3D_11 and a maximum value of 49.5 % for the run 3D_16. In particular, reasonable values of E_{xf} are obtained for all the runs, except the runs 3D_7-3D_16-3D_17, whose mean percentage error is 43.6 %, 49.5%, 31.7%, respectively. Runs 3D_7-3D_16-3D_17 are the experiments performed with h_0=0.05 m and, as already observed from Figure 3.11a-c and Figure 3.12a-c, show the maximum discrepancy between experimental and numerical front position.

This fact can be due to the application of the one layer approximation used for the numerical model, which seems to be suitable for high initial depth of the fluid (i.e. h_0=0.15, 0.10 m), when free-surface oscillations do not influence the development of the gravity current. On the contrary for the case of lower depth of the dense fluid (i.e. h_0=0.05 m) maybe the current's dynamics is influenced by the oscillation of the free surface, given the lower thickness of the dense layer, and such an oscillation should not be neglected anymore.

Figure 3.13a-i and Figure 3.14a-i show the comparison of current's profiles, obtained by laboratory measurements and numerical simulations for all the runs performed with $\rho_{01} \cong 1010$ and 1030 Kg/m^3, respectively. The contour of experimental gravity currents is obtained from a top view, applying threshold's method to the images acquired by the camera, as fully explained in section 3.1.1.

The corresponding numerical top view of the current's shape is obtained from the contour plot of the gravity current numerical surface. Each plot in Figure 3.13a-i and Figure 3.14a-i show current's profile at four different time steps. For some runs experimental profiles (Figure 3.13f and Figure 3.14d) show a shape dissymmetry, probably due to the manual removal of the sliding gate, which does not allow a homogeneous flow through the gate.

The ability of the model in reproducing the gravity current's shape is fairly good for the same runs whose mean error E_{xf} reach reasonable values, while it is not acceptable for the runs performed with h_0=0.05 m, whose discrepancy between experimental and numerical front's position was observed.

La Rocca et al. (2009) was focused on 3D gravity current's dynamics varying bed's roughness and initial density of the dense fluid and keeping constant the initial height of the two fluids h_0=0.15 m. They observed a good agreement between experimental results and numerical prediction obtained with the same model used in this work. This fact confirm the hypothesis that the discrepancy observed between experimental and numerical results in this work can be attributed to the limits of the numerical model in reproducing the dynamics of gravity currents with a small depth.

Run	ρ_{01} [Kg/m^3]	h_0 [m]	d [m]	E_{xf} [%]
3D_1	1008	0.15	0.135	7.2
3D_2	1010	0.15	0.350	3.5
3D_3	1013	0.15	0.670	12.2
3D_4	1011	0.10	0.135	9.4
3D_5	1010	0.10	0.350	5.5
3D_6	1011	0.10	0.670	10.3
3D_7	1009	0.05	0.135	43.6
3D_8	1008	0.05	0.350	18.8
3D_9	1008	0.05	0.670	9.1
3D_10	1027	0.15	0.135	4.6
3D_11	1024	0.15	0.350	1.6
3D_12	1027	0.15	0.670	7.6
3D_13	1032	0.10	0.135	7.2
3D_14	1029	0.10	0.350	4.1
3D_15	1032	0.10	0.670	16.1
3D_16	1027	0.05	0.135	49.5
3D_17	1027	0.05	0.350	31.7
3D_18	1027	0.05	0.670	12.0

Table 6: Experimental parameters and mean error E_{xf} computed for each run on the basis of Equation (60) for all the 3D released currents.
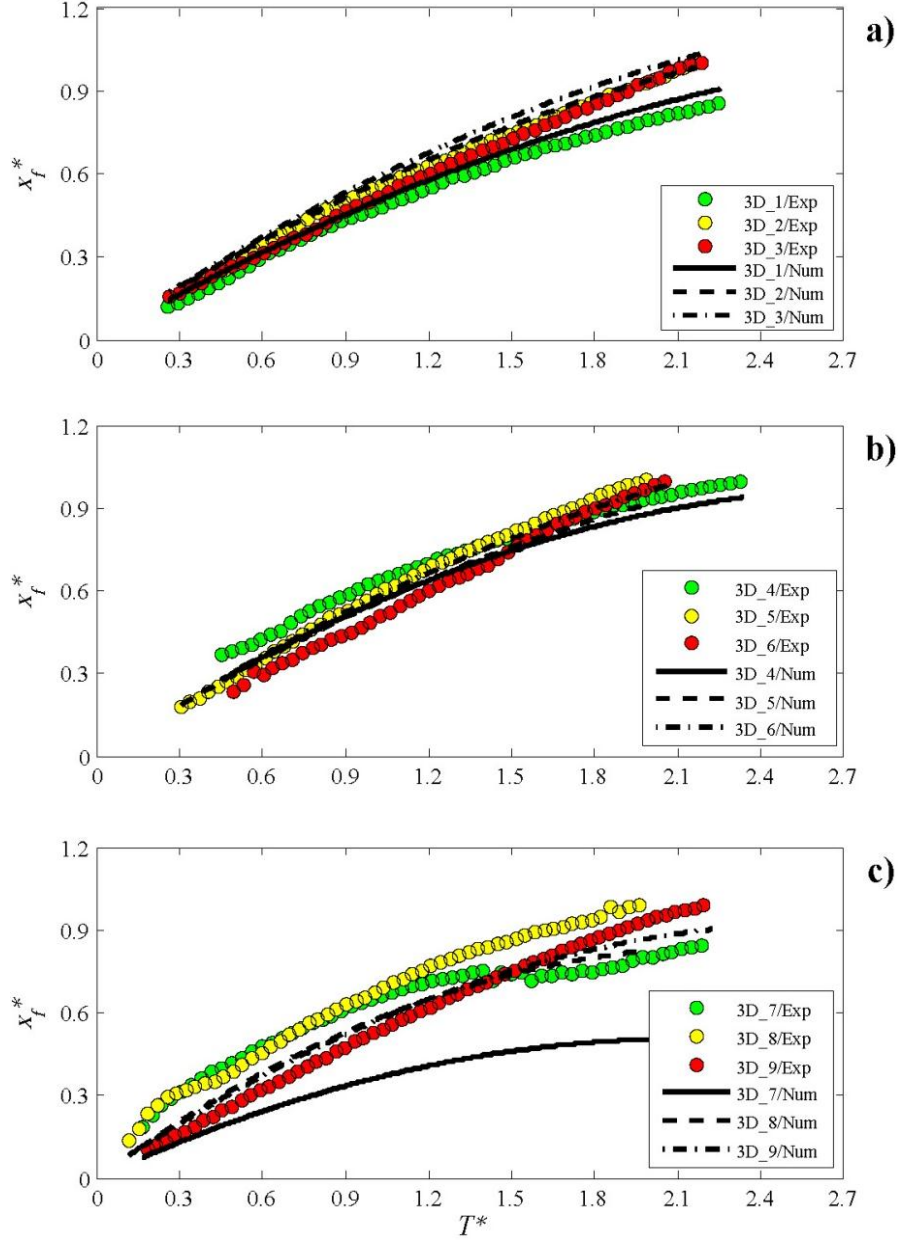
Figure 3.11a-c: Dimensionless plot of experimental and numerical front positions versus time for the runs performed with $\rho_{01} \cong 1010$ Kg/m^3. (a) Runs 3D_1-3D_2-3D_3 performed with h_0=0.15 m and d=0.135, 0.35, 0.67 m, respectively; (b) Runs 3D_4-3D_5-3D_6 performed with h_0=0.10 m and d=0.135, 0.35, 0. 67 m, respectively; (c) Runs 3D_7-3D_8-3D_9 performed with h_0=0.05 m and d=0.135, 0.35, 0.67 m, respectively. The front position is detected along the centerline of the tank.
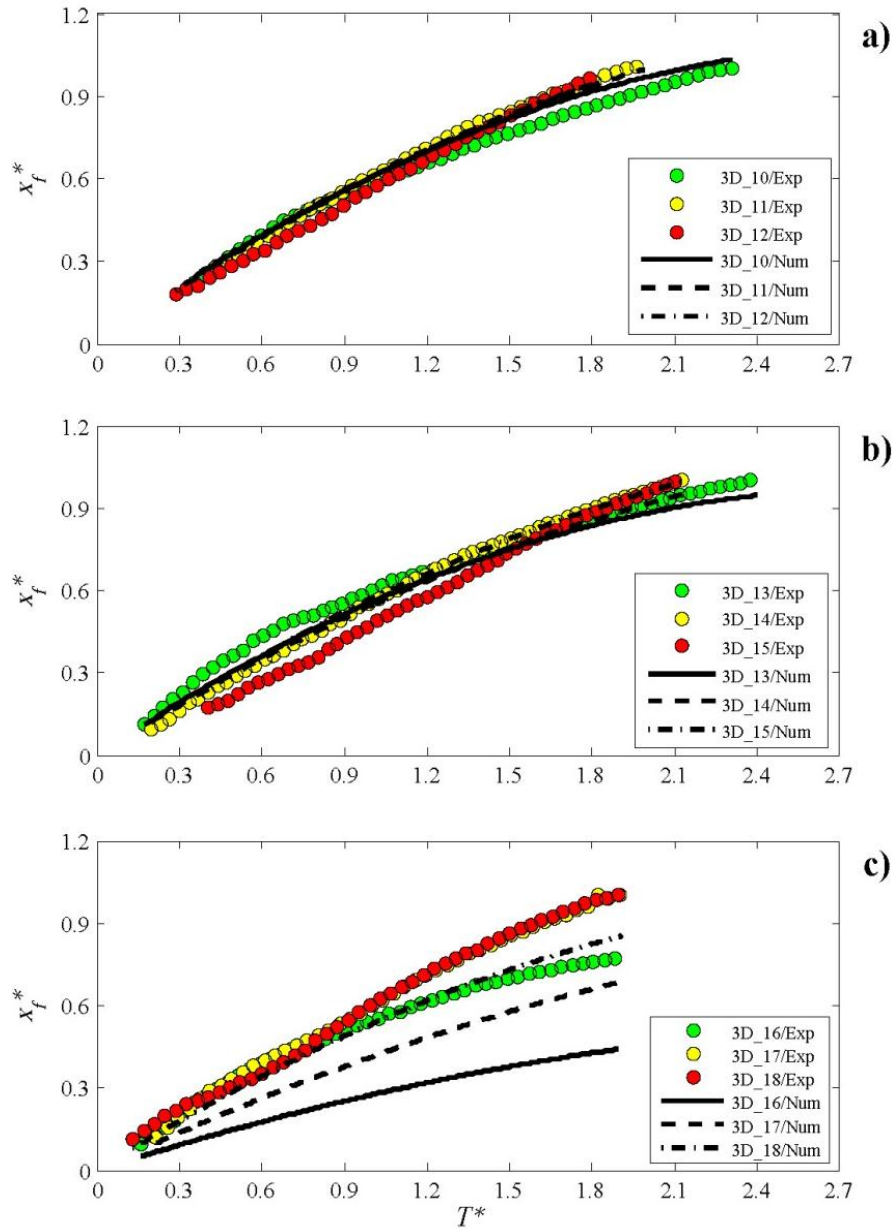
Figure 3.12a-c: Dimensionless plot of experimental and numerical front positions versus time for the runs performed with $\rho_{01} \cong 1030$ Kg/m³. (a) Runs 3D_10-3D_11-3D_12 performed with h_0=0.15 m and d=0.135, 0.35, 0.67 m, respectively; (b) Runs 3D_13-3D_14-3D_15 performed with h_0=0.10 m and d=0.135, 0.35, 0.67 m, respectively; (c) Runs 3D_16-3D_17-3D_18 performed with h_0=0.05 m and d=0.135, 0.35, 0.67 m, respectively. The front position is detected along the centerline of the tank.
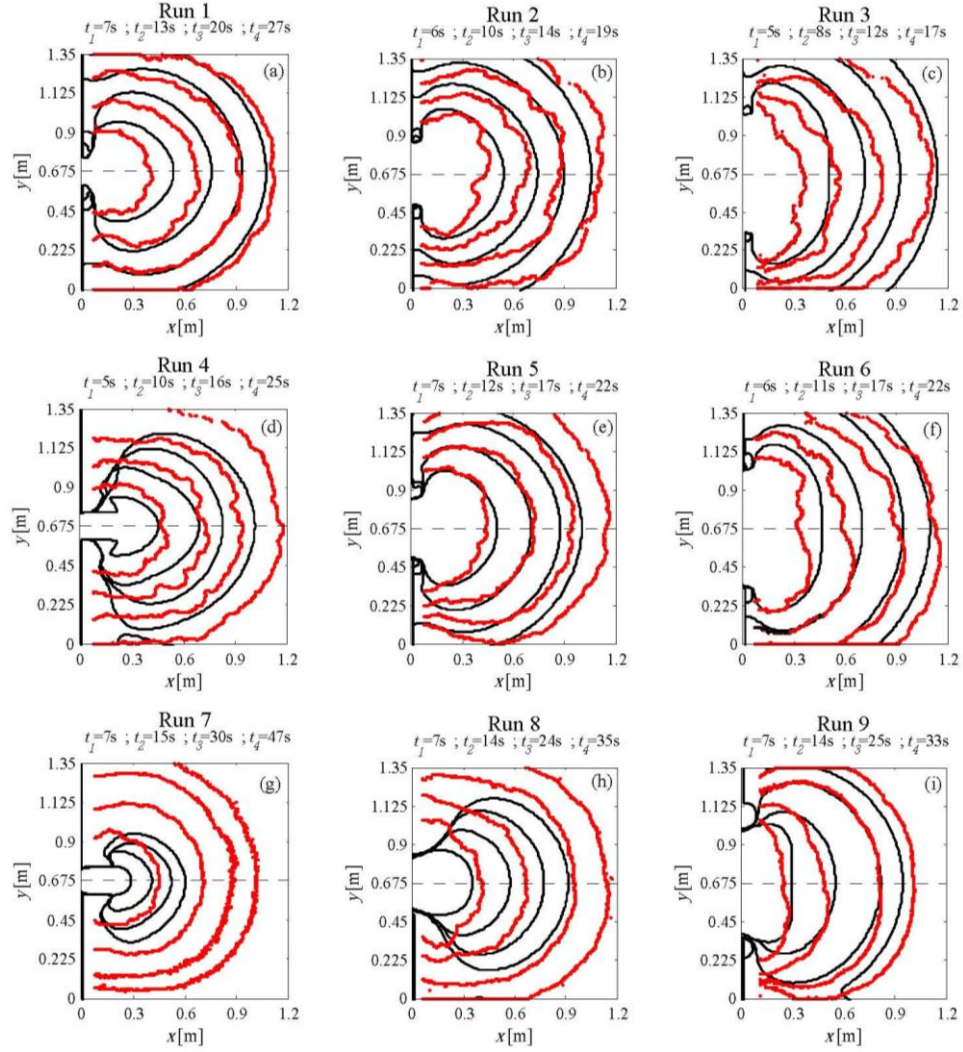
Figure 3.13a-i: Comparison between experimental and numerical wave front for the runs performed with $\rho_{01} \cong 1010$ Kg/m^3. (a) Run 3D_1: h_0=0.15 m and d=0.135 m; (b) Run 3D_2: h_0=0.15 m and d=0.35 m; (c) Run 3D_3: h_0=0.15 m and d=0.67 m; (d) Run 3D_4: h_0=0.10 m and d=0.135 m; (e) Run 3D_5: h_0=0.10 m and d=0.35 m; (f) Run 3D_6: h_0=0.10 m and d=0.67 m; (g) Run 3D_7: h_0=0.05 m and d=0.135 m; (h) Run 3D_8: h_0=0.05 m and d=0.35 m; (i) Run 3D_9: h_0=0.05 m and d=0.67 m.
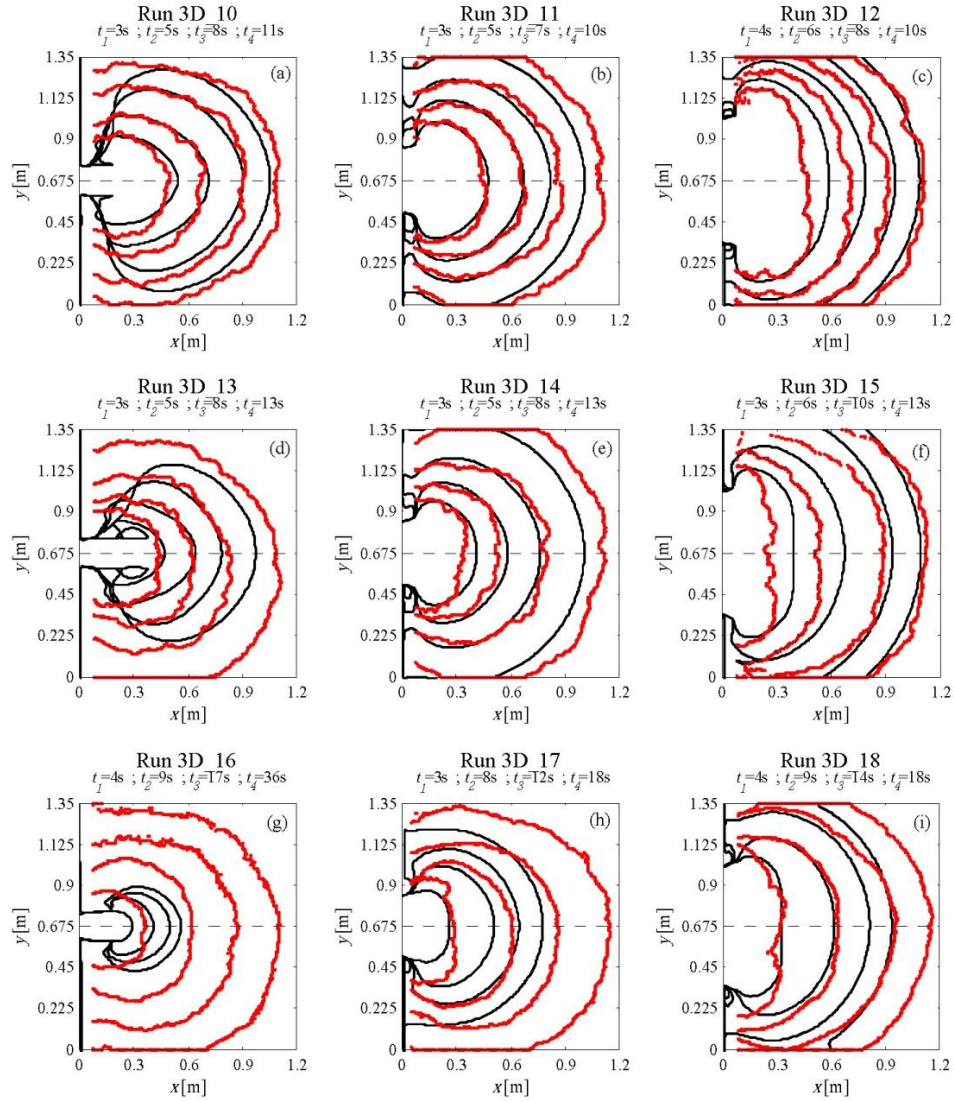
Figure 3.14a-i: Comparison between experimental and numerical wave front for the runs performed with $\rho_{01} \cong 1030$ Kg/m^3. (a) Run 3D_10: h_0=0.15 m and d=0.135 m; (b) Run 3D_11: h_0=0.15 m and d=0.35 m; (c) Run 3D_12: h_0=0.15 m and d=0.67 m; (d) Run 3D_13: h_0=0.10 m and d=0.135 m; (e) Run 3D_14: h_0=0.10 m and d=0.35 m; (f) Run 3D_15: h_0=0.10 m and d=0.67 m; (g) Run 3D_16: h_0=0.05 m and d=0.135 m; (h) Run 3D_17: h_0=0.05 m and d=0.35 m; (i) Run 3D_18: h_0=0.05 m and d= .67 m.

4. Conclusions and future aims

This work investigates gravity currents by both laboratory experiments and numerical simulations. 2D and 3D experimental gravity currents were realized by lock exchange release technique. In this configuration a tank is divided by a vertical sliding gate into two reservoirs, one filled with salty water and the other with fresh water, in order to create a density gradient at the two sides of the gate. When the gate is suddenly removed, the heavier fluid collapses flowing under the lighter one and the gravity current develops. By applying an image analysis technique, based on threshold method, the space-time evolution of the current's profile was measured.

Regarding 2D gravity currents, several experiments were performed keeping constant the gate position, the height of the two fluids and the density of the surrounding fluid and testing different values of the initial density of the gravity current, bed's roughness and slope's angle. Experimental results show that the speed of the current increases as the initial density of released current increases. Moreover, dimensionless plot of front position versus time for the runs performed with different values of the initial density of the gravity current and keeping constant the other experimental parameters shows that the time histories of front position lye on the same curve. Such a result is in agreement with most of the studies about gravity currents. For the runs performed on flat and smooth beds a comparison with theoretical front evolution given by previous studies was performed. In particular, three distinct phases in the dynamics of gravity currents realized on flat and smooth beds by an instantaneous release were distinguished by Huppert & Simpson (1980) and Rottman & Simpson (1983). Experimental data are in agreement with previous formulae only for the first and the second phase, while the third phase seems not to occur in the current's evolution of the performed runs. Such a discrepancy could be due to the fact that viscous phases of the realized currents are not long enough to be observable.

Experimental results of gravity currents moving on flat and rough beds show a general trend of decrease of the speed of the currents as the bed roughness increases. In particular as the initial density of the heavier fluid increases, a decrease of the decelerating effect due to the bed's roughness can be observed. As a superimposition of some runs in the time histories of front positions can be observed, additional experiments a fixed rough bed for each set of runs are required in order to improve the certainty of the values of the used roughness.

2D experimental gravity currents moving on upsloping beds were performed. While gravity currents realized with critical and subcritical slope's angle reach the end of the tank, runs performed with supercritical angles stops before the end

wall of the tank. As expected, increasing the slope's angle, a decrease of the current's speed can be observed.

A 1D, two-layer, shallow-water model developed by Adduce et al. (2012) was used to perform numerical simulations of the gravity currents moving on smooth flat and upsloping beds. The oscillation of the free surface and the mixing between the two layers are taken into account in the mathematical model. The entrainment at the interface, due to a mass transport from the lighter fluid to the heavier one, causes a decrease of the density of the gravity current. The entrainment between the two fluids was modeled by a modified Ellison & Turner's formula (1959). Several tests were run to calibrate the dimensionless coefficient k in order to have a good simulation of both the front position and the profile of the gravity current. The comparison between experimental measurements and numerical results for miscible fluids shows a good agreement both for the gravity current's profiles and for the front's positions. Therefore the presented model is able to reproduce gravity current's dynamics on both horizontal and upsloping beds.

For the 2D configuration PIV technique was applied in order to measure the velocity field of gravity currents produced by lock exchange release. One of the main objectives of this stage of work was to verify the reliability of the back flow predicted for gravity currents moving on upsloping beds by the one-dimensional numerical model near the lock of the tank. Two experiments were realized to perform instantaneous velocity measurements: a first preliminary run was carried out in order to test the PIV system for gravity current moving on flat and smooth bed and a second run was realized on smooth upsloping bed in order to compare experimental results with numerical predictions. In order to avoid the problem of local changes of index of refraction between the two fluids near the lock where density gradient is high and particle cannot be distinguished RIM (Refractive Index Matching) method was applied.

From the comparison between numerical profiles and velocity values measured by PIV along the y-direction, the presence of a backflow can be noticed observing both numerical and measured values. However, as the backflow is predicted by the numerical model to be wider than the one observed by experimental analysis additional laboratory experiments and PIV measurements should be performed in order to verify the real extent of this phenomenon.

Velocity measurements show the main features of a typical gravity current: the main direction of the lock fluid is along the x-axis while the surrounding fluid moves upward and backward in the opposite direction with a lower velocity. In agreement with previous studies the vorticity fields show two main areas of positive and negative values at the interface between the two layers and along the rigid bottom boundary, respectively.

3D gravity currents were realized keeping constant the density of the lighter fluid and varying the initial density of the heavier one, the height of the two fluids and the length of the gate. Experimental results shows that during the

same time the runs performed with the smaller value of the gate's length cover a smaller distance than those realized with higher values of this parameter. Moreover the speed of the current is observed to be directly proportional to both the initial density of the heavier fluid and the initial height of the fluids. Numerical simulations of 3D gravity current were performed using a 2D single-layer, shallow-water model. The entrainment between the two fluids and the phenomena of settling and resuspension of particles are taken into account in the mathematical model. Indeed the model could reproduce both gravity and turbidity currents. Although in this work only compositional gravity currents obtained with a solution of tap water and salt were realized.

The comparison between experimental results and numerical prediction of the front's position shows a fairly good agreement for all the runs except the ones performed with the lower value of initial height of the fluids. This fact can be due to the application of the single layer approximation used for the numerical model, which seems to be suitable for high initial depth of the fluid, when free-surface oscillations do not influence the development of the gravity current, while for lower depth of the dense fluid the current's dynamics is influenced by the oscillation of the free surface, given the lower thickness of the dense layer, and such an oscillation should not be neglected anymore. Anyway the obtained results encourage the continuation of the work in order to investigate also turbidity current's dynamics taking into account deposition and resuspension of particles.

References

Adduce, C., Sciortino, G. and Proietti, S. (2012), *Gravity currents produced by lock-exchange: experiments and simulations with a two layer shallow-water model with entrainment*, J. Hydraul. Eng., 138(2), 10.1061/(ASCE)HY.1943-7900.0000484.

Adrian, R.J. (1991), *Particle-imaging techniques for experimental fluid mechanics,* Annu. Rev. Fluid Mech., 22: 261-304.

Alahyari, A. and Longmire, E.K. (1994), *Particle image velocimetry in a variable density flow: application to a dynamically evolving microburst*, Exp. Fluids, 17:434-440.

Alahyari, A. and Longmire, E.K. (1996), *Development and structure of a gravity current head*, Exp. Fluids, 20:410-416.

Benjamin, T.B. (1968), *Gravity currents and related phenomena*, J. Fluid Mech., 31: 209-248.

Bonnecaze, R.T., Huppert, H.U. and Lister, J. (1993), *Particle driven gravity currents*, J. Fluid Mech., 250:339-369.

Bradford, F., Katopodes, N.D. and Parker, G. (1997), *Characteristic analysis of turbid underflows*, J. Hydraul. Eng., 123:420-431.

Cantero, M., Lee, J., Balachandar, S. and García, M. (2007), *On the front velocity of gravity currents*, J. Fluid Mech., 586:1-39.

Cantero, M., Balachandar, S., García, M. and Ferry, J. (2006), *Direct numerical simulations of planar and cylindrical density currents*, J. Appl. Mech., 73(6):923-930.

Cenedese, C. and Adduce, C. (2008), *Mixing in a density driven current flowing down a slope in a rotating fluid*, J. Fluid Mech., 604: 369-388.

Çengel, Y.A. and Cimbala, J.M. (2006), *Fluid Mechanics: fundamentals and applications*, Mac Graw Hill, New York.

Chippada, S., Dawson, C.N., Martinez, M.L. and Wheeler, M.F. (1998), *A Godunov-type finite volume method for the system of shallow water equations*, Comput. Methods Appl. Mech. Eng. 151:105-129.

Colebrook, C.F. (1939), *Turbolent flows in pipes, with particular reference to the transition region between the smooth and rough pipe laws*, J. Inst. Civ. Eng., 11:133-156.

Darcy, H. (1857), *Recherches expérimentales relatives au mouvement de l'eau dans les tuyaux*, Mallet-Bachelier, Paris.

Ellison, T.H. and Turner, J.S. (1959), *Turbolent entrainment in stratified flows*, J. Fluid Mech., 6:423-448.

Gladstone, C. and Woods, A. (2000), *On the application of box models to particle-driven gravity currents*, J. Fluid Mech., 416:187-195.

Hallworth, M.A., Hogg, A.J. and Huppert, H.E. (1998), *Effects of external flow on compositional and particle gravity currents*, J. Fluid Mech., 359:109-142.

Härtel, C., Meiburg, E. and Necker, F. (2000a), *Analysis and direct numerical simulation of the flow at a gravity current head – Part 1: Flow topology and front speed for slip and no-slip boundaries*, J. Fluid Mech., 418:189-212.

Härtel, C. Carlsson, F. and Thunblom, N. (2000b), *Analysis and direct numerical simulation of the flow at a gravity current head – Part 2: The lob-and-cleft instability*, J. Fluid Mech., 418:213-229.

Huppert, H.E. (1982), *The propagation of two-dimensional and axisymmetric viscous gravity currents over a rigid horizontal surface*, J. Fluid Mech., 121:43-58.

Huppert, H.E. (2006), *Gravity currents: a personal perspective*, J. Fluid Mech., 554:299-322.

Huppert, H.E. and Simpson, J.E. (1980), *The slumping of gravity currents*, J. Fluid Mech., 99:785-799.

Kármán, T. von (1940), *The engineer grapples with nonlinear problems*, Bull. Am. Math. Soc., 46:615-683.

Klemp, J.B., Rotunno R. and Skamarock W.C. (1994), *On the dynamics of a gravity current in a channel*, J. Fluid Mech., 269:169-198.

Kostic, S. and Parker, G. (2003a), *Progradational sand-mud deltas in lakes and reservoirs: Part 1. Theory and numerical modeling*, J. Hydraul. Res., 41(2):127-140.

Kostic, S. and Parker, G. (2003b), *Progradational sand-mud deltas in lakes and reservoirs: Part 2. Experiment and numerical simulation*, J. Hydraul. Res., 41(2):141-152.

Kostic, S. and Parker, G. (2007), *Conditions under which a supercritical turbidity current traverses an abrupt transition to vanishing bed slope without a hydraulic jump*, J. Fluid Mech., 586:119-145.

La Rocca, M., Adduce, C., Sciortino, G. and Bateman Pinzon A. (2008), *Experimental and numerical simulation of three-dimensional gravity currents on smooth and rough bottom*, Phys. Fluids, 20:106603.

La Rocca M., Adduce C., Mele P., Sciortino G. (2009), *Numerical simulation of 3D submarine turbidity currents*, ISOPE 2009 Conference Proceedings.

La Rocca, M., Adduce, C., Lombardi, V., Sciortino, G. and Hinkelmann, R. (2012), *Development of a Lattice Boltzmann Method for two-layered shallow-water flow*, Int. J. Numer. Meth. Fluids, doi: 10.1002/fld.2742 (Published online).

Marino, B.M., Thomas, L.P. and Linden, P.F. (2005), *The front condition of gravity currents,* J. Fluid Mech., 536:49-78.

Martin, J.E. and García, M.H. (2009), *Combined PIV/PLIF measurements of a steady density current front*, Exp. Fluids, 46:265-276.

Maxworthy, T. (1999), *The dynamics of sedimenting surface gravity currents*, J. Fluid Mech., 392:27-44.

Ooi, S.K. (2007), *2D large-eddy simulation of lock-exchange gravity current flows at high Grashof numbers*, J. Hydraul. Eng., 133(9):1037-1047.

Parker, G., Fukushima, Y. and Pantin, H.M. (1986), *Self-accelerating turbidity currents*, J. Fluid Mech., 171:145-181.

Prandtl, L. (1952), *Essential of fluid dynamics*, Blackie & Son, London.

Rottman, J.W. and Simpson, J.E. (1983), *Gravity currents produced by instantaneous release of a heavy fluid in a rectangular channel*, J. Fluid Mech., 135:95-110.

Simpson, J.E. (1982), *Gravity currents in the laboratory, atmosphere, and ocean*, Ann. Rev. Fluid Mech., 14:213-234.

Simpson, J.E. (1997), *Gravity currents in the environment and the laboratory*, Cambridge university press, Cambridge.

Shin, J.O., Dalziel, S.B. and Linden, P.F. (2004), *Gravity currents produced by lock exchange*, J. Fluid Mech., 521:1-34.

Sparks, R.S., Bonnecaze, R.T., Huppert, H.E., Lister, J.R., Hallworth, M.A., Mader, H. and Philips, J. (1993), *Sediment-laden gravity currents with reversing buoyancy*, Earth and Plan. Sc. Let., 114:243-257.

Supino, G. (1981), *Manuale dell'Ingegneria Civile*, Edizioni Scientifiche A. Cremonese, Roma, 242-246.

Thomas, L.P., Dalziel, S.B. and Marino, B.M. (2003), *The structure of the head of an inertial gravity current determined by particle-tracking velocimetry*, Exp. Fluids, 34:708-716.

Toro, EF (1999), *Riemann Solvers and Numerical Methods for Fluid Dynamics*, Springer, New York.

Turner, J.S. (1986), *Turbolent entrainment: the development of the entrainment assumption, and its application to geophysical flows*, J. Fluid Mech., 173:431-471.

Ungarish, M. (2009), *An introduction to gravity currents and intrusions*, CRC Press, Boca Raton.

Weisbach, J. (1845*), Lehrbuch der Ingenieur- und Maschinen-Mechanik*, Vieweg und Sohn, Braunschweig, Vol. I.

Zhu, J.B., Lee, C.B., Chen, G.Q. and Lee, J.H.W. (2006), *PIV observation of instantaneous velocity structure of lock release gravity currents in the slumping phase*, Comm. Nonlinear Sci. Numer. Simulat. 11:262-270.

Acknowledgments